

AN ABSTRACT OF THE THESIS OF

Michael Louis Lesiecki for the degree of Doctor of Philosophy

in Chemistry presented on July 11, 1975

Title: Spectroscopic Studies of Matrix Isolated High Temperature

Molecules

Abstract approved:

*Redacted for Privacy*

Dr. J. W. Nibler

A number of systems of matrix isolated high temperature molecules have been studied using spectroscopic techniques. Infrared and Raman spectra have been obtained for  $\text{PrF}_3$  and  $\text{LaF}_3$  and from a coincidence between the Raman active symmetric stretch ( $526 \text{ cm}^{-1}$ ,  $\text{PrF}_3$ ;  $514 \text{ cm}^{-1}$ ,  $\text{LaF}_3$ ) and a corresponding weak feature in the infrared we have been able to deduce a non-planar  $C_{3v}$  symmetry for both species. Our conclusions are in agreement with a gas phase electric deflection result for  $\text{LaF}_3$  but differ for  $\text{PrF}_3$  since the deflection experiment for this molecule implies a planar  $D_{3h}$  configuration.

Infrared and Raman spectra are presented for monomeric and dimeric thallos halide species ( $\text{TlF}$ ,  $\text{Tl}_2\text{F}_2$ ,  $\text{TlCl}$  and  $\text{Tl}_2\text{Cl}_2$ ) isolated in argon matrices. From these results it is concluded that both the  $\text{Tl}_2\text{F}_2$  and  $\text{Tl}_2\text{Cl}_2$  molecules have planar rhombic structures rather than linear configurations as previously proposed on the basis of mass spectroscopic, infrared and photoelectron studies. Entropy

calculations and other arguments are presented to resolve this discrepancy. Our structural conclusion for  $\text{Tl}_2\text{F}_2$  is in good accord with a very recent electron diffraction investigation of  $\text{Tl}_2\text{F}_2$  and the structural parameters and vibrational amplitudes obtained in that work are incorporated with our frequencies in a normal coordinate analysis. Force fields are obtained for both  $\text{Tl}_2\text{F}_2$  and  $\text{Tl}_2\text{Cl}_2$  and a very large amplitude ( $31^\circ$ ) is calculated for the out of plane bending coordinate of  $\text{Tl}_2\text{F}_2$ . Assuming that the bonding in this compound is largely ionic, an average instantaneous vibrational dipole moment of 3.7 Debye is deduced. This very large value in a 'non polar' molecule is in good agreement with a novel electron scattering experiment on  $\text{Tl}_2\text{F}_2$  molecular beams in which vibrational dipoles in the range 2 to 8 Debye were recently reported.

For the magnesium dihalides the complete vibrational spectrum has been obtained and the observation of the  $\nu_1$  symmetric stretch in the Raman (argon matrix:  $\text{MgF}_2$ , 550.0;  $\text{MgCl}_2$ , 326.5;  $\text{MgBr}_2$ , 197.7;  $\text{MgI}_2$ ,  $147.6 \text{ cm}^{-1}$ ) leads us to conclude that all the molecules in this series are linear. This is in agreement with the majority of the previous experimental and theoretical work and establishes that the assignment of a bent configuration in a previous infrared study of  $\text{MgF}_2$  was incorrect. A number of spectral complications were observed, such as a weak feature in the infrared (for  $\text{MgF}_2$  and  $\text{MgCl}_2$ ) that was apparently the analog of  $\nu_1$ . The infrared activity in this mode was discussed in terms of a probable weak complex

formation. Accurate potential constants have been determined and used as a basis for evaluating several theoretical models for the bonding in the alkaline earth dihalides and in  $\text{MgF}_2$  in particular. Models based on ionic descriptions were the most successful in reproducing the observed bending force constants. A calculation of statistical entropies and an analysis of some of the observed dimer features are offered.

$\text{YF}$  has been identified as a decomposition product of  $\text{YF}_3$  and has been produced in a number of novel ways. Its absorption spectrum has been obtained and compared with known gas phase data. The absorption results indicate that there are two sites in the matrix and a simple model has been proposed to explain a number of interesting matrix effects. Laser induced emission from the  $\text{C}^1\Sigma^+$  state has been well characterized and analysed to yield molecular constants from which Franck-Condon factors have been determined and used to compare observed and calculated intensities. Some preliminary emission results from the  $\text{B}^1\Pi$  state have also been reported. The shading of the absorption and emission bands was attributed to phonon sidebands and the varying degree of vibrational relaxation observed in the emission spectra was related to the ability of  $\text{YF}$  to exchange vibrational energy with other guests in the matrix.

Finally, several preliminary lifetime experiments were described and the results indicated that the molecules appeared to be undergoing singlet-triplet excited state inter-system crossing and a

possible mechanism was proposed which indicated that the lifetime associated with the molecules returning from the triplet state to the singlet ground state was on the order of minutes. Further experimental work to confirm these results and to elucidate the mechanism that produces these long lifetimes is in progress.

Spectroscopic Studies of Matrix Isolated  
High Temperature Molecules

by

Michael Louis Lesiecki

A THESIS

submitted to

Oregon State University

in partial fulfillment of  
the requirements for the  
degree of

Doctor of Philosophy

Completed July 1975

Commencement June 1976

APPROVED:

*Redacted for Privacy*

---

Associate Professor of Chemistry  
in charge of major

*Redacted for Privacy*

---

Chairman of Department of Chemistry

*Redacted for Privacy*

---

Dean of Graduate School

Date thesis is presented July 11, 1975

Typed by Mary Jo Stratton for Michael Louis Lesiecki

## ACKNOWLEDGEMENT

I would like to thank Dr. Joseph W. Nibler for his encouragement, help, friendship and for shouting Horray! when good results came through. Joe has endeavored to teach experimental techniques and theories and he has stressed the need to be thorough and to do research of the highest possible quality. If I have learned a fraction, then I will be better for it. My thanks again.

To my wife Carol, I thank you for the help with the typing, figures and all the other things you have done for me in the preparation of this thesis. Not only that, but you have always been patient and most encouraging and understanding about this work and I thank you more than words can say.

It has been my pleasure to have the friendship and help of Lou Allamandola and Hossein Rojhtalab and many of the graduate students, faculty and staff at Oregon State. My thanks also to Jim Shirk with whom I first started in this field. I would also like to express my appreciation to my parents who have always encouraged me throughout my schooling.

I would like to thank Dr. Wm. Hayden Smith of Princeton University for his computation of the Franck-Condon factors for YF reported here. In addition, I am grateful for financial support from the National Science Foundation.

## TABLE OF CONTENTS

	<u>Page</u>
I. INFRARED AND RAMAN SPECTRA AND STRUCTURE OF MATRIX ISOLATED $\text{PrF}_3$ AND $\text{LaF}_3$	1
Introduction	1
Experimental	4
Results and Discussion	11
$\text{PrF}_3$	11
$\text{LaF}_3$	15
Conclusions	15
II. INFRARED AND RAMAN SPECTRA AND STRUCTURE OF MATRIX ISOLATED THALLOUS HALIDE DIMERS: $\text{Tl}_2\text{F}_2$ and $\text{Tl}_2\text{Cl}_2$	19
Introduction	19
Experimental	22
Results	27
Thallos Fluoride	27
Thallos Chloride	31
Discussion	34
Symmetry and Vibrational Assignments	34
Structural Parameters for $\text{Tl}_2\text{Cl}_2$	39
Absolute Entropy Calculations	41
Force Field Calculations	43
Symmetry Coordinates and G Matrices	43
Force Constants	45
Amplitudes of Vibration for $\text{Tl}_2\text{F}_2$	53
Summary	54
III. INFRARED AND RAMAN SPECTRA AND STRUCTURE OF MATRIX ISOLATED MAGNESIUM DIHALIDES: $\text{MgF}_2$ , $\text{MgCl}_2$ , $\text{MgBr}_2$ , $\text{MgI}_2$	57
Introduction	57
Experimental	60
Results	62
$\text{MgF}_2$ in Krypton	62
$\text{MgF}_2$ in Argon	69
$\text{MgF}_2$ in Nitrogen	71
$\text{MgCl}_2$ in Argon	73
$\text{MgCl}_2$ in Nitrogen	79

	<u>Page</u>
MgBr <sub>2</sub> in Argon	81
MgI <sub>2</sub> in Argon	86
Discussion	89
Frequency Assignments and Structural Implications	89
Force Constants and Bonding	93
Absolute Entropy Calculations	97
Analysis of the Dimer Spectra	98
Summary	101
 IV. ABSORPTION SPECTRUM, LASER EXCITED EMISSION SPECTRUM AND PRELIMINARY VIBRATIONAL LIFETIME EXPERIMENTS FOR MATRIX ISOLATED YF	       103
Introduction	103
Experimental	105
Results	106
Absorption and Laser Excited Emission Spectra and Molecular Constants of YF	106
Franck-Condon Factors	118
Discussion	120
Matrix Effects	120
Phonon Interactions	120
Site Effects	121
Vibrational Relaxation	126
Preliminary Vibrational Lifetime Studies	128
Summary	136
 BIBLIOGRAPHY	 138
 APPENDICES	
Appendix I. Calibration and Use of the Crystal Oscillator	144
Appendix II. Cary 15 Calibration	147
Appendix III. Determination of the Relative Spectral Response of the Cary 82	150

## LIST OF FIGURES

<u>Figure</u>		<u>Page</u>
1	Schematic of cold cell, high temperature furnace and laser illumination geometry.	5
2	Cold cell-furnace assembly positioned on reflection stage.	7
3	Vibrational spectra of $\text{PrF}_3$ isolated in argon.	12
4	Vibrational spectra of $\text{LaF}_3$ isolated in argon.	16
5	Schematic of deposition rate monitor.	24
6	Vibrational spectra of $\text{TlF}/\text{Tl}_2\text{F}_2$ isolated in argon.	28
7	Vibrational spectra of $\text{TlCl}/\text{Tl}_2\text{Cl}_2$ isolated in argon.	32
8	Effect of annealing on the vibrational spectra of $\text{TlCl}/\text{Tl}_2\text{Cl}_2$ .	33
9	Force fields, calculated and experimental mean amplitudes of vibration for $\text{Tl}_2\text{F}_2$ .	47
10	Force field for $\text{Tl}_2\text{Cl}_2$ .	50
11	Vibrational spectra of $\text{MgF}_2$ isolated in krypton.	63
12	Expanded scale of the infrared trace of Fig. 11.	68
13	Vibrational spectra of $\text{MgF}_2$ in argon.	70
14	Vibrational spectra of $\text{MgF}_2$ in nitrogen.	72
15	Vibrational spectra of $\text{MgCl}_2$ in argon.	74

<u>Figure</u>		<u>Page</u>
16	Expanded scale of the infrared trace of Fig. 15.	77
17	Vibrational spectra of $\text{MgCl}_2$ isolated in nitrogen.	80
18	Vibrational spectra of $\text{MgBr}_2$ isolated in argon.	82
19	Vibrational spectra of $\text{MgI}_2$ isolated in argon.	87
20	Absorption spectra for YF in argon.	108
21	Emission spectra ( $\text{C}^1\Sigma^+ \rightarrow \text{X}^1\Sigma^+$ ) of YF in argon.	112
22	Emission spectra ( $\text{B}^1\Pi \rightarrow \text{X}^1\Sigma^+$ ) of YF in argon.	117
23	Fluorescence of YF in argon.	123
24	Site effects on the energy levels of YF.	124
25	Observed anti-Stokes emission for YF.	129
26	Observed change in the YF emission intensity during vibrational lifetime experiments.	130
27	Variation of emission intensity with wavelength compared to $\text{B}^1\Pi$ absorption spectrum.	132
28	Observed change in emission intensity with time.	133
29	Possible mechanism for observation during vibrational lifetime measurements.	135

## LIST OF TABLES

<u>Table</u>		<u>Page</u>
1	Vibrational frequencies of $\text{PrF}_3$ and $\text{LaF}_3$ in argon.	17
2	Fundamental frequencies of thallos fluoride and chloride in argon.	38
3	Symmetry coordinates and symmetrized F and G matrix elements for $\text{Tl}_2\text{X}_2$ .	44
4	Force constants for $\text{Tl}_2\text{F}_2$ .	46
5	Observed spectral features for $\text{MgF}_2$ .	64
6	Observed spectral features for $\text{MgCl}_2$ .	75
7	Observed and calculated fundamental frequencies for $\text{MgCl}_2$ in argon.	78
8	Observed spectral features for $\text{MgBr}_2$ and $\text{MgI}_2$ .	83
9	Observed and calculated fundamental frequencies for $\text{MgBr}_2$ and $\text{MgI}_2$ in argon.	85
10	Fundamental frequencies and force constants for the magnesium dihalides in argon.	90
11	Absolute entropies for the magnesium dihalides.	97
12	Calculated and observed frequencies for $\text{M}_2\text{X}_4$ species.	99
13	Comparison of gas with matrix absorptions for YF.	109
14	Deslandres table for YF.	113
15	Molecular parameters for gaseous and matrix isolated YF.	114

Table

Page

16

Comparison of observed and calculated  
relative emission intensities for YF.

119

# SPECTROSCOPIC STUDIES OF MATRIX ISOLATED HIGH TEMPERATURE MOLECULES

## I. INFRARED AND RAMAN SPECTRA AND STRUCTURE OF MATRIX ISOLATED $\text{PrF}_3$ AND $\text{LaF}_3$

### Introduction

Infrared matrix isolation spectroscopy has proven to be a valuable technique in the study of unstable species, but corresponding Raman spectra have generally not been observed. With the advent of the laser source, matrix isolation Raman spectroscopy, although difficult due to the inherent weakness of the effect and the dilute conditions of the matrix, has become feasible and a number of papers have appeared in the literature since 1971. Among others, Shirk and Claassen (1), Ozin (2) and coworkers, and Andrews (3) have pioneered in the development of the technique. Raman spectroscopy, supplemented by infrared results, can give the complete vibrational spectrum of a molecule, aid in the assignment of vibrational frequencies, and make definite conclusions possible regarding the molecular structure. For example, infrared studies of  $\text{N}_2\text{H}_2$  (formed as a discharge product of  $\text{N}_2\text{H}_4$ ) could not definitely assign the observed frequencies and were inconsistent as to whether  $\text{N}_2\text{H}_2$  existed in the "trans" form or as a mixture of "cis" and "trans." To resolve these conflicts, Bondybey and Nibler (4) conducted an infrared and Raman

study of matrix isolated  $N_2H_2$  and were able to definitely assign the five in-plane modes of  $N_2H_2$  and conclude that the structure was that of the "trans" form. As a second example, Ozin (2) has studied matrix isolated  $XeCl_2$  (formed in a microwave discharge of a mixture of Xe and  $Cl_2$ ) and has observed one strong band characteristic of the totally symmetric Xe-Cl stretching mode and from the non-coincidence with the two previously observed infrared bands (5) was able to confirm the linear  $D_{\infty h}$  structure proposed in the matrix infrared study. In one further example, Andrews (3) has studied reactions of lithium metal atoms with oxygen molecules to form the new chemical species  $Li^+O_2^-$ . He has assigned a  $C_{2v}$  triangular structure to the molecule on the basis of the near agreement between the 0-0 stretching mode for  $LiO_2$  and the  $O_2^-$  fundamental and the observation of sharp triplet bands in the reaction of a mixture of  $^{16}O_2$ ,  $^{16}O^{18}O$ ,  $^{18}O_2$  with  $^7Li$  atoms at high dilution in argon.

As indicated above, a comparison of the infrared and Raman spectra of a molecule can allow one to make definite vibrational assignments and predictions about the molecular structure. In this work, we have studied the infrared and Raman spectra of matrix isolated thermally unstable species whose structures are: 1) unknown, 2) not definitely known since the infrared studies were inconclusive regarding the molecular structure, or 3) not definitely known since the infrared results were contradictory to conclusions of other

experiments such as electric deflection or electron diffraction. In the first part of this research, we have obtained the infrared and Raman spectra of matrix isolated  $\text{PrF}_3$  and  $\text{LaF}_3$  and were able to assign the observed vibrational frequencies and determine the molecular structures of the molecules. Also, in subsequent chapters we will discuss infrared and Raman structural studies on thallium fluoride and chloride and the magnesium halides.

Recent infrared matrix studies of the lanthanide rare earth trifluorides by Wesley and DeKock (6) (WD) and Hauge et al. (7, 8) (H) are at variance as to the molecular geometry of these species. Of particular interest, is the spectrum of  $\text{PrF}_3$  reported by (WD) in which they observed two intense infrared stretching absorptions ( $\nu_1 = 524$ ,  $\nu_3 = 458 \text{ cm}^{-1}$ ) which seemed best interpreted in terms of a non-planar  $C_{3v}$  structure. Support for this interpretation came from the frequencies of the asymmetric stretch,  $\nu_3$ , and one of the bending modes at  $99 \text{ cm}^{-1}$ , since these appeared unusually low in comparison with values for the other trifluorides. (H) has observed four infrared absorptions for the trifluorides of La, Ce, Nd, Eu and Gd and has proposed that the molecules in this group are non-planar. They also predict that  $\text{PrF}_3$  is non-planar, and on the basis of the observed frequencies of  $\text{CeF}_3$  and  $\text{NdF}_3$  they conclude that the symmetric and asymmetric stretch should be observed in argon at  $526$  and  $496 \text{ cm}^{-1}$  respectively. However, the available electron

diffraction data (9) on these series of compounds have been interpreted in terms of planar geometries, and recent electric deflection experiments by Kaiser et al. (10) (K) indicate a planar  $D_{3h}$  structure for  $\text{PrF}_3$  in the gas phase. In view of this, the implied structural change in going to the matrix would be quite unusual and hence a Raman matrix isolation experiment was undertaken to check the infrared results. Since the symmetric stretch,  $\nu_1$ , should have high Raman intensity and should be polarized, the identification of the  $542 \text{ cm}^{-1}$  or  $458 \text{ cm}^{-1}$  band as  $\nu_1$  would be convincing evidence for a pyramidal structure in the work of (WD) or alternatively the observation of  $\nu_1$  near  $526 \text{ cm}^{-1}$  would confirm the predictions of (H).

In addition, the electric deflection experiments of (K) indicated a non-planar gas phase structure for  $\text{LaF}_3$ , while (WD) conclude a planar  $D_{3h}$  structure on the basis of the observation of three infrared bands. On the other hand, (H) have observed four infrared bands ( $\nu_1 = 513 \text{ cm}^{-1}$  in argon) for  $\text{LaF}_3$  and predict a  $C_{3v}$  structure. Again, the combination of infrared data and the observation of  $\nu_1$  in the Raman should allow one to determine the structure of matrix isolated  $\text{LaF}_3$ .

### Experimental

Figure 1 is a schematic of the cold cell, high temperature furnace, and laser illumination geometry. The sample is generated

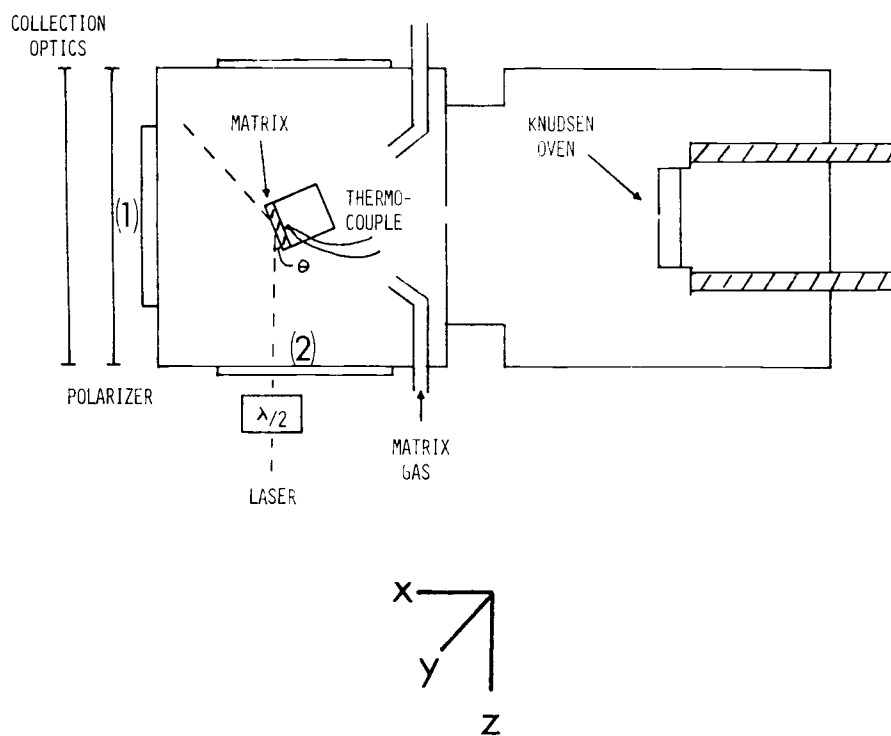


Figure 1. Schematic of cold cell, high temperature furnace and laser illumination geometry.

from a resistively heated tantalum or graphite Knudsen cell (2 cm in length, 0.8 cm i.d.) of typically 1.0 mm wall thickness and 1.0 mm diameter effusion hole. The Knudsen cell is positioned approximately 12 cm from the cold tip and the molecular beam encounters a 0.8 cm diameter hole in a radiation shield positioned approximately 3 cm from the tip. A water-cooled vacuum shroud surrounds the Knudsen cell assembly and an externally controlled shutter may be positioned 4 cm from the cold tip to act as a beam stop. After the molecular beam passes through the radiation shield it is co-condensed with the matrix gas entering from a 1 mm i.d. copper tube terminating approximately 3 cm from a rotatable 2.5 x 2.5 x 5.0 cm polished aluminum cold tip. The tip is bored out (2 cm i.d.) along the long axis to reduce the thermal mass and it is cooled to 12-14<sup>o</sup>K by an Air Products Displex refrigerator. The temperature is monitored by a hydrogen vapor pressure thermometer and by a Au-Fe/chromel thermocouple attached to the tip.

The mirror-like tip and three optical ports allow both infrared and Raman spectra to be recorded for the same sample. In a typical experiment, the cold cell-furnace assembly is positioned on the reflection stage in the infrared instrument (Perkin Elmer 180) as shown in Figure 2. The sample is deposited on the cold tip which is then rotated 180<sup>o</sup> to intercept the infrared beam. With the globar source and thermopile detector, window #1 is CsI, capable of covering

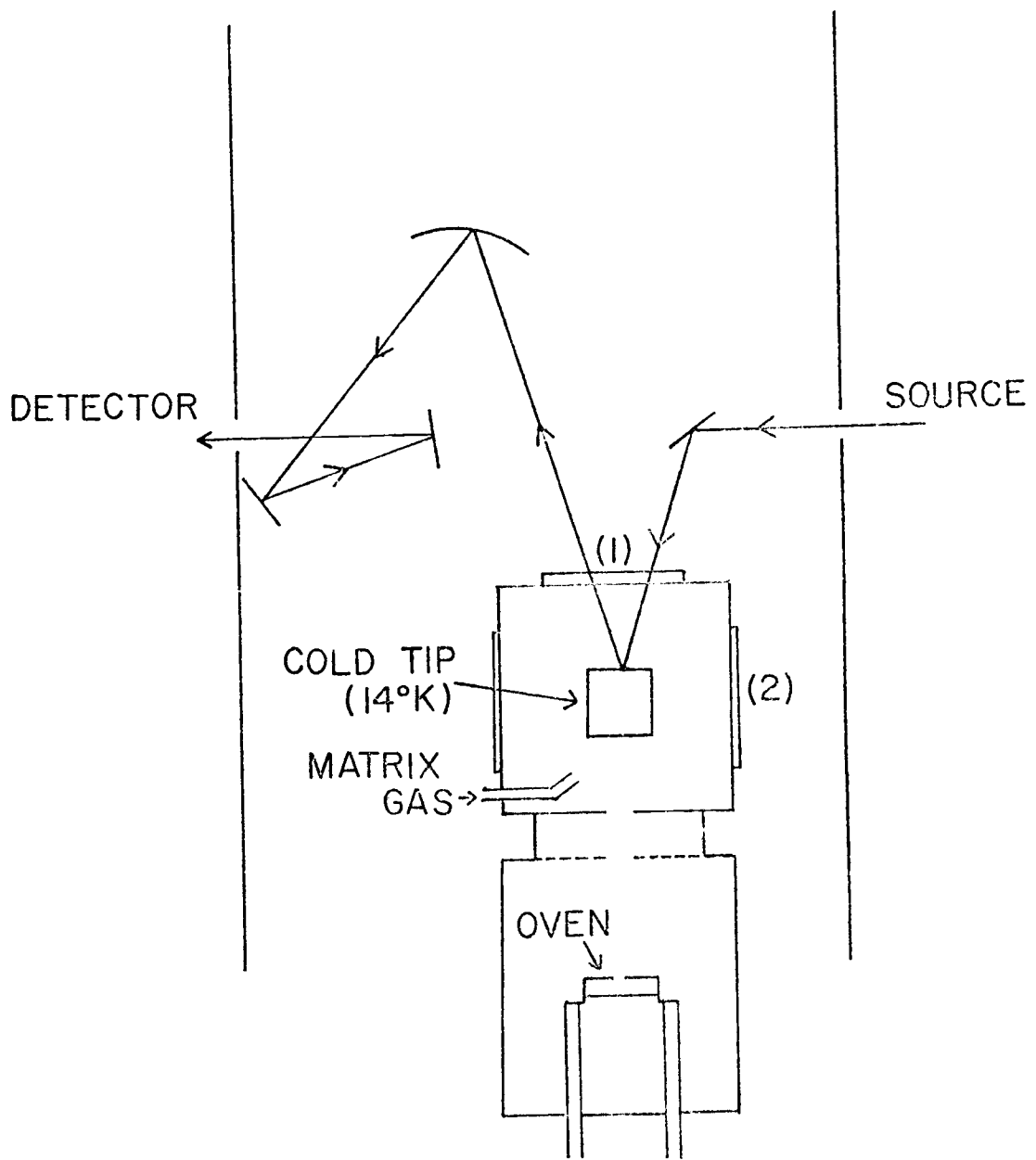


Figure 2. Cold cell - furnace assembly positioned on reflection stage in the infrared instrument.

the range  $200-4000\text{ cm}^{-1}$ . For far infrared scans ( $200-32\text{ cm}^{-1}$ ) we employ a mercury source, TGS detector and a high density polyethylene disc as window #1. To improve the transmission of this polyethylene window the thickness of the center circle (2.5 cm diameter) is reduced from 3 to 1.5 mm. After a suitable deposit, infrared scans of the sample are obtained and then the cold cell-furnace assembly is positioned horizontally on the x-y translational stage of the Cary 82 Raman spectrophotometer. A glass window, #2, serves as the optical port for the laser radiation exciting along the z-axis (see Figure 1) and the scattered radiation is viewed through window #2 along the x-axis. The geometry dictates that the exciting argon ion laser radiation enter via window #2 and the scattering radiation be viewed through window #1. Therefore, infrared scans using a CsI window (transparent to the Raman scattered light) may be directly compared to Raman scans of the same sample. Argon and krypton ion gas lasers as well as a dye laser (commonly using Rhodamine-6G) are used as sources in the Raman experiment. Sample positioning is quite important; to obtain the maximum signal in a Raman scan the tip angle and cell position must all be optimized with respect to the focal point of the exciting laser and the focal point of the collection lens.

The advantages of the above-mentioned infrared reflection arrangement are considerable (11):

- 1) Deposition times are halved since for transparent matrices the beam transverses the sample twice.
- 2) As stated, infrared and Raman experiments are possible on the same sample and using the Raman geometry, laser excited fluorescence spectra may also be obtained.
- 3) The four faces of the cold tip make it possible to do four separate experiments (to optimize deposit conditions, for example) without warming up the cold tip.
- 4) The reflection arrangement is nearly as efficient as a transmission experiment since the reflection stage loses only 10% of the energy if a mirror rather than the cold cell assembly is placed in the sample position. In addition, a typical transmission experiment with two external CsI windows plus a CsI substrate gives approximately 65% transmission, while the reflection arrangement with one external CsI window (and a double pass through the sample) gives approximately 60% transmission. Also, in the far infrared the aluminum substrate replaces the silicon window giving a considerable gain in energy-starved situations since the silicon window is not particularly transparent.
- 5) The thermal conductivity of the aluminum substrate is higher than that of CsI allowing better isolation in experiments involving rapid depositions. Isolation is also improved for deposits of

high temperature species, such as  $\text{PrF}_3$  and  $\text{LaF}_3$ , where the thermal load on the matrix is higher.

- 6) Substrate surfaces other than aluminum can be used with molecules that might react with aluminum or CsI.

Prior to a typical experiment, the cold cell and furnace assembly were evacuated to a pressure of approximately  $1 \times 10^{-5}$  torr and the sample was heated in the Knudsen cell under vacuum to slightly above the anticipated deposit temperature to outgas the sample. For both  $\text{PrF}_3$  (99.9%, Michigan Chemical Corp.) and  $\text{LaF}_3$  (99.9%, Alfa Inorganics) the outgas temperature was approximately  $1350^\circ\text{C}$  while deposit temperatures were in the range  $1300$ - $1350^\circ\text{C}$ ; these temperatures were measured by viewing the Knudsen cell through an optical port in the rear of the furnace housing with an optical pyrometer. The matrix gas was generally deposited at a rate of 5 to 15 mM/hr as measured by a calibrated flow meter and deposit times were of the order of 1 to 30 hours. To minimize the formation of dimers or higher order polymers, initial deposits of short duration were conducted in the infrared. Because of the greater sensitivity of the infrared measurement, the optimum isolation conditions to favor the monomeric species could quickly be determined, and then extended deposits made for a Raman scan. Depolarization measurements are possible for glassy matrix films (12), slow deposition rates and visual examination of the matrix surface during the deposit (with subsequent

adjustment of deposit conditions) tend to give the most reliable results. In our experiments, depolarization ratios were measured by rotating the vector of the exciting radiation with a half-wave plate and analyzing with the polarizer in a fixed position. In the i(pa)s notation with the axis labeled as in Figure 1, a parallel scan would be z(yy)x and a perpendicular scan would be z(xy)x.

### Results and Discussion

#### PrF<sub>3</sub>

Trace a of Figure 3 presents the infrared spectrum of PrF<sub>3</sub>, while traces b and c show Raman bands shifted by 526, 458 and 99 cm<sup>-1</sup> from the 5145 Å and 4880 Å laser lines. The extra features observed with the higher energy 4880 Å line are fluorescence bands of PrF<sub>3</sub>, probably resulting from excitation to the <sup>3</sup>P<sub>1</sub>, <sup>3</sup>P<sub>0</sub> or <sup>1</sup>I<sub>6</sub> states (these states are likely to be accessible with this line but not with the 5145 Å line (13)). Comparison of the Raman and infrared features is quite revealing. Most strikingly, the strong, polarized ( $\rho = .35$ ) Raman line proves that  $\nu_1$  occurs at 526 cm<sup>-1</sup> and since this band is nearly coincident with a weak feature at 525 cm<sup>-1</sup> in the infrared we now have a basis for preferring a pyramidal C<sub>3v</sub> structure. The other depolarized Raman bands at 458 and 99 cm<sup>-1</sup> are coincident with infrared features and hence must be the E modes  $\nu_3$  and  $\nu_4$ . The

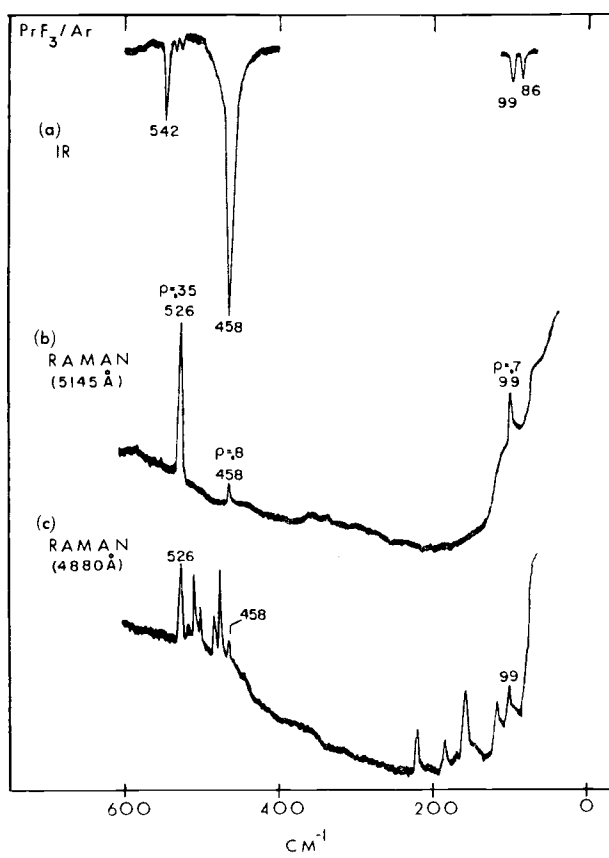


Figure 3. Vibrational spectra of  $\text{PrF}_3$  isolated in an argon matrix at  $14^\circ\text{K}$ .

remaining IR feature, the  $A_1$  mode at  $86\text{ cm}^{-1}$ , is also Raman allowed and there is an indication of this band on the shoulder of the exciting line background in trace b.

The question of the IR band at  $542\text{ cm}^{-1}$  remains. An explanation in terms of dimers or impurities is not favored since the relative IR intensities of the  $542$  and  $458\text{ cm}^{-1}$  features remain constant for different ovens, oven temperatures and matrix ratios. A possible explanation in terms of Jahn-Teller splitting of  $\nu_3$  resulting from a degenerate E ground state is discounted because the early work of Van Vleck (14) clearly indicates that this splitting will not be significant for the rare-earths.

Two possible explanations occur to us. The first is that the  $542\text{ cm}^{-1}$  transition is simply an  $A_1 \rightarrow A_2$  electronic transition between two of the sublevels ( $2A_1$ ,  $A_2$ ,  $4E$ ) which result when the ground  $^3H_4$  state of  $\text{Pr}^{+3}$  is placed in a  $C_{3v}$  ligand field. Such levels are expected to be spread over a range of about  $500\text{ cm}^{-1}$  and some transitions have been observed below  $100\text{ cm}^{-1}$  for solid  $\text{PrF}_3$  (15). However, the intensity does seem high for the small amount of  $\text{PrF}_3$  present in the matrix and moreover, similar transitions could be expected for the other lanthanide trifluorides. Finally, this explanation does not account for the low value of  $\nu_3$  for  $\text{PrF}_3$  relative to the other trifluorides.

An alternate explanation which we favor is that  $\nu_3(E)$  is perturbed from its expected location at  $493 \text{ cm}^{-1}$  (Figure 2 ref. 6) or  $496 \text{ cm}^{-1}$  (Figure 2 ref. 7) by a resonance interaction with an E electronic level, leading to two levels located at  $458 \text{ cm}^{-1}$  (E) and  $542 \text{ cm}^{-1}$  ( $A_1 + A_2$ ). Evidence for this explanation is two-fold: (a)  $\nu_3$  in  $N_2$  is greater than  $\nu_3$  in Ar and (b) the  $542$  and  $458 \text{ cm}^{-1}$  transitions are extremely sensitive to  $N_2$  doping (up to 10%) of the Ar matrix. Both observations are contrary to results for the lanthanide trifluorides and both suggest a sensitive matrix tuning of two resonant levels. Apparently the resonance splitting is much less ( $488 - 470 = 18 \text{ cm}^{-1}$ ) in  $N_2$  than in Ar ( $542 - 458 = 84 \text{ cm}^{-1}$ ).

However, this assumption alone does not explain the observation of the two IR bands at  $542$  and  $458 \text{ cm}^{-1}$ . These activities can only occur if the ground state is E -- use of  $A_1$  or  $A_2$  ground states yields only one IR active transition to the resonating levels. The E ground state also allows Raman activity for these two transitions which explains the Raman band at  $458 \text{ cm}^{-1}$  and it would not seem too surprising if the medium intensity  $542 \text{ cm}^{-1}$  band in the infrared has a very small Raman intensity. This picture also explains nicely why only the IR spectrum of  $PrF_3$  (and possibly  $NdF_3$ ) is unusual in the lanthanide trifluorides since it requires not only a degenerate ground state but also an electronic state in resonance with  $\nu_3$  -- an occurrence expected to be rare.

LaF<sub>3</sub>

Figure 4 presents the infrared (a) and Raman (b) spectra of LaF<sub>3</sub>. The strong polarized ( $\rho = 0.4$ ) Raman band at  $514 \text{ cm}^{-1}$  is assigned to the symmetric stretching mode and is coincident with a weak feature in the infrared, supporting a pyramidal C<sub>3v</sub> structure. In addition, the Raman and infrared observation of both bending modes at  $120$  and  $84 \text{ cm}^{-1}$  and their Raman depolarization ratios also require a C<sub>3v</sub> structure. The depolarized ( $\rho = 0.8$ ) band at  $120 \text{ cm}^{-1}$  can be assigned to the E bending mode and the observed depolarization ratio ( $\rho = 0.4$ ) of the  $84 \text{ cm}^{-1}$  band indicates that it is the A<sub>1</sub> bending mode. The absence of the asymmetric stretching mode at  $478 \text{ cm}^{-1}$  in the Raman is not too surprising since this band should have a weak intensity.

Conclusions

From the observed infrared and Raman spectra we have been able to deduce non-planar C<sub>3v</sub> structures for PrF<sub>3</sub> and LaF<sub>3</sub>. Also, we have assigned the observed frequencies, in an argon matrix, for both species and the results are presented in Table I.

Our structural conclusions confirm the observations for LaF<sub>3</sub> in the infrared matrix work of (H) and agree with their predictions for PrF<sub>3</sub>. In addition, our observation of  $\nu_1$  for both species allows the

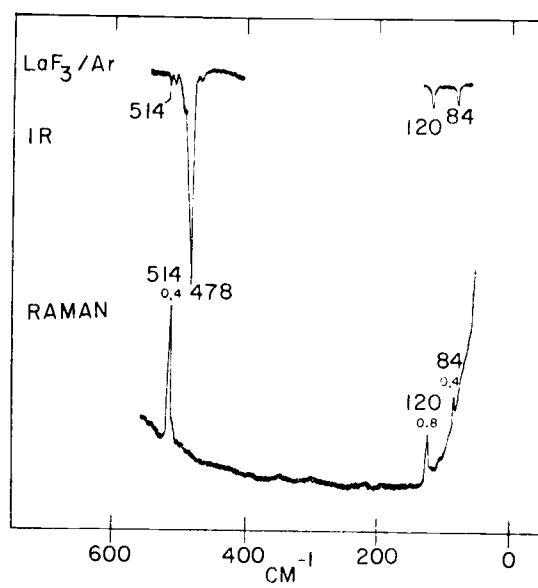


Figure 4. Vibrational spectra of  $\text{LaF}_3$  isolated in an argon matrix at  $14^\circ\text{K}$ .

Table 1. Vibrational frequencies of  $\text{PrF}_3$  and  $\text{LaF}_3$  isolated in argon matrices.<sup>a</sup>

	Frequency ( $\text{cm}^{-1}$ )	Identification
$\text{PrF}_3$ ( $C_{3v}$ )	526	$\nu_1$ ( $A_1$ )
	86	$\nu_2$ ( $A_2$ )
	458	$\nu_3$ (E)
	99	$\nu_4$ (E)
	542	see text
$\text{LaF}_3$ ( $C_{3v}$ )	514	$\nu_1$ ( $A_1$ )
	84	$\nu_2$ ( $A_1$ )
	478	$\nu_3$ (E)
	120	$\nu_4$ (E)

<sup>a</sup>Frequencies are believed accurate to  $\pm 1 \text{ cm}^{-1}$ .

work of (WD) to be reinterpreted in terms of a non-planar geometry. On the other hand, our results disagree with the electron diffraction data which have proposed a planar  $D_{3h}$  configuration for these species. However, high temperature electron diffraction data often have large uncertainties deriving from thermal amplitudes and in addition, this technique has been shown to be insensitive to the non-linear geometries of  $\text{CaF}_2$ ,  $\text{SrF}_2$ , and  $\text{BaF}_2$ . This suggests that the non-planarity of the high temperature trihalide species might also escape detection.

Our results for  $\text{LaF}_3$  also agree with the high temperature gas phase electric deflection experiment (10) which indicates an electric

dipole moment (therefore, a non-planar geometry). However, the electric deflection experiment for  $\text{PrF}_3$  did not indicate an electric dipole moment (therefore, a planar geometry), a result in direct disagreement with our conclusions. A satisfactory explanation for this discrepancy is not readily apparent but it might be noted that as (K) has pointed out, it is not possible to rule out a non-planar  $C_{3v}$  symmetry as the high polarizabilities of the lanthanides could mask the presence of a small dipole moment. Also, it is conceivable that matrix forces might distort a planar configuration somewhat to give a pyramidal structure.

Further Raman studies on the remaining molecules in the lanthanide series are indicated before definite conclusions can be reached regarding the structure and bonding of these species. At this time, the work of (WD), (H) and (K) is at varying stages of disagreement and a Raman matrix isolation study of the remaining lanthanides would resolve the discrepancies among their results. Once this has been done, the question of f-orbital participation or 5d-6s-orbital interaction (as discussed by the above authors) as being responsible for the geometry of the lanthanides can perhaps be more easily answered.

II. INFRARED AND RAMAN SPECTRA AND STRUCTURE OF  
MATRIX ISOLATED THALLOUS HALIDE  
DIMERS:  $Tl_2F_2$  AND  $Tl_2Cl_2$

Introduction

The structure and chemical bonding in  $Tl_2F_2$  and the other thallos halide dimers have been much discussed in the recent literature. If the bonding is largely ionic, one would expect a  $D_{2h}$  planar rhombic structure such as that found for alkali halide dimers. However, on the basis of vapor pressure and mass spectroscopic measurements, Keneshea and Cubicciotti concluded that a linear  $D_{\infty h}$  structure gave better agreement with the experimental entropy values for  $Tl_2F_2$ ,  $Tl_2Cl_2$  and  $Tl_2Br_2$  (16, 17). They also noted a significant  $Tl_2^+$  feature in the mass spectra of these compounds, an observation which further seemed to support a linear model with a strong covalent Tl-Tl bond. Subsequently, the infrared spectra of matrix isolated  $Tl_2F_2$  and  $Tl_2Cl_2$  were examined by Brom and Franzen (18) and two infrared features in the region from 33 to 4000  $cm^{-1}$  were attributed to  $Tl_2F_2$  and to  $Tl_2Cl_2$ . This observation too was taken to favor a  $D_{\infty h}$  model since three infrared active fundamentals would be predicted for the rhombic configuration. In addition, Brom and Franzen presented entropy calculations and a bonding discussion to support their argument for a linear structure.

In 1973, Dehmer, Berkowitz and Cusachs (19) reported the photoelectron spectrum of  $\text{Tl}_2\text{F}_2$  and compared their observations with those predicted from semiempirical calculations based on both  $D_{\infty h}$  and  $D_{2h}$  models. These results also were more consistent with a linear structure although the previous arguments based on entropy calculations and on the  $\text{Tl}_2^+$  mass spectral peaks were not compelling in their view.

In 1974 two molecular beam experiments were published on  $\text{Tl}_2\text{F}_2$ . Fickes, Slater, Becker and Stern (20) examined the scattering of low energy electrons by  $\text{Tl}_2\text{F}_2$  beams and found evidence for an instantaneous dipole of several Debye. They noted that such an observation need not necessarily imply a polar molecule since the dipole could arise from a bending mode of large amplitude ( $\sim 30^\circ$ ). However they did indicate that such a large amplitude could not be easily reconciled with a stiff linear structure, the rigidity being implied by the high frequency reported by Brom and Franzen (18) for the bending mode. Subsequently Muentzer (21) carried out a molecular beam electric deflection experiment which showed conclusively that the instantaneous dipole must be of vibrational origin since the equilibrium structure for the dimer was nonpolar. Of course, no choice between  $D_{2h}$  and  $D_{\infty h}$  models could be made from this result.

Although the preponderance of data seemed to be compatible with the linear structure, in 1974 we learned of some preliminary

electron diffraction data which seemed to be best interpreted in terms of the rhombic structure (22). This stimulated us to conduct simultaneous infrared and Raman matrix experiments on  $Tl_2F_2$  and  $Tl_2Cl_2$  since previous Raman matrix studies (23) in our laboratory have shown that structural conclusions reached on the basis of infrared spectroscopy alone are often subject to question. Of course, for an  $X_2Y_2$  molecule the number of Raman active bands does not distinguish between  $D_{\infty h}$  and  $D_{2h}$  symmetries since three Raman active bands (two polarized) are predicted for both models. However, if the  $Tl_2F_2$  molecule is linear with a strong covalent Tl-Tl bond, one would expect the Raman spectrum to be dominated by scattering at the low Tl-Tl stretching frequency. Thus we felt confident that an unambiguous structural conclusion would be possible in this case and indeed the present results show this to be so. During the preparation of this manuscript, the published electron diffraction results (24) for  $Tl_2F_2$  became available to us and these structural parameters and vibrational amplitudes have been used in our normal coordinate analysis for this molecule. We have repeated the entropy calculations and a resolution of almost all of the conflicting data on  $Tl_2F_2$  is offered. In addition spectra for  $Tl_2Cl_2$  are presented and from these results, there can be little doubt that this molecule has the same symmetry as  $Tl_2F_2$ .

## Experimental

In the present study of thallium fluoride and chloride, conventional techniques for the matrix isolation of high temperature species were used. The experimental apparatus and procedure is the same as that described in Chapter I and exceptions or additions particular to these experiments will be noted here. Prior to a typical experiment, the cold cell and furnace were evacuated to a pressure of approximately  $1 \times 10^{-5}$  torr and the sample was outgassed in a graphite Knudsen cell under vacuum to slightly above the anticipated deposition temperature (approximately  $300^{\circ}\text{C}$  for both compounds). The deposition rates of both thallium fluoride (Cerac, 99.9%) and thallium chloride (Alpha-Ventron, 99.9%) were adjusted to optimize the monomer:dimer:polymer ratio in the matrix. The degree of isolation,  $M/R$  (mole ratio of matrix gas/metal halide), is an important consideration in determining this ratio. To calculate  $M/R$  the deposit rates of both matrix gas and metal halide must be obtained. The matrix gas was generally deposited at 5 to 15 mM/hr, a rate conveniently measured by a calibrated flowmeter. However, the deposit rate of the metal halide is not so easily obtained. For effusion from a Knudsen cell, the rate can be estimated (25) from the vapor pressure of the species at the effusion temperature. Often, however, such vapor pressure data are unavailable and, moreover, absolute

temperature measurements are not trivial at high temperatures. In addition, even at a fixed temperature we have observed marked decreases in rates of deposition with time because of internal migration of salts to the cooler regions of the Knudsen cell. Such factors clearly demonstrate the need for a more direct monitor of the effusion rate.

One such monitor, a quartz crystal microbalance, is commonly employed for thin film deposits in the optical coating and semiconductor industries. Moskovits and Ozin have briefly described the application of this device in their study of matrix reactions of metal atoms evaporated from filaments (26). We have recently developed a similar, low cost system which we are using to directly monitor effusion rates and offer here some practical observations which may be of use to others interested in this and similar applications.

Figure 5 illustrates our experimental apparatus. The quartz crystal (27) plugs into a socket mounted on a 1/4" brass tube which slides in an Ultra Torr vacuum seal so as to locate the crystal at one of four positions. Position A shields the crystal, B allows the continuous monitoring of the relative effusion rate during matrix deposition, C permits direct sampling of the effusion beam, and D blocks the beam (for outgassing purposes). A direct measurement involves reading the frequency at A, inserting at C for one minute, returning to A and recording the frequency after the crystal has

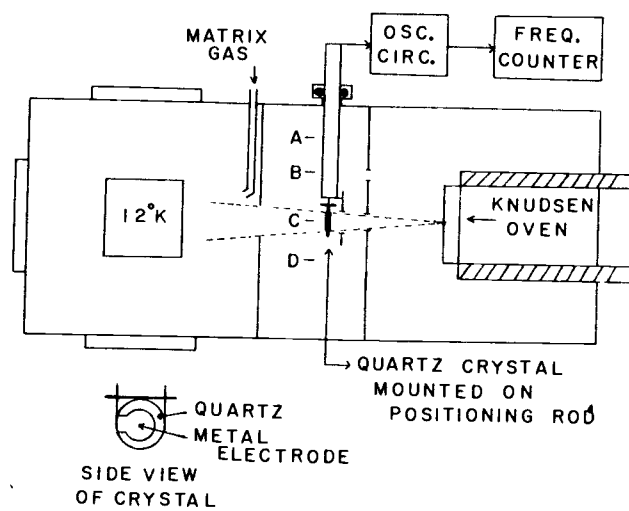


Figure 5. Schematic of deposition monitor for matrix isolation studies.

cooled. This procedure avoids frequency shifts due to temperature variations and also minimized the amount of deposit on the crystal so that it can be used for many experiments before cleaning. When a continuous monitor is desired, the direct rate is first determined and then the crystal is moved to B. After thermal equilibrium is reached, a rate measurement at B is compared to the direct rate to give a scale factor for subsequent monitoring. Since radiation heating is substantial at both B and C, one of the electrodes is thermally (and electrically) grounded via the brass tube to the water-cooled oven housing. With this arrangement, we have operated at effusion temperatures up to  $1500^{\circ}\text{K}$  without difficulty.

The relations between the added mass  $\Delta m$  and the frequency shift  $\Delta f$  is  $\Delta m/A = K\Delta f$  where  $K = \rho d/f_0$ ,  $f_0$  = initial frequency,  $\rho$  = quartz density = 2.65 g/cc,  $d$  = crystal thickness = 0.167 MHz-cm/ $f_0$  for AT cut quartz and  $A$  = oscillating area  $\approx$  electrode area (28). The weight of salt  $w$  which actually passes in one minute through the final (limiting) aperture of area  $A'$  to mix with the matrix gas is then  $w = K\Delta f(CA'\ell_1^2/\ell_2^2)$ . Here  $\ell_1$  and  $\ell_2$  are the distances from the Knudsen source to the crystal and the limiting aperture, respectively, and  $C$  is a factor to correct for the effusion distribution.  $C$  can be calculated using the methods and tables of Miller (25) and is usually close to unity for small values of  $A'$  ( $C = 0.90$  for our Knudsen cell and geometry).

Crystal constants (K) of 17.7 and 5.5 mg/MHz-cm<sup>2</sup> are expected for 5 and 9 MHz crystals respectively and these agree roughly with several experimental values we have measured (12.3 and 14.4 mg/MHz-cm<sup>2</sup> for two different 5 MHz oscillators and 4.7 mg/MHz-cm<sup>2</sup> for a 9 MHz crystal). The latter values were obtained by evaporating NaCl on the crystal electrode area and then dissolving the film for analysis by Na atomic absorption. The resultant plots of  $\Delta f$  vs  $\Delta m$  were linear up to the cutoff point at which the crystals stopped oscillating (typically 7-11 mg/cm<sup>2</sup> for both 5 and 9 MHz oscillators) and tests with NaBr in place of NaCl confirmed that only the deposit mass is important. [Comparable results were also obtained by spraying the masked electrode with a leak-sealant spray (or hairspray), drying, and directly weighing the crystal on a microbalance.] The rather low experimental values of K (=  $\Delta m/A \Delta f$ ) are believed to be due to difficulties in accurately defining the oscillating area A. Ideally, the deposit should just cover the electrode area and, if accurate deposition rates (better than  $\sim 20\%$ ) are desired, calibration with a fixed geometry is probably necessary.

Comparisons of measured NaCl deposit rates with those calculated from the Knudsen equation show only fair agreement. (Measured for solid NaCl at 750°C = 0.053, calculated = 0.21  $\mu\text{g}/\text{sec}$ ; measured for liquid NaCl at 825°C = 1.11, calculated = 1.50  $\mu\text{g}/\text{sec}$ .) These discrepancies are believed to derive from uncertainties in the

vapor pressure, measured temperatures, and the Knudsen cell parameters. Clearly a direct measure of the deposition rate is to be preferred and our experience with the quartz microbalance indicates that this sample system is ideal for such applications (additional details are given in Appendix I).

For these studies of the thallose halides, typical changes in the frequency of the crystal (normally oscillating at 5 MHz) were of the order of 3 to 30 KHz/min, corresponding to deposition rates of  $Tl_2F_2$  of 0.01 and 0.10 mM/hr respectively. The matrix gas flow was adjusted to allow M/R to vary between approximately 100 and 1000 for these deposition rates and typical deposit times were of the order of 2-6 hr.

## Results

### Thallose Fluoride

The vibrational spectra of thallose fluoride isolated in an argon matrix are presented in Figure 6. The Raman results for this typical experiment were recorded after a deposit of 4 hours in which M/R = 100-200. Trace b shows Raman bands shifted from the 5145 Å argon ion laser line while trace a shows a similar scan taken at a higher sensitivity. The identification of low frequency features ( $< 100 \text{ cm}^{-1}$ ) is complicated by the background due to the exciting radiation. However, the inset shows two bands at 93 and 85  $\text{cm}^{-1}$  whose Raman nature

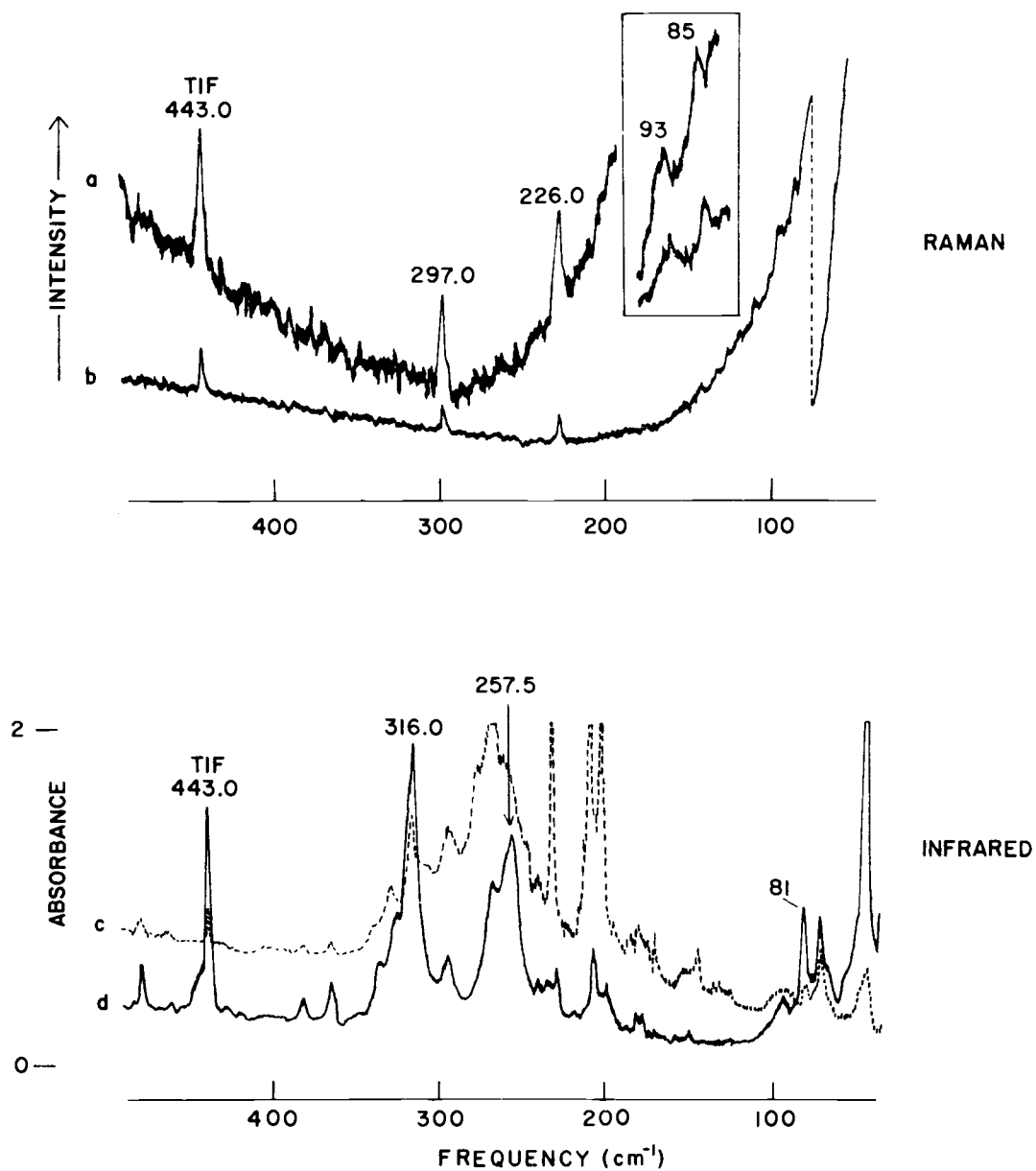


Fig. 6. Vibrational spectra of  $\text{TlF}/\text{Tl}_2\text{F}_2$  in an argon matrix. Raman a: 5145 Å, 200 cps, SBW = 4 cm<sup>-1</sup>; b: 5145 Å, 500 cps, SBW = 2.5 cm<sup>-1</sup>; inset: lower - 4880 Å, upper - 5145 Å, 200 cps, SBW = 2 cm<sup>-1</sup>. Infrared: SBW = 2 cm<sup>-1</sup>, — 14°K, --- after annealing at 40°K followed by recooling to 14°K.

is supported by the fact that their frequencies did not vary with a change in the exciting line (lower trace of inset =  $4880 \text{ \AA}$  excitation, upper trace =  $5145 \text{ \AA}$ ). The bands at  $297$  and  $226 \text{ cm}^{-1}$  occurred with about equal intensity in all experiments and the intensity of the  $443 \text{ cm}^{-1}$  feature, relative to the other Raman lines, increased as the dilution factor was increased. The assignment of the band at  $443 \text{ cm}^{-1}$  to TlF and the remaining Raman bands to  $\text{Tl}_2\text{F}_2$  will be discussed in the following section.

Trace d presents a typical infrared spectrum for a deposit of 3 hr and  $M/R = 100-200$ , and trace c shows the resulting change in the spectrum after allowing diffusion to occur at  $40^\circ\text{K}$  followed by recooling to  $14^\circ\text{K}$ . The infrared trace d agrees well with that of ref. 18 in the region  $500-240 \text{ cm}^{-1}$  and the three prominent bands in that region can be assigned as follows:  $443 \text{ cm}^{-1}$ , TlF;  $316, 257.5 \text{ cm}^{-1}$ ,  $\text{Tl}_2\text{F}_2$ . There are a number of weaker features from  $350$  to  $240 \text{ cm}^{-1}$  and their behavior on diffusion as shown in trace c indicates that they are due to higher polymers of  $\text{Tl}_2\text{F}_2$ . The weak band at  $384 \text{ cm}^{-1}$  and a companion at  $1024 \text{ cm}^{-1}$  are apparently due to isolated  $\text{SiF}_4$ , possibly formed by the  $0.01\%$  Si impurity that was reported in the TlF (Cerac,  $99.9\%$ ) sample analysis. The assignment of the bands at  $482$  and  $368 \text{ cm}^{-1}$  is not readily apparent but these features decreased at a slower rate than either the monomer or dimer bands on warmup to  $40^\circ\text{K}$ .

In ref. 18, the authors report only one absorption, at  $70\text{ cm}^{-1}$ , in argon in the region  $240\text{-}33\text{ cm}^{-1}$ ; this they attribute to a lattice mode of the matrix. We observe several features in this low frequency region; the weak bands at  $231$ ,  $210$  and  $202\text{ cm}^{-1}$  can be assigned to higher order polymers of  $\text{Tl}_2\text{F}_2$  on the basis of their increase in intensity upon warmup as shown in trace c. We also note bands at  $71$  and  $46\text{ cm}^{-1}$  which exhibited intensity variations that were unrelated to each other or to any other bands in the spectrum. These absorptions are believed to be due to induced phonon bands in the argon matrix; their occurrence has been studied by others (29, 30) who report similar frequencies. We also detected a feature at  $81\text{ cm}^{-1}$  whose intensity variation qualitatively parallels that of the  $316$  and  $257.5\text{ cm}^{-1}$  bands for two different deposition rates and for the  $40^\circ\text{K}$  diffusion experiment. More quantitative intensity measurements relative to the  $316$  and  $257.5\text{ cm}^{-1}$  bands upon warmup were complicated due to the overlap of polymer bands which appear on diffusion (Figure 6, trace c). It is conceivable that the  $81\text{ cm}^{-1}$  band could also be a guest-induced lattice mode of the matrix. However, since both the  $71$  and  $46\text{ cm}^{-1}$  bands appear in  $\text{TlCl}$  experiments, whereas the  $81\text{ cm}^{-1}$  feature does not (see below), we feel reasonably confident that the latter absorption should be attributed to  $\text{Tl}_2\text{F}_2$ .

## Thallos Chloride

Figure 7 shows the vibrational spectra of thallos chloride isolated in an argon matrix. The Raman results were recorded after a 4-hr deposit in which M/R = 100-150 and trace a shows Raman bands shifted from the 5145 Å exciting line while the inset shows an expanded display of two areas of the same spectrum recorded at a higher sensitivity. The doublet at 263.0 and 257.1 cm<sup>-1</sup> can be assigned to Tl<sup>35</sup>Cl and Tl<sup>37</sup>Cl respectively since the observed isotopic splitting of 5.9 cm<sup>-1</sup> compares well with the calculated splitting of 6.1 cm<sup>-1</sup>. The doublet at 190.4 and 184.6 cm<sup>-1</sup> and the bands at 131 and 61 cm<sup>-1</sup> may be assigned to Tl<sub>2</sub>Cl<sub>2</sub> and these features were always present with about the same relative intensity in all experiments. Further support for these assignments is presented in Figure 8 which shows the changes in the spectrum after allowing diffusion to occur at 40°K. For the Raman trace of Figure 8 the TlCl doublet at 263 cm<sup>-1</sup> decreases on warmup while the doublet at 190.4 cm<sup>-1</sup> and the band at 131 cm<sup>-1</sup> both logically increase in intensity as the monomeric units diffuse together to form Tl<sub>2</sub>Cl<sub>2</sub>. In addition, another feature at 118 cm<sup>-1</sup> increases on warmup at a faster rate than either of the dimer bands and therefore its growth is attributed to the formation of higher polymers. Results from other diffusion experiments for the low frequency region, although not shown in Figure 8, indicate that the

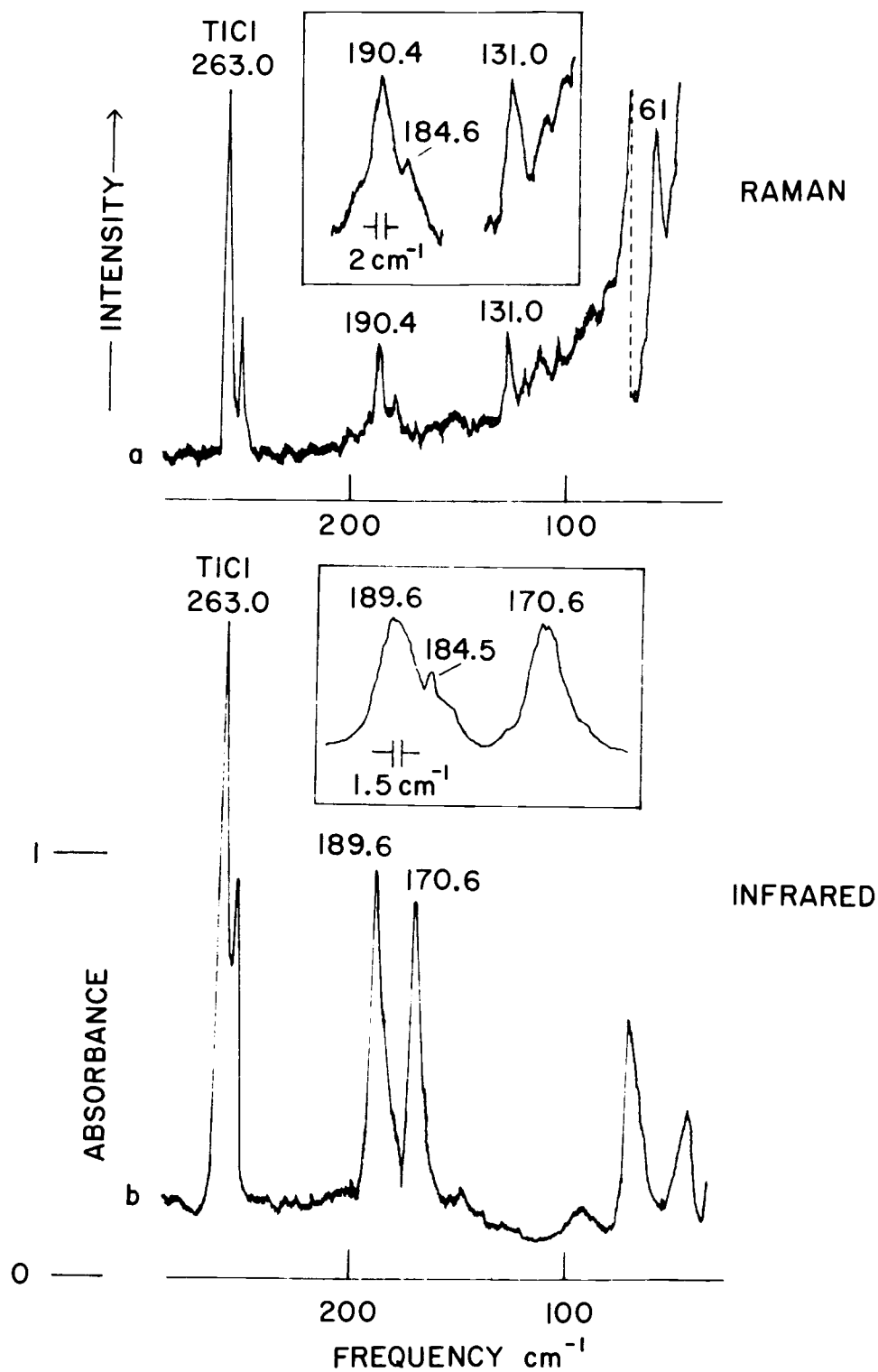


Fig. 7. Vibrational spectra of TlCl/Tl<sub>2</sub>Cl<sub>2</sub> in an argon matrix. Raman a: 5145 Å, 300 cps, SBW = 2 cm<sup>-1</sup>; inset: 5145 Å, 100 cps, SBW = 2 cm<sup>-1</sup>. Infrared b: SBW = 2 cm<sup>-1</sup>, inset: SBW = 1.5 cm<sup>-1</sup>.

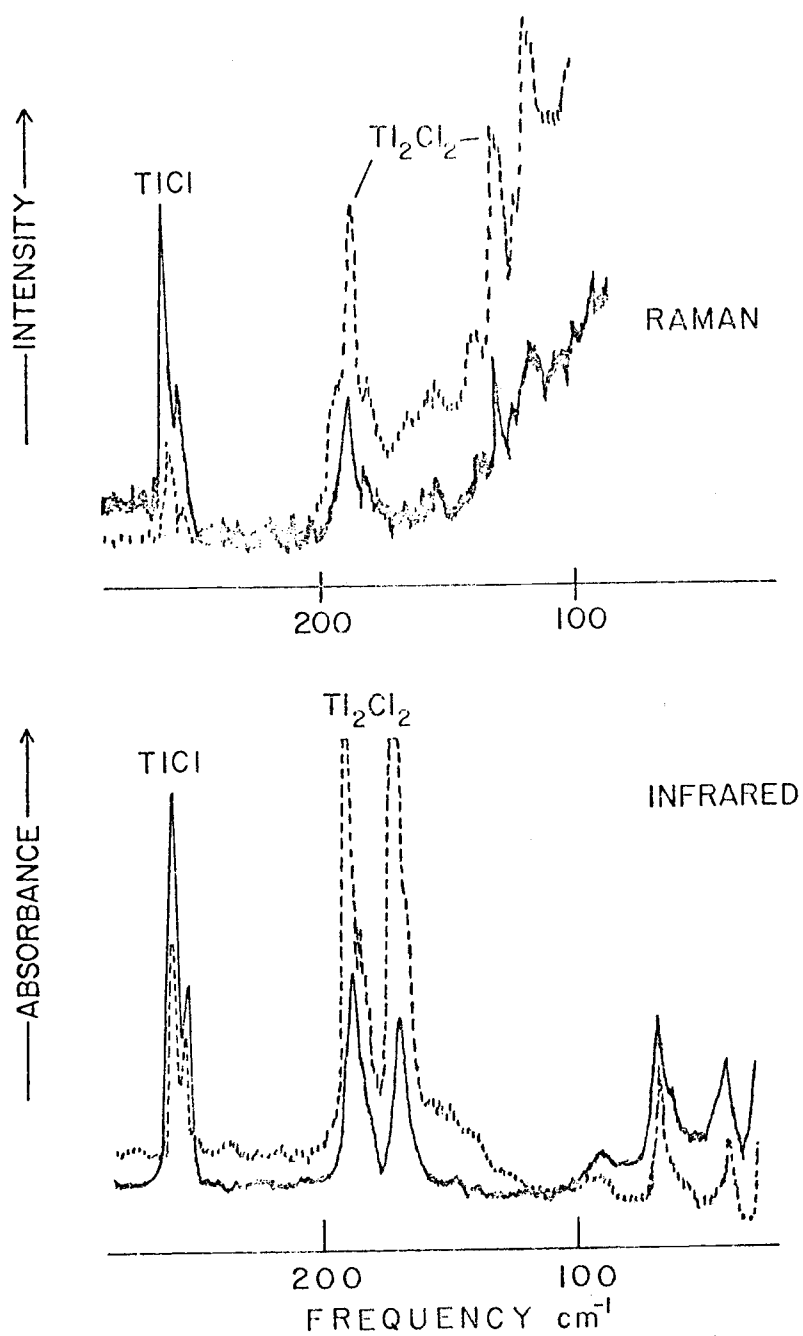


Figure 8. Effect of diffusion on the vibrational spectra of  $\text{TiCl}$ / $\text{Ti}_2\text{Cl}_2$  in an argon matrix; — 14°K, ---- after warmup to 40°K followed by recooling to 14°K.

$61\text{ cm}^{-1}$  band grows in intensity on warmup in a manner qualitatively analogous to the two other dimer features.

A typical infrared spectrum of thallos chloride isolated in an argon matrix is shown in Figure 7. Trace b was recorded after a 1.5 hr deposit at  $M/R = 100-150$  and the inset shows an expanded trace of the two bands at  $189.6$  and  $170.6\text{ cm}^{-1}$ . These infrared results agree well with those reported in ref. 18 and the doublet at  $263\text{ cm}^{-1}$  can be assigned to  $\text{Tl}^{35}\text{Cl}$ ,  $\text{Tl}^{37}\text{Cl}$  while the doublet at  $189.6\text{ cm}^{-1}$  and the band at  $170.6\text{ cm}^{-1}$  are attributed to  $\text{Tl}_2\text{Cl}_2$ . Support for these assignments derives from Figure 8 which shows the resultant changes in the infrared spectrum on warmup to  $40^\circ\text{K}$ . The monomer doublet at  $263\text{ cm}^{-1}$  decreases while the two dimer bands are seen to clearly increase after diffusion has occurred. The only other absorptions apparent in the low frequency region, even in more extended deposits, were the induced phonon modes in the argon matrix at  $71$  and  $46\text{ cm}^{-1}$ .

## Discussion

### Symmetry and Vibrational Assignments

The assignment of the monomer bands at  $443.0\text{ cm}^{-1}$  for  $\text{TlF}$  and  $263.0$  and  $257.1\text{ cm}^{-1}$  for  $\text{TlCl}$  is straightforward. This diatomic stretching mode should have both infrared and Raman activity and, as indicated in ref. 18, the matrix values are close to gas phase values

known from electronic band spectra (473 and 282  $\text{cm}^{-1}$ , respectively). In addition, the observed Cl isotopic splitting agrees well with the calculated value.

For the dimer molecule the two most likely symmetries are linear  $D_{\infty h}$  and planar rhombic  $D_{2h}$ . For  $D_{\infty h}$  one would expect to observe two infrared active modes ( $\Sigma_u^+$ ,  $\Pi_u$ ) and three Raman active modes ( $2\Sigma_g^+$ ,  $\Pi_g$ ). Most importantly, in the Raman spectrum for the  $D_{\infty h}$  model, in addition to a low frequency bending mode, there will be two symmetric stretching modes; one for the Tl-X stretch and a particularly strong band corresponding to the Tl-Tl stretch. The strong Raman intensity of metal-metal stretching vibrations has been noted before (31) and is often used in the characterization of species containing metal-metal bonds. This high Raman intensity is due to the large change in polarizability that occurs when a covalent bond between two atoms of high atomic number is stretched. Indeed, in the case of the Raman spectrum of  $\text{Hg}_2\text{Cl}_2$  (solid) (32), known to have linear  $D_{\infty h}$  symmetry from X-ray structural analysis, the intensity of the Hg-Hg stretch is approximately five times that of the symmetric Hg-Cl stretch. In contrast, the Raman spectra of  $\text{Tl}_2\text{F}_2$  and  $\text{Tl}_2\text{Cl}_2$  displayed in Figures 6 and 7 show no indication of an intense Tl-Tl stretching mode; for both compounds two dimer features of about equal intensity occur above 100  $\text{cm}^{-1}$ . Though these observations admittedly do not completely exclude a linear structure, they are

certainly more consistent with the rhombic  $D_{2h}$  symmetry for both molecules.

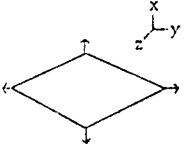
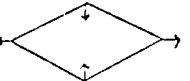
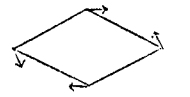
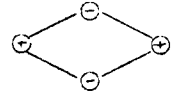
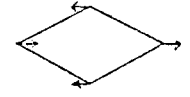
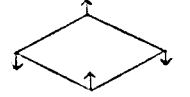
Of course, a rhombic structure implies that there should be three infrared active modes and, indeed, in the infrared spectrum of  $Tl_2F_2$  we observe strong bands at 316 and 257.5  $cm^{-1}$  plus a weaker band at 81  $cm^{-1}$ . It is difficult to be absolutely confident when assigning bands in this low frequency region because of impurity-induced lattice modes. Nonetheless it seems reasonable to assign the 81  $cm^{-1}$  band to  $Tl_2F_2$  on the basis of its parallel behavior with the 316 and 257.5  $cm^{-1}$  features during deposits with different dilution factors and during diffusion experiments. Although this 81  $cm^{-1}$  absorption was not reported in the previous infrared study (18), it is conceivable that it was not resolved from the induced phonon mode cited at 71  $cm^{-1}$ . Since no TlF spectra below 200  $cm^{-1}$  were actually shown in that study, it is difficult to test this conjecture. The fact that no mention was made of the induced phonon mode that we clearly observe at 46  $cm^{-1}$  further suggests that the experimental sensitivity may have been low in this difficult spectral region.

For  $Tl_2Cl_2$ , only two absorptions were observed in the infrared, a doublet at 189.6 and 184.5  $cm^{-1}$  and a singlet at 170.6  $cm^{-1}$ . Therefore, we conclude that the third infrared active mode is too weak to be observed or that it is masked by the bands at 71 or 46  $cm^{-1}$ . The possibility of estimating the frequency of this bending mode will be discussed later.

Finally, probably the most compelling evidence for the  $D_{2h}$  structure comes from the very recent electron diffraction study of Solomonik and coworkers (24). Although high temperature electron diffraction studies have occasionally led to erroneous structural conclusions in the past because of thermal excitation of low lying bending modes (e.g. some of the alkaline earth dihalides), it appears that the results for  $Tl_2F_2$  are reliable. In particular, the  $Tl \cdots Tl$  distance will dominate the radial distribution curve and the observed value,  $3.68 \pm 0.01 \text{ \AA}$ , clearly is much larger than a value of about 2.4 to 2.6  $\text{\AA}$  which has been reasonably suggested for a linear model (18, 19). The  $Tl-F$  distance is reported as  $2.29 \pm 0.02 \text{ \AA}$  and a  $F-Tl-F$  angle of  $73 \pm 2^\circ$  is deduced for a  $D_{2h}$  model.

Accepting then, a rhombic structure for  $Tl_2F_2$  and, by spectral analogy, for  $Tl_2Cl_2$ , we must assign the three infrared active ( $B_{1u}$ ,  $B_{2u}$ ,  $B_{3u}$ ) and three Raman active ( $2A_g$ ,  $B_{1g}$ ) normal vibrations. The axis and numbering convention for describing the vibrations is similar to the one used by Berkowitz in his work on the planar rhombic alkali halide dimers (33). The motions of the atoms for each mode and the corresponding frequency assignments for  $Tl_2F_2$  and  $Tl_2Cl_2$  are given in Table 2. For the infrared active modes, the  $B_{1u}$  out-of-plane bending motion would have the lowest frequency and hence is assigned at  $81 \text{ cm}^{-1}$ . The calculations of Brom and Franzen (18), using an ionic model similar to the one detailed by Berkowitz, indicate

Table 2. Fundamental frequencies of thallos fluoride and chloride in an argon matrix.<sup>a</sup>

Vibrational Number and Symmetry	Approximate Description	Tl <sub>2</sub> F <sub>2</sub> (cm <sup>-1</sup> )	Tl <sub>2</sub> <sup>35,35</sup> Cl <sub>2</sub> (cm <sup>-1</sup> )	Tl <sub>2</sub> <sup>35,37</sup> Cl <sub>2</sub> (cm <sup>-1</sup> )	
		<u>obs</u>	<u>obs</u>	<u>obs</u>	<u>calc</u>
$\nu_1$ (A <sub>g</sub> )		226.0	131.0	(151.0) <sup>b</sup>	129.1
$\nu_2$ (A <sub>g</sub> )		95 85	61	(61)	61.0
$\nu_3$ (B <sub>1g</sub> )		297.0	190.4	(190.4) 184.6	{190.0 185.5
$\nu_4$ (B <sub>1u</sub> )		81	---	---	---
$\nu_5$ (B <sub>2u</sub> )		316.0	189.6	(189.6) 184.5	{190.0 185.5
$\nu_6$ (B <sub>3u</sub> )		257.5	170.6	(170.6)	168.7

<sup>a</sup> All frequencies are believed accurate to 1.0 cm<sup>-1</sup>.

<sup>b</sup> Values in parentheses were not resolved from the stronger 35-35 features.

that the  $B_{2u}$  mode would be higher in frequency than the  $B_{3u}$  mode. In the Raman spectrum, the symmetric in-plane  $A_g$  bending mode (an equivalent designation as a  $Tl \cdots Tl$  stretch could also be used, vide infra) should have the lowest frequency and Berkowitz's calculations further suggest that reasonable approximations for the two remaining frequencies are  $A_g$  (sym. stretch)  $\simeq B_{3u}$  and  $B_{1g}$   $\simeq B_{2u}$ . This implies that the  $B_{1g}$  mode would be higher in frequency than the  $A_g$  (sym. stretch) mode. Efforts were made to confirm this experimentally by Raman depolarization measurements but these were not successful because the matrices were quite scattering.

The question of the frequency choice for the lower  $A_g$  mode still remains since we observed two low frequency Raman bands at 93 and  $85 \text{ cm}^{-1}$ . As noted below, an entropy calculation did not provide a firm basis for choosing between these values. However, it seems reasonable that the extra low frequency feature would be due to higher polymers which should have lower bending frequencies than the dimer and thus we favor the assignment of the  $93 \text{ cm}^{-1}$  band to  $\nu_2$  of  $Tl_2F_2$ .

### Structural Parameters for $Tl_2Cl_2$

For  $Tl_2Cl_2$  electron diffraction results were not available and thus it was necessary to estimate the structural parameters for thermodynamic and force constant calculations. Rather arbitrarily it was assumed that the monomer/dimer  $Tl-X$  bond length ratio would be

the same for both the fluoride and chloride. Combining the  $Tl_2F_2$  value of  $2.29 \text{ \AA}$  with the  $TlF$  and  $TlCl$  monomer bond lengths of  $2.0844$  and  $2.4848 \text{ \AA}$  (from microwave data) (34), we obtain a  $TlCl$  dimer distance of  $2.73 \text{ \AA}$ . Since one other parameter is needed to define the structure completely, two possible approaches were considered.

The first method involves using the  $B_{2u}/B_{3u}$  frequency ratio which is equal to  $\cot(\alpha_{X-Tl-X}/2)$  if the  $B_{2u}$  and  $B_{3u}$  stretching force constants are assumed equal. White et al. (35) found that this relation gave angles in good agreement with electron diffraction values for  $Li_2Cl_2$ ,  $Li_2Br_2$  and  $Li_2I_2$  (calc.  $108^\circ$ ,  $109^\circ$ ,  $113^\circ$ ; obs.  $108^\circ$ ,  $110^\circ$ ,  $116^\circ$ , respectively). For  $Tl_2F_2$ , however, the agreement is somewhat poorer (calc.  $78.4^\circ$ ; obs.  $73^\circ$ ), and moreover, our force constant calculations for  $Tl_2F_2$  indicate that the assumption that  $F_{B_{2u}}/F_{B_{3u}} \approx 1$  is not particularly good (obs. ratio = 1.21, see later). For  $Tl_2Cl_2$ , a  $Cl-Tl-Cl$  angle of  $84^\circ$  is predicted by this relation.

A second basis for estimating the structural parameter would be to assume that the  $X \cdots X$  distance is equal to twice the Pauling ionic radius of the  $X$  atom. The rationale here is that the bonding is principally ionic and the halide ions are pulled into the metal-metal bridge as far as possible. Though perhaps a simplistic view, it is remarkable that this description is quite consistent with observed  $X \cdots X$  distances in  $Li_2Cl_2$ ,  $Li_2Br_2$  and  $Li_2I_2$  as well as in  $Tl_2F_2$  (calc.  $3.62$ ,  $3.90$ ,  $4.32$  and  $2.72 \text{ \AA}$ ; obs.  $3.60$ ,  $3.86$ ,  $4.30$  and  $2.73 \text{ \AA}$ ,

respectively). For  $Tl_2Cl_2$ , a  $Cl \cdots Cl$  distance of  $3.62 \text{ \AA}$  would result, implying a  $Cl-Tl-Cl$  angle of  $83^\circ$ . Since this value is essentially identical to that predicted by method one, a choice between the two is unnecessary. Nonetheless, we prefer the latter description since it has physical appeal and thus we have based all our calculations on a structure with  $Tl-Cl = 2.73 \text{ \AA}$  and  $Cl \cdots Cl = 3.62 \text{ \AA}$ . For this model the  $Tl \cdots Tl$  distance is  $4.09 \text{ \AA}$  versus a value of  $3.68 \text{ \AA}$  in  $Tl_2F_2$ .

### Absolute Entropy Calculations

Assuming a planar rhombic structure for  $Tl_2F_2$  with  $Tl-F = 2.29 \text{ \AA}$  and  $Tl-Tl = 3.68 \text{ \AA}$  we calculate, using expressions given by Herzberg (36), a translational and rotational contribution of 81.3 e. u. to the absolute entropy at  $1000^\circ K$ . Qualitative calculations (18, 19) suggest that the ground electronic state of  $Tl_2F_2$  in the linear configuration is a triplet and hence one would have an electronic contribution of  $R \ln 3 = 2.2$  e. u. to the absolute entropy. However, for the  $D_{2h}$  model, none of the molecular orbitals are degenerate by symmetry and thus it is most likely that the ground state is a singlet. Consequently, there should be no significant electronic contribution to the absolute entropy.

The vibrational contribution if  $\nu_2 = 93 \text{ cm}^{-1}$  is 27.7 e. u. and if  $\nu_2 = 85 \text{ cm}^{-1}$  is 27.9 e. u. The total calculated absolute entropy of  $Tl_2F_2$  at  $1000^\circ K$  would thus be 109.0 or 109.2 e. u., respectively. In

contrast, Brom and Franzen calculated a value of 106.7 e. u. for the linear structure (18). These calculated values can be compared with the experimental value of 110.2 e. u. which was obtained by subtracting the absolute entropy for the reaction  $\text{Tl}_2\text{F}_2(\text{g}) = 2\text{TlF}(\text{g})$  ( $27.9 \pm 0.5$  e. u., ref. 17) from twice the absolute entropy of  $\text{TlF}$  (69.06 e. u., ref. 16). The results can perhaps be said to favor the rhombic structure but the experimental uncertainty is sufficient to preclude any conclusions regarding the choice between  $\nu_2$  frequencies.

For  $\text{Tl}_2\text{Cl}_2$ , the sum of the translational and rotational contributions to the entropy at  $1000^\circ\text{K}$  is 83.1 e. u. and this does not change significantly for large variations in the structural parameters.

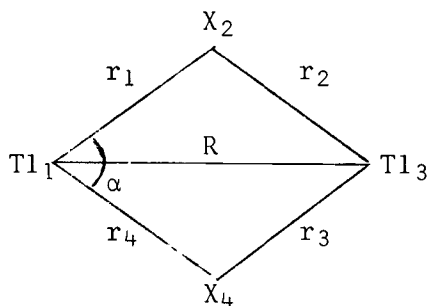
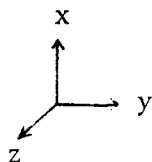
Although the exact frequency of  $\nu_4$  is not known for  $\text{Tl}_2\text{Cl}_2$ , it is likely that it lies below the  $81 \text{ cm}^{-1}$  value for  $\text{Tl}_2\text{F}_2$  and, assuming that it lies in the range  $80\text{-}30 \text{ cm}^{-1}$ , we obtain  $33.0 \pm 1.0$  e. u. for the vibrational entropy contribution. The total calculated value,  $116.1 \pm 1.0$  e. u., does not compare well with Cubicciotti's experimental value (37) of 125.4 e. u. at  $1000^\circ\text{K}$ . Brom and Franzen found an even poorer fit in their comparison using a linear structure for  $\text{Tl}_2\text{Cl}_2$  (calc. value, 112.5 e. u.). However they noted much better agreement if their value calculated for  $1100^\circ\text{K}$  (114.5 e. u.) was compared with a second experimental entropy value of 115.2 e. u. which had been determined by Komshilova and Polachenok (38) at this higher temperature. This latter value is also much closer to our calculated entropy

at  $1100^{\circ}\text{K}$ ,  $118.1 \pm 1.0$  e. u. However the uncertainty in the experimental and calculated values makes it questionable that this comparison can lead to a meaningful distinction between the two structural models. Likewise no reliable value of the unknown bending frequency  $\nu_4$  can be deduced from entropy considerations.

### Force Field Calculations

Symmetry Coordinates and G Matrices. The symmetry coordinates that we have chosen to describe the vibrations of a planar rhombic molecule are given in Table 3. The coordinates  $S_1$ ,  $S_3$ ,  $S_5$  and  $S_6$  are symmetrized combinations of the Tl-X stretches for which the G and F matrices are easily obtained. For the  $B_{1u}$  out-of-plane motion  $S_4$ , the simplest choice is the non-redundant combination of Cartesian displacements in the  $\underline{z}$  direction for which  $G_{44} = 1/2(M_{\text{Tl}}^{-1} + M_{\text{X}}^{-1})$ . A similar  $B_{1u}$  displacement coordinate was used by Berkowitz (33) in his calculations on alkali halide dimers,  $M_2X_2$ . However his calculated G matrix element,  $G_{44} = (M_{\text{X}} - M_{\text{M}})^2 / 8M_{\text{X}}M_{\text{M}}(M_{\text{X}} + M_{\text{M}})$ , differs by more than a mass independent scale factor from the above and appears to be incorrect. Note for example that his expression gives an impossible value of zero if  $M_{\text{M}} = M_{\text{X}}$ . This error is apparently due to an improper coordinate scaling procedure used in deducing the G matrix elements and we note similar problems with G matrix values which he obtains for several other  $M_2X_2$  coordinates.

Table 3. Symmetry Coordinates and Symmetrized F and G Matrix Elements for  $Tl_2X_2$ .



$$\mu_{Tl} = M_{Tl}^{-1}$$

$$\mu_X = M_X^{-1}$$

<u>Symmetry Coordinates</u>	<u>Symmetrized <math>F^\alpha</math> and G Matrix Elements</u>	
$S_1(A_g) = \frac{1}{2}(\Delta r_1 + \Delta r_2 + \Delta r_3 + \Delta r_4)$	$F_{11} = f_r + f_{rr} + f_{rr}' + f_{rr}''$	$G_{11} = \mu_{Tl} + \mu_X + (\mu_{Tl} - \mu_X) \cos \alpha$
$S_2(A_g) = \Delta R$	$F_{22} = f_R, F_{12} = 2f_{rR}$	$G_{22} = 2\mu_{Tl}, G_{12} = 2\mu_{Tl} \cos(\alpha/2)$
$S_3(B_{1g}) = \frac{1}{2}(\Delta r_1 - \Delta r_2 + \Delta r_3 - \Delta r_4)$	$F_{33} = f_r - f_{rr} - f_{rr}' + f_{rr}''$	$G_{33} = \mu_{Tl} + \mu_X - (\mu_{Tl} - \mu_X) \cos \alpha$
$S_4(B_{1u}) = \frac{1}{2}(\Delta z_1 - \Delta z_2 + \Delta z_3 - \Delta z_4)$	$F_{44} = f_{op}$	$G_{44} = \frac{1}{2}(\mu_{Tl} + \mu_X)$
$S_5(B_{2u}) = \frac{1}{2}(\Delta r_1 - \Delta r_2 - \Delta r_3 + \Delta r_4)$	$F_{55} = f_r + f_{rr} - f_{rr}' - f_{rr}''$	$G_{55} = (\mu_{Tl} + \mu_X)(1 + \cos \alpha)$
$S_6(B_{3u}) = \frac{1}{2}(\Delta r_1 + \Delta r_2 - \Delta r_3 - \Delta r_4)$	$F_{66} = f_r - f_{rr} + f_{rr}' - f_{rr}''$	$G_{66} = (\mu_{Tl} + \mu_X)(1 - \cos \alpha)$

$^\alpha f_{rr}$  is an interaction through a common Tl atom,  $f_{rr}'$  an interaction through a common F atom, and  $f_{rr}''$  an interaction between opposite sides of the ring.

There remains one in-plane  $A_g$  coordinate, for which several choices are possible for the  $M_2X_2$  system. Cyvin et al. (39) used a bending coordinate  $S_2 = 1/2(\Delta\alpha_1 + \Delta\alpha_2)$  while Berkowitz (33) chose a combination of  $M\cdots M$  and  $X\cdots X$  stretches  $S_2 = 1/2 (\Delta R_{X\cdots X} - \Delta R_{M\cdots M})$ . Both coordinates require the elimination of one in-plane redundancy condition. An alternative coordinate which does not involve any redundancy is the simple choice  $S_2 = \Delta R_{M\cdots M}$ . We favor this choice since it does not seem likely to us that strong directional valence forces will operate in ionic molecules such as  $Tl_2F_2$  and  $Tl_2Cl_2$  and a non-bonded  $X\cdots X$  or  $Tl\cdots Tl$  coordinate seems more appropriate. Since the X atom is varying in these molecules, the  $Tl\cdots Tl$  distance was selected to examine the change that would result in going from fluorine to chlorine.

Force Constants. Because of the high symmetry, the secular equation for  $Tl_2F_2$  factors into an  $A_g$  block of order two plus four one-dimensional blocks of symmetry  $B_{1g}$ ,  $B_{1u}$ ,  $B_{2u}$  and  $B_{3u}$ . The force constants for the latter blocks are readily obtained and are listed in Table 4. For the  $A_g$  block, three force constants are to be determined but only two frequency constraints are available. A display of possible values for  $F_{11}$  and  $F_{22}$  as a function of assumed values for  $F_{12}$  is offered in Figure 9; any given choice for  $F_{12}$  implies two separate choices for  $F_{11}$  and  $F_{22}$  which will exactly fit the observed frequencies.

Table 4. Force Constants for  $\text{Tl}_2\text{F}_2$  and  $\text{Tl}_2\text{Cl}_2$  (mdyn/Å)Symmetrized Force Constants

$F_{11}$	$1.021 \pm .050^a$	$0.559 \pm .050$
$F_{22}$	$0.804 \pm .0003$	$0.395 \pm .005$
$F_{12}$	$-0.632 \pm .032$	$-0.359 \pm .024$
$F_{33}$	0.728	0.588
$F_{44}$	0.135	---
$F_{55}$	0.956	0.583
$F_{66}$	0.793	0.564

Internal Force Constants

$f_r$	0.875	0.574
$f_{rr}$	0.114	-0.012
$f_{rr}'$	0.032	-0.003
$f_{rr}''$	(0.0)	(0.0)
$f_R$	0.804	0.395
$f_{op}$	0.135	---
$f_{rR}$	-0.632	-0.359

<sup>a</sup> The uncertainties for  $F_{11}$  are estimates from which the uncertainties for  $F_{22}$  and  $F_{12}$  follow from figures 9 and 10.

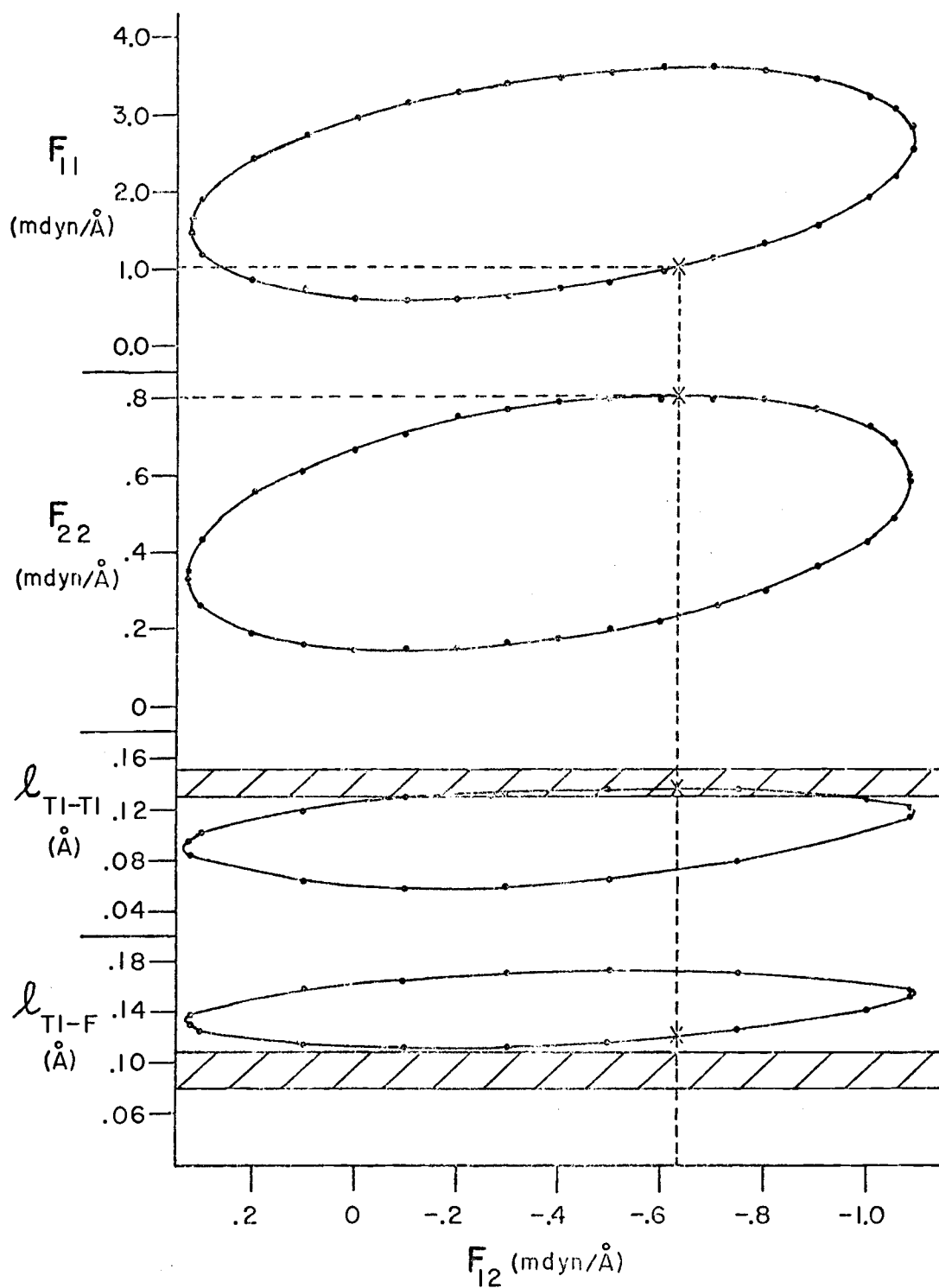


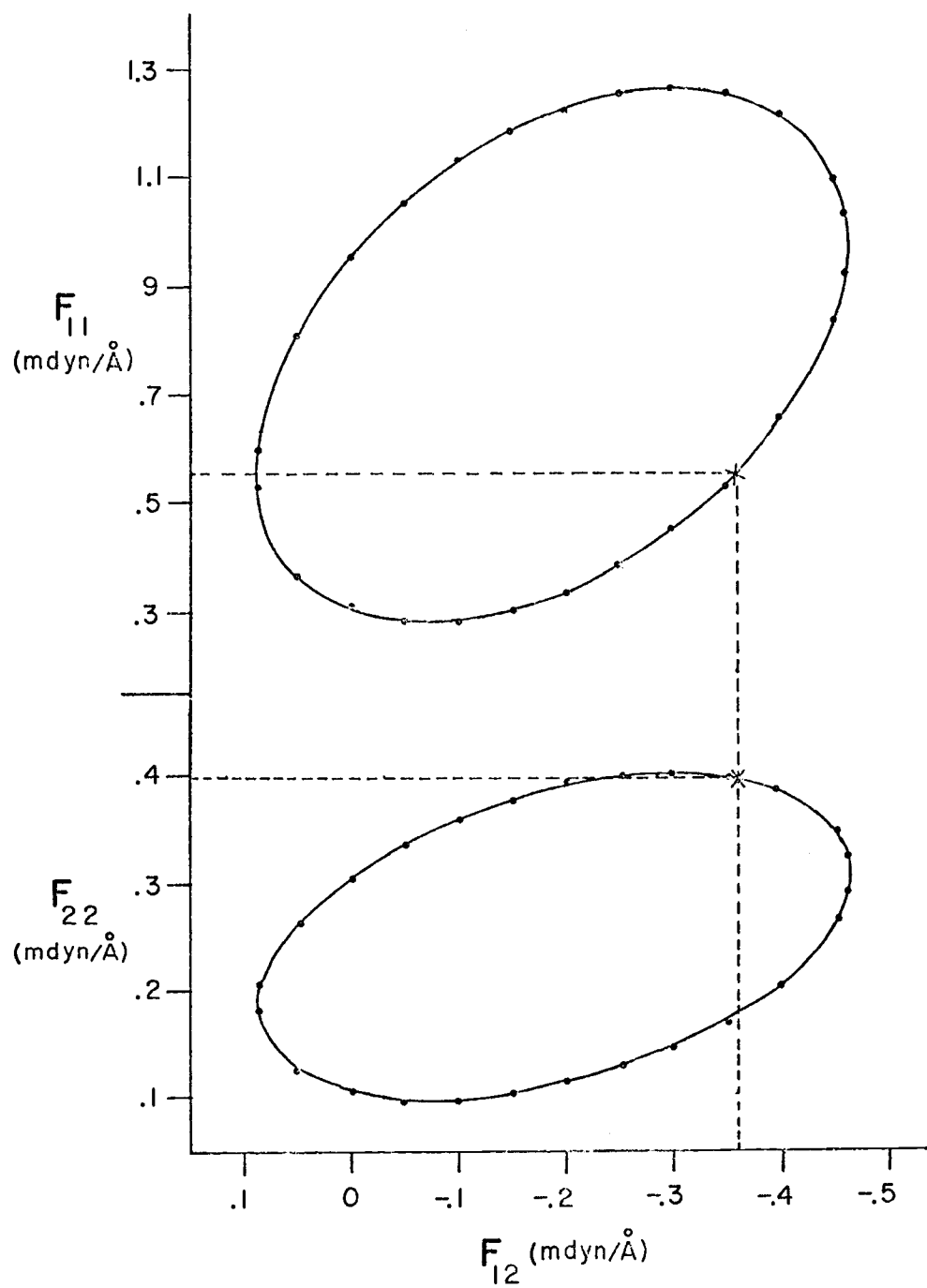
Figure 9. Force fields, calculated amplitudes and experimental (shaded area) mean amplitudes of vibration for  $Tl_2F_2$ .

In an effort to restrict the  $A_g$  force constants further, the mean amplitudes of vibration,  $\ell_{T1-F}$  and  $\ell_{T1 \cdots T1}$ , at  $700^\circ\text{K}$  were calculated and also plotted in Figure 9. The experimental values (24) of these amplitudes,  $\ell_{T1-F} = 0.09_5 \pm 0.01_5 \text{ \AA}$  and  $\ell_{T1 \cdots T1} = 0.14 \pm 0.01 \text{ \AA}$ , at  $700^\circ\text{K}$  are shown as shaded bands. Unfortunately there is reasonable agreement between the calculated and observed T1-F amplitudes for a wide range of  $F_{12}$  so that this amplitude does not serve as a particularly useful constraint. The same is true of the T1  $\cdots$  T1 amplitude for which no actual intersection between calculated and observed values results.

An alternative choice in defining the force field would be to simplify it on some reasonable basis. One sensible approach might be to set the stretch-stretch interaction constant  $f''_{rr}$  to zero since it involves bonds on opposite sides of the ring and these have no common atoms. With this assumption, values of  $f_r = 0.875$ ,  $f_{rr} = 0.114$  and  $f'_{rr} = 0.0324$  mdyn/ $\text{\AA}$  result from the  $B_{1g}$ ,  $B_{2u}$  and  $B_{3u}$  symmetrized force constants. A value of  $F_{11} = f_r + f_{rr} + f'_{rr} + f''_{rr} = 1.021$  mdyn/ $\text{\AA}$  can then be calculated and this implies values of  $F_{12} = 0.264$  or  $-0.632$  mdyn/ $\text{\AA}$  (dashed lines, Figure 9). The first solution point must be discarded because of the poor agreement with the observed mean square amplitudes but the second value is quite acceptable. This value of  $F_{12}$  in turn implies a value of  $F_{22} = 0.804$  mdyn/ $\text{\AA}$ . To obtain an estimate of the uncertainty in these three force constants we have assumed that the magnitude of  $f''_{rr}$  is unlikely to be larger

than  $f'_{rr} = 0.032 \text{ m dyn}/\text{\AA}$ . Thus a generous value of  $\pm 0.05 \text{ m dyn}/\text{\AA}$  for the uncertainty in  $F_{11}$  was arbitrarily chosen and the implied uncertainties in  $F_{12}$  and  $F_{22}$  are listed in Table 4.

For  $\text{Tl}_2\text{Cl}_2$ ,  $f''_{rr}$  was also assumed equal to zero and the solution points are shown in Figure 10 and are tabulated in Table 4. By analogy with the  $\text{Tl}_2\text{F}_2$  results, the  $F_{12}$  intersection point of  $-0.403 \text{ m dyn}/\text{\AA}$  was chosen over the other possibility near  $+0.1$ . As a check on the validity of the  $\text{Tl}_2\text{Cl}_2$  force field, frequencies were calculated for the isotopic molecule  $\text{Tl}_2^{35,37}\text{Cl}_2$  with the results shown in the last column of Table 2. For this reduced  $C_{2v}$  symmetry, all modes become simultaneously infrared and Raman active and mixing occurs between the  $B_{1g}$  and  $B_{2u}$  modes and also between the  $A_g$  and  $B_{3u}$  vibrations. For  $\nu_1$ ,  $\nu_2$ ,  $\nu_4$  and  $\nu_6$  the calculated frequencies are only very slightly shifted from those of the parent  $\text{Tl}_2^{35,35}\text{Cl}_2$  molecule and no frequency splittings were experimentally resolved. For the  $B_{1g}$  and  $B_{2u}$  modes the situation was different however. These vibrations occur at nearly the same frequency ( $190 \text{ cm}^{-1}$ ) in the parent isotope (a feature we believe to be due to accidental degeneracy rather than a breakdown of the mutual exclusion rule because of a loss of inversion symmetry). On isotopic substitution these vibrations can mix and the normal coordinates for the mixed isotopic species show that the two coordinates are essentially  $S_3 \pm S_5$ . These plus-minus combinations can be described as antisymmetric stretches of either



the  $\text{Tl-}^{35}\text{Cl-Tl}$  or the  $\text{Tl-}^{37}\text{Cl-Tl}$  bridges and both are Raman and infrared allowed. The calculated frequencies are 190.0 and 185.5  $\text{cm}^{-1}$  respectively and it is apparent that the 190.0  $\text{cm}^{-1}$  component cannot be resolved from the parent  $B_{1g}$  and  $B_{2u}$  features. The 185.5  $\text{cm}^{-1}$  band is observed however, in the infrared at 184.5  $\text{cm}^{-1}$  and in the Raman at 184.6  $\text{cm}^{-1}$ . Moreover the experimental 190/185 intensity ratios in the infrared and Raman spectra (Figure 7) are in good accord with that predicted from the mixing process (without mixing the observed ratios would be 9:6; with mixing the ratio would be 9+3:6-3). Thus both the frequencies and intensities for the  $\text{Tl}_2^{35,37}\text{Cl}_2$  species are satisfactorily reproduced by the force constants listed in Table 4 and we believe them to be reliable.

Several observations regarding the numerical values for the force constants can be made. First it may be noted that the Tl-X bond stretching constants for  $\text{Tl}_2\text{F}_2$  (0.875  $\text{mdyn}/\text{\AA}$ ) and  $\text{Tl}_2\text{Cl}_2$  (0.574  $\text{mdyn}/\text{\AA}$ ) both decrease by a factor of about 2.5 compared to the values calculated for the monomer from gas phase frequencies (Tl-F, 2.29  $\text{mdyn}/\text{\AA}$ ; Tl-Cl, 1.40  $\text{mdyn}/\text{\AA}$ ). This large decrease is of course reasonable since the Tl-X bond lengths greatly increase as each halogen atom bonds to two Tl atoms in forming the dimer. The stretch-stretch interaction constants are noticeably larger in  $\text{Tl}_2\text{F}_2$  than in  $\text{Tl}_2\text{Cl}_2$ ; the latter seems to involve little coupling among the Tl-Cl stretches. For both compounds the coupling is larger through

the halogen  $f_{rr} > f'_{rr}$ ). The Tl...Tl force constant drops significantly in going from the fluoride (0.804 m dyn/Å) to the chloride (0.395 m dyn/Å) and both are much lower than the value calculated for the Tl<sub>2</sub> diatomic molecule ( $\nu = 136 \text{ cm}^{-1}$ ,  $f_R = 1.12 \text{ m dyn/Å}$ ) (40). As might be anticipated, the interaction between the Tl...Tl stretch and the Tl-X stretch is substantial; indeed the interaction constant  $f_{rR}$  is comparable to  $f_R$  for both compounds. Moreover the normal coordinate and the potential energy distribution for the  $\nu_2 A_g$  frequency also indicate heavy mixing among  $S_1$  and  $S_2$ . Possibly the use of a bending coordinate for  $S_2$  might reduce this mixing and hence be more descriptive of the normal coordinates. This was not done in our calculations because the accompanying redundancy conditions add bending terms to the  $B_{2u}$  and/or  $B_{3u}$  symmetry force constants and the assumption that  $f''_{rr} = 0$  is no longer sufficient to define the force field.

Finally, it is interesting to note that, if the out-of-plane force constant is assumed the same for Tl<sub>2</sub>F<sub>2</sub> and Tl<sub>2</sub>Cl<sub>2</sub>, a  $\nu_4$  frequency of  $62 \text{ cm}^{-1}$  would be predicted. This could be viewed as an upper bound for this mode since it is likely that this force constant will drop 30-50% in going to the chloride as do all of the other force constants (Table IV). A drop of 50% would put this mode at  $31 \text{ cm}^{-1}$ , below the limit of our spectrometer, while a drop of 25% would place the band at  $46 \text{ cm}^{-1}$ , in coincidence with the induced lattice phonon mode. Thus

either possibility could account for our failure to detect this fundamental.

### Amplitudes of Vibration for $Tl_2F_2$

Although the calculation of amplitudes of vibration for  $Tl_2F_2$  did not prove effective in constraining the force field, the results are relevant to several experimental observations. First, it may be noted that the calculated and observed Tl-F amplitude ( $0.095 \text{ \AA}$ ) is noticeably larger than that which we calculate for Tl-F monomer ( $0.067 \text{ \AA}$ ). This is of course to be expected since the bonds are much weaker in the dimer. Next it is interesting that a large out-of-plane bending amplitude ( $31^\circ$ ) was calculated for the angle between the two Tl-F-Tl flaps at  $700^\circ\text{K}$ . This value is in good agreement with a flap angle of  $35^\circ$  which we deduce from the electron diffraction results in the following way. The experimental value of the F...F distance is reported (24) as  $2.605 \pm 0.124 \text{ \AA}$  whereas the value deduced for a planar molecule from the experimental Tl-F ( $2.29 \text{ \AA}$ ) and Tl...Tl ( $3.68 \text{ \AA}$ ) distances is  $2.73 \text{ \AA}$ . This difference, attributed to the "shrinkage effect," implies that the bending amplitude is large and averages about  $35^\circ$ .

Such a large bending amplitude offers a possible explanation for the electron scattering results of Fickes et al. (20). As noted earlier these experiments suggested very large instantaneous dipole moments

in  $\text{Tl}_2\text{F}_2$ , in the range of 2.5 to 7.7 Debye depending on the electron energy. The electron- $\text{Tl}_2\text{F}_2$  interaction time is apparently so short in these experiments that the electrons sample frozen nuclear configurations. Fickes et al. comment that a  $\Pi_u$  bending amplitude of  $30^\circ$  would be needed for a linear model in order to account for these observations. However, the  $256 \text{ cm}^{-1}$  value assigned to this mode by Brom and Franzen only yields a mean amplitude of  $2.0^\circ$  for the F-Tl-Tl angle. In the limit of unit charge on each atom, such a displacement would produce a dipole of 0.8 Debye, much lower than the observed values. However, for a planar rhombic structure with a mean bending amplitude of  $31^\circ$ , the unit charge model gives a dipole moment of 3.7 Debye--a value in good accord with the electron scattering data. This argument can also be taken as support for the idea of largely ionic bonding in the thallos halide dimers.

### Summary

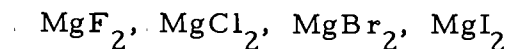
Infrared and Raman spectra have been obtained for matrix isolated  $\text{Tl}_2\text{F}_2$  in an effort to resolve conflicting statements regarding the structure and bonding in this simple dimer. On the basis of Raman intensities and the number of infrared active fundamentals, it is concluded that the molecule is planar rhombic rather than linear. Raman results for  $\text{Tl}_2\text{Cl}_2$  suggest that this dimer also has the  $D_{2h}$  configuration.

These conclusions are compatible with a very recent electron diffraction study on  $\text{Tl}_2\text{F}_2$  but differ from those reached from a previous infrared matrix study, absolute entropy calculations and a photoelectron investigation. The present infrared results and entropy calculations based on both infrared and Raman frequencies are shown to be generally more consistent with the rhombic model than the linear one. The question of the interpretation of the photoelectron spectrum remains. The argument for a linear structure in this case is based on a comparison of the observed photoelectron spectrum with energy level differences calculated for linear and rhombic  $\text{Tl}_2\text{F}_2$ . These semiempirical calculations are based on a number of approximations (e.g. minimal basis set, neglect of core levels, use of Koopman's theorem, etc.) and, as pointed out by Dehmer et al., they are not quantitative but serve only to reinforce the earlier conclusions based on entropy or infrared arguments. Since the latter arguments are no longer compelling, perhaps all that need be said is that a higher order of calculations appears to be necessary for the thallos halides.

Force constants have been deduced for both  $\text{Tl}_2\text{F}_2$  and  $\text{Tl}_2\text{Cl}_2$  and the observed frequencies are reproduced quite accurately. For  $\text{Tl}_2\text{F}_2$  vibration amplitudes were calculated but comparison with the observed Tl-F and Tl...Tl amplitudes showed the latter to be poor force field constraints. A large out-of-plane bending amplitude ( $31^\circ$ ) was calculated and this is in good accord with the electron diffraction

results. A calculation of the dipole moment associated with this large amplitude, assuming an ionic model for  $\text{Tl}_2\text{F}_2$ , gives a large value (3.7 Debye) in excellent agreement with the range of values deduced from an electron scattering experiment on  $\text{Tl}_2\text{F}_2$  molecular beams.

### III. INFRARED AND RAMAN SPECTRA AND STRUCTURE OF MATRIX ISOLATED MAGNESIUM DIHALIDES:



#### Introduction

The structures and chemical bonding of the alkaline earth dihalides have been the subjects of a wide variety of experimental and theoretical investigations in recent years. Although early electron diffraction results suggested linear configurations for all the dihalides examined (41), the uncertainty in the X-M-X angle was quite large (typically  $30^\circ$ ) due to thermal excitation of the low frequency bending mode. A more critical test of linearity in the vapor phase came from subsequent electronic deflection experiments by Klemperer and coworkers (42, 43) in which, of the alkaline earth dihalides, only  $\text{CaF}_2$ ,  $\text{SrF}_2$ ,  $\text{SrCl}_2$  and the barium dihalides were found to be polar and hence bent. Infrared matrix isolation studies have been used to confirm most of these conclusions and bond angles have been estimated for the difluorides and dichlorides from isotopic frequency shifts in the antisymmetric stretch ( $\nu_3$ ). In the case of  $\text{MgF}_2$ , however, some controversy has developed regarding the linearity of this molecule in a matrix and it was, in part, this aspect which prompted the combined infrared and Raman work reported here for the magnesium dihalides.

The infrared spectrum of matrix isolated  $\text{MgF}_2$  has been studied by Snelson (46) (S), Mann et al. (44) (M), and Hauge, Margrave and Kana'an (47) (HMK). While S and HMK conclude that the molecule is linear, the  $\nu_3$  isotopic frequency shifts measured by M have been used to deduce a bent structure with an apex angle of  $158^\circ$  (45). In support of this conclusion, these workers cite a band at  $478 \text{ cm}^{-1}$  which they suggest is due to the symmetric stretch ( $\nu_1$ ), infrared active only for a bent configuration. S and HMK attribute this absorption to dimeric  $\text{MgF}_2$  and the work of H further suggests that  $\nu_1 = 552 \text{ cm}^{-1}$  in argon on the basis of unpublished work in which  $\text{MgF}_2$  was complexed with other molecules, thereby causing some infrared activity.

There have been a number of studies on the bonding and geometry of  $\text{MgF}_2$  from a theoretical standpoint. Hayes (48) proposed a simple explanation of the geometry of the group IIa dihalides which uses Walsh-type diagrams, modified to account for the influence of the metal atom d orbitals. His results predict a linear structure for all of the magnesium dihalides. Allavena and Besnainou (49) have predicted: a)  $C_{2v}$  symmetry for  $\text{MgF}_2$  using semi-empirical CNDO-type calculations and b)  $D_{\infty h}$  symmetry using a priori SCF-MO calculations. Two additional independent theoretical studies (50, 51) have predicted a linear structure with a small barrier to deformation. Hayes et al. (52) further suggest that the dipole induced-dipole

interaction between  $\text{MgF}_2$  and a krypton matrix could be sufficient to distort  $\text{MgF}_2$  from a linear gas phase configuration. Recently, Kim and Gordon (53) have calculated vibrational frequencies for  $\text{MgF}_2$  ( $\nu_1 = 630$ ,  $\nu_2 = 330$ ,  $\nu_3 = 990 \text{ cm}^{-1}$ ) from calculated ion-ion interaction potentials assuming a linear structure.

Buchler and Klemperer (54) observed the gas phase infrared spectrum of  $\text{MgCl}_2$  and assigned  $\nu_3$  at  $597 \text{ cm}^{-1}$  and the bend,  $\nu_2$ , at  $295 \text{ cm}^{-1}$ . Cocke et al. (55) investigated the infrared spectrum of the argon matrix isolated molecule and reported bands at 603 and  $585 \text{ cm}^{-1}$ , attributable to  $\nu_3$  of  $\text{MgCl}_2$  in different matrix sites. They suggest that the lower frequency band could arise from a  $\text{MgCl}_2$  molecule that is bent due to possible distortions from the matrix environment. White et al. (56) have also observed the infrared spectrum of  $\text{MgCl}_2$  isolated in a krypton matrix, and assign bands in the  $590$  to  $570 \text{ cm}^{-1}$  region to  $\nu_3$  of  $\text{MgCl}_2$  in two different matrix sites. In addition they observe a low frequency absorption at  $88 \text{ cm}^{-1}$  which was assigned as the bend. From selection rule considerations and measured isotopic shifts, these workers conclude that  $\text{MgCl}_2$  is linear in the matrix environment as well as in the vapor phase.

Although  $\text{MgBr}_2$  and  $\text{MgI}_2$  are believed to be linear in the vapor phase, the infrared results are sparse and inconclusive in this regard. Randall et al. (57) have examined the gas phase infrared spectrum of  $\text{MgBr}_2$  and report a band at  $490 \text{ cm}^{-1}$  attributable to  $\nu_3$ . In an argon

matrix, Cocke et al. (55) observed this feature as a multiplet at 520, 509 and 502  $\text{cm}^{-1}$ . Neither study allowed examination of the low frequency bending region below 200  $\text{cm}^{-1}$ . For  $\text{MgI}_2$ , no vibrational spectrum has been reported to date.

In the present study, complete vibrational spectra of all the magnesium dihalides have been obtained. From the Raman results, the symmetric stretch has been clearly identified for each compound and the corresponding infrared region has been carefully examined for an infrared counterpart which might imply a nonlinear structure. Several interesting complications arise which have structural implications and these are discussed. Finally, a complete force constant analysis as well as a calculation of the statistical thermodynamic functions is offered.

### Experimental

The experimental apparatus used in this study has been described in Chapters I and II and only the details pertinent to these experiments will be given here. The samples of  $\text{MgF}_2$  (optical grade, Optovac; 99.9%, Cerac),  $\text{MgCl}_2$  (99.99%, Rocky Mountain Research),  $\text{MgBr}_2$  (99%, Cerac) and  $\text{MgI}_2$  (99%, Cerac) were vaporized in resistively heated single-oven Knudsen cells constructed of graphite, Ta or Pt. The platinum cells were made by rolling 0.005 in. foil into a tube, spot welding the seam, and crimping the ends after filling.

Typical effusion temperatures were:  $\text{MgF}_2$ ,  $1225^\circ\text{C}$ ;  $\text{MgCl}_2$ ,  $800^\circ\text{C}$ ;  $\text{MgBr}_2$ ,  $750^\circ\text{C}$ ;  $\text{MgI}_2$ ,  $700^\circ\text{C}$ .

Prior to a typical experiment, the cold cell and furnace were evacuated to a pressure of approximately  $1 \times 10^{-5}$  torr and the sample was outgassed in the Knudsen cell under vacuum to slightly above the anticipated deposition temperature. The deposition rates were adjusted to optimize the monomer:dimer ratio in the matrix. The matrix gas was generally deposited at a rate of 5 to 15 mM/hr (as measured by a calibrated flowmeter), and deposition times were of the order of 2-6 hr. In some experiments, the deposition rate of the effusing species was measured by an oscillating quartz crystal microbalance (as described in Chapter II) which can be moved to directly sample the molecular beam during the course of the experiment. After a short time, the crystal is withdrawn from the beam and the measured change in frequency with time can be related to the deposition rate of the sample. For example, typical changes in the frequency of a 9 MHz crystal were of the order of 0.3 to 0.5 KHz/min, corresponding to deposition rates of  $\text{MgF}_2$  of  $5.0 \times 10^{-3}$  to  $1.0 \times 10^{-2}$  mM/hr. The matrix gas flow was adjusted to allow the M/R (mole ratio of matrix gas to metal halide) to be varied for these deposition rates.

## Results

### MgF<sub>2</sub> in Krypton

The infrared and Raman spectra of MgF<sub>2</sub> generated in a graphite Knudsen cell and isolated in a krypton matrix are presented in Fig. 11 and a summary of the observed spectral features is given in Table 5. In the Raman spectrum, trace a was recorded with 5145 Å excitation for a  $\approx 1225^\circ\text{C}$  deposit in which  $M/R \approx 1000$  while trace b was obtained with 4880 Å excitation in a second experiment with similar deposition conditions. Trace c was observed using 5145 Å with an increased deposit rate ( $\approx 1275^\circ\text{C}$ ) so that  $M/R \approx 500$ ; no other bands in the region 350 to 200  $\text{cm}^{-1}$  were observed in this spectrum. In all, 26 experiments were conducted for MgF<sub>2</sub>, supplied from two different sources, in matrices of Ar, Kr and N<sub>2</sub> and using graphite, Ta and Pt Knudsen cells. Raman spectra were recorded for 12 of these and the feature at 544.5  $\text{cm}^{-1}$  in Kr (550.0  $\text{cm}^{-1}$  in Ar, 514  $\text{cm}^{-1}$  in N<sub>2</sub>) was consistently present irrespective of the frequency of the exciting radiation. From mass spectroscopic investigations it is known that the composition of the vapor over the solid at the effusion temperatures used is  $\approx 99\%$  MgF<sub>2</sub> (58), thus the dominant species in the matrix should be MgF<sub>2</sub>. Since the scattering produced by the symmetric stretching mode of MgF<sub>2</sub> should dominate the Raman spectrum, there seems no doubt that the band at 544.5  $\text{cm}^{-1}$  must be

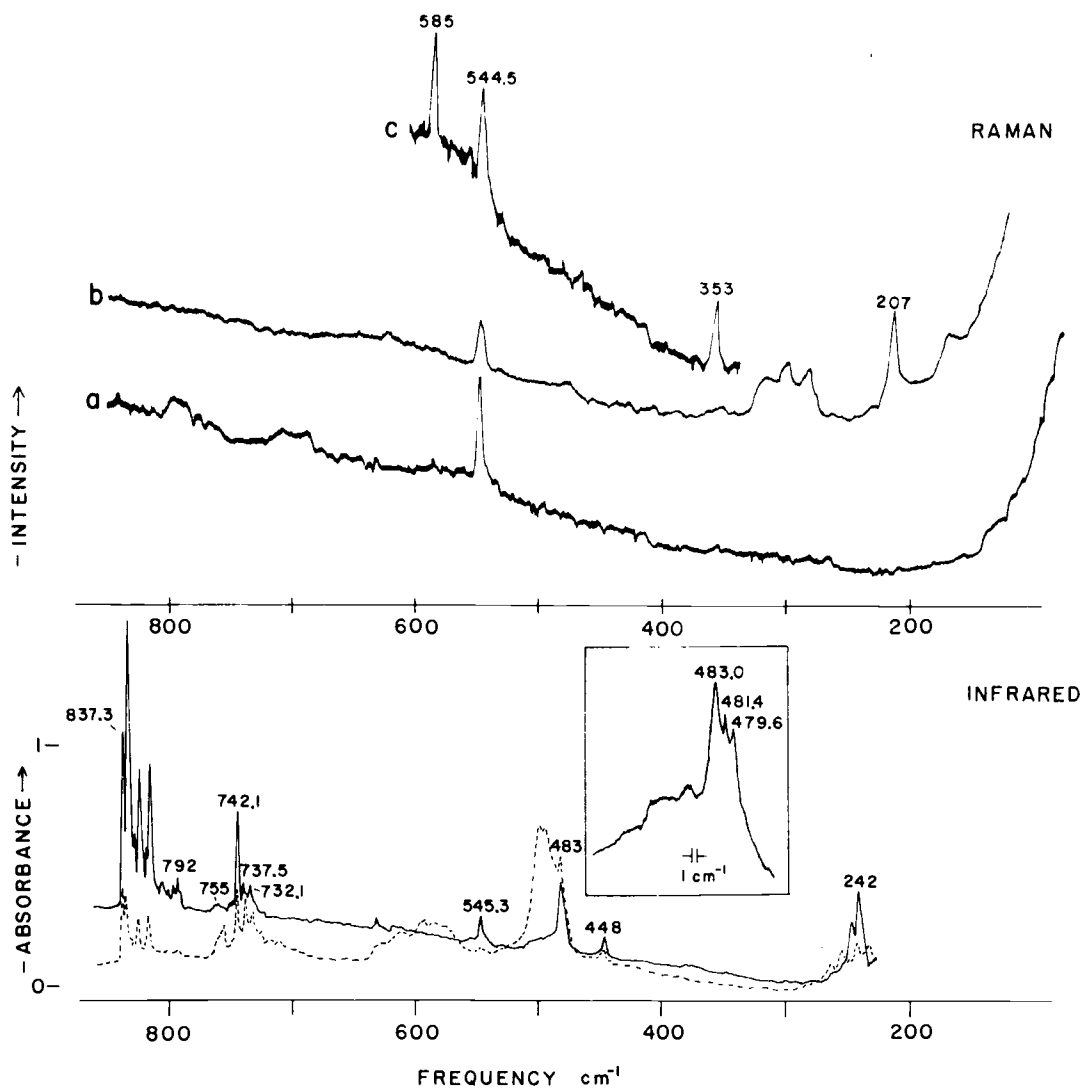


Fig. 11. Vibrational spectra of  $\text{MgF}_2$  in a krypton matrix. Raman a:  $M/R \approx 1000$  ( $T = 1225^\circ\text{C}$ ),  $5145 \text{ \AA}$ ,  $2000 \text{ cps}$ ,  $\text{SBW} = 4 \text{ cm}^{-1}$ ; b:  $T = 1225^\circ\text{C}$ ,  $4880 \text{ \AA}$ ,  $1000 \text{ cps}$ ,  $\text{SBW} = 5 \text{ cm}^{-1}$ ; c:  $M/R \approx 500$  ( $T = 1275^\circ\text{C}$ ),  $5145 \text{ \AA}$ ,  $500 \text{ cps}$ ,  $\text{SBW} = 3 \text{ cm}^{-1}$ . Infrared:  $T = 1225^\circ\text{C}$ ,  $\text{SBW} = 2 \text{ cm}^{-1}$ , —  $14^\circ\text{K}$ , --- after annealing at  $35 - 40^\circ\text{K}$  followed by recooling to  $14^\circ\text{K}$ .

Table 5. Summary of observed spectral features for  $\text{MgF}_2$  isolated in various matrices.

	<u>Krypton</u>	<u>Argon</u>	<u>Nitrogen</u>	<u>Assignment</u>
RAMAN: ( $\text{cm}^{-1}$ )			2360	$14,14\nu_{\text{N}_2} + \nu_{\text{N}_2}$ lattice
			2344	$\text{MgF}_2 \cdots \text{N}_2$
			2326	$14,14\nu_{\text{N}_2}$
			2290	$14,15\nu_{\text{N}_2}$
	585	584		$(\text{MgF}_2)_2$
	544.5	550.0	514	$\nu_1 \text{MgF}_2$
	353	354		$(\text{MgF}_2)_2$
	207	186	230	See discussion
INFRARED: ( $\text{cm}^{-1}$ )	840-810	845-815	780-760	$\nu_3 \text{MgF}_2$
	791.5	795	755.3	$\text{MgF}_2 \cdots \text{X} ?$
	755	758		$(\text{MgF}_2)_n$
	745-725	750-730	699	$(\text{MgF}_2)_2$
	545.3	548.0		See discussion
	483	486.5	472	$(\text{MgF}_2)_2$
	447.6	450	432	$(\text{MgF}_2)_2$
	242	249	219	$\nu_2 \text{MgF}_2$
	$\approx 240$	$\approx 240$		$(\text{MgF}_2)_2$

assigned as  $\nu_1$  of  $\text{MgF}_2$ . However, in addition to  $\nu_1$ , occasionally there were complicating features present in the Raman spectrum. For example, a structured band near  $300 \text{ cm}^{-1}$  appeared only with  $4880 \text{ \AA}$  excitation and thus is attributed to an unknown fluorescent species. The lines at  $585$  and  $353 \text{ cm}^{-1}$  (Fig. 11, c) were favored in more concentrated matrices and can be assigned to dimers of  $\text{MgF}_2$ . In addition, a Raman band at  $207 \text{ cm}^{-1}$  was observed with varying intensity in several experiments and on occasion its intensity was actually greater than that of  $\nu_1$ . Several observations can be made regarding this  $207 \text{ cm}^{-1}$  feature: 1) it did not depend upon the  $\text{MgF}_2$  source (Optovac or Cerac) or the Knudsen cell material (graphite or Ta), 2) its intensity did not correlate with either the monomer or dimer features, 3) it is probably not due to a product of a reaction with the furnace materials (i. e., electrodes or radiation shields) since the band did not appear in all of the experiments, 4) it is not due to higher aggregates or solid  $\text{MgF}_2$  because of the measured dilution factors. Although no positive identification of the source for this absorption was made in the study, several possible candidates will be discussed later.

Figure 11 also shows an infrared scan of  $\text{MgF}_2$  in a krypton matrix after a 2-hr deposit at  $\sim 1250^\circ \text{C}$ . The solid trace was recorded at  $14^\circ \text{K}$  while the dashed trace shows the resulting changes in the spectrum after allowing diffusion to occur at  $35\text{-}40^\circ \text{K}$ . The multiplet

above  $800\text{ cm}^{-1}$  is attributed to  $\nu_3$  of  $\text{MgF}_2$  in agreement with S, M and HMK, and more details concerning its structure will be given below. The weak absorption at  $791.5\text{ cm}^{-1}$  disappears rapidly on diffusion and is possibly due to a mobile impurity or  $\text{MgF}_2$  complex. The multiplet near  $740\text{ cm}^{-1}$  has been assigned to diatomic  $\text{MgF}$  by M and to  $\text{MgF}_2$  dimer by S and HMK. We favor the latter since, in agreement with HMK, we observed that the intensity of both the  $740\text{ cm}^{-1}$  multiplet and the  $483\text{ cm}^{-1}$  feature increased relative to  $\nu_3$  for more concentrated matrices and after diffusion (Fig. 11). A weak shoulder at  $755\text{ cm}^{-1}$  also increased on diffusion and in fact at a greater rate than the  $740\text{ cm}^{-1}$  multiplet; consequently, it is attributed to polymeric  $\text{MgF}_2$ . A broad feature near  $500\text{ cm}^{-1}$  behaved similarly and hence is also assigned to higher polymers.

The feature near  $483\text{ cm}^{-1}$  showed some isotopic components (inset, Fig. 11) which have been reported at higher resolution by M at  $478.0$ ,  $477.3$  and  $476.8\text{ cm}^{-1}$ . These workers assign this isotopic multiplet to  $\nu_1$  of  $\text{MgF}_2$  and cite its observation and the Mg isotopic shifts as evidence for a bent structure for  $\text{MgF}_2$ . HMK also has observed these bands, at  $484.9$ ,  $482.7$  and  $481.1\text{ cm}^{-1}$ , but attributes them to  $\text{MgF}_2$  dimer. Our infrared diffusion results support the latter conclusion and, even more importantly, the Raman results conclusively establish  $\nu_1$  at  $544.5\text{ cm}^{-1}$ . No significant Raman feature was observed at  $478\text{ cm}^{-1}$  despite careful examination.

The strong feature at  $242\text{ cm}^{-1}$  is assigned to the  $\nu_2$  bending mode, in agreement with earlier studies by S and M. Some dimer/polymer absorptions also contribute in this region as shown by the diffusion trace in Fig. 11. M has noted an underlying dimer band at  $240\text{ cm}^{-1}$  and our dilution studies are in accord with this since the  $242$  peak is enhanced with respect to  $\nu_3$  in more concentrated matrices.

It is interesting to examine more closely the  $\nu_3$  and  $\nu_1$  regions in the infrared as shown in Fig. 12. The solid trace was obtained at  $14^\circ\text{K}$  while the dashed trace shows the results after diffusion at  $35\text{-}40^\circ\text{K}$  with appropriate scale amplification factors included in the figure. The features in the  $\nu_3$  region can be assigned to the three magnesium isotopes ( $^{24}\text{Mg} = 79\%$ ,  $^{25}\text{Mg} = 10\%$ ,  $^{26}\text{Mg} = 11\%$ ) in three different matrix sites. The measured frequencies and intensities are generally in excellent agreement with the work of HMK and M, and it is apparent from the diffusion results that the  $833.0\text{ cm}^{-1}$  site is thermally unstable. However, the intensities for two absorptions at  $823.9$  and  $815.0\text{ cm}^{-1}$  are not consistent with what is expected for the  $^{25}\text{MgF}_2$  and  $^{26}\text{MgF}_2$  species, and these bands were not present in all experiments. Their intensity did not parallel that of either the monomer or dimer bands and an explanation which we favor would attribute them to weak  $\text{MgF}_2$  complexes such as have been observed by HMK. The complexing agents might be  $\text{H}_2\text{O}$ ,  $\text{N}_2$ ,  $\text{O}_2$ ,  $\text{CO}$ ,  $\text{CO}_2$  and, possibly,  $\text{CF}_4$  [observed at  $1275$  and  $1260\text{ cm}^{-1}$  in the infrared

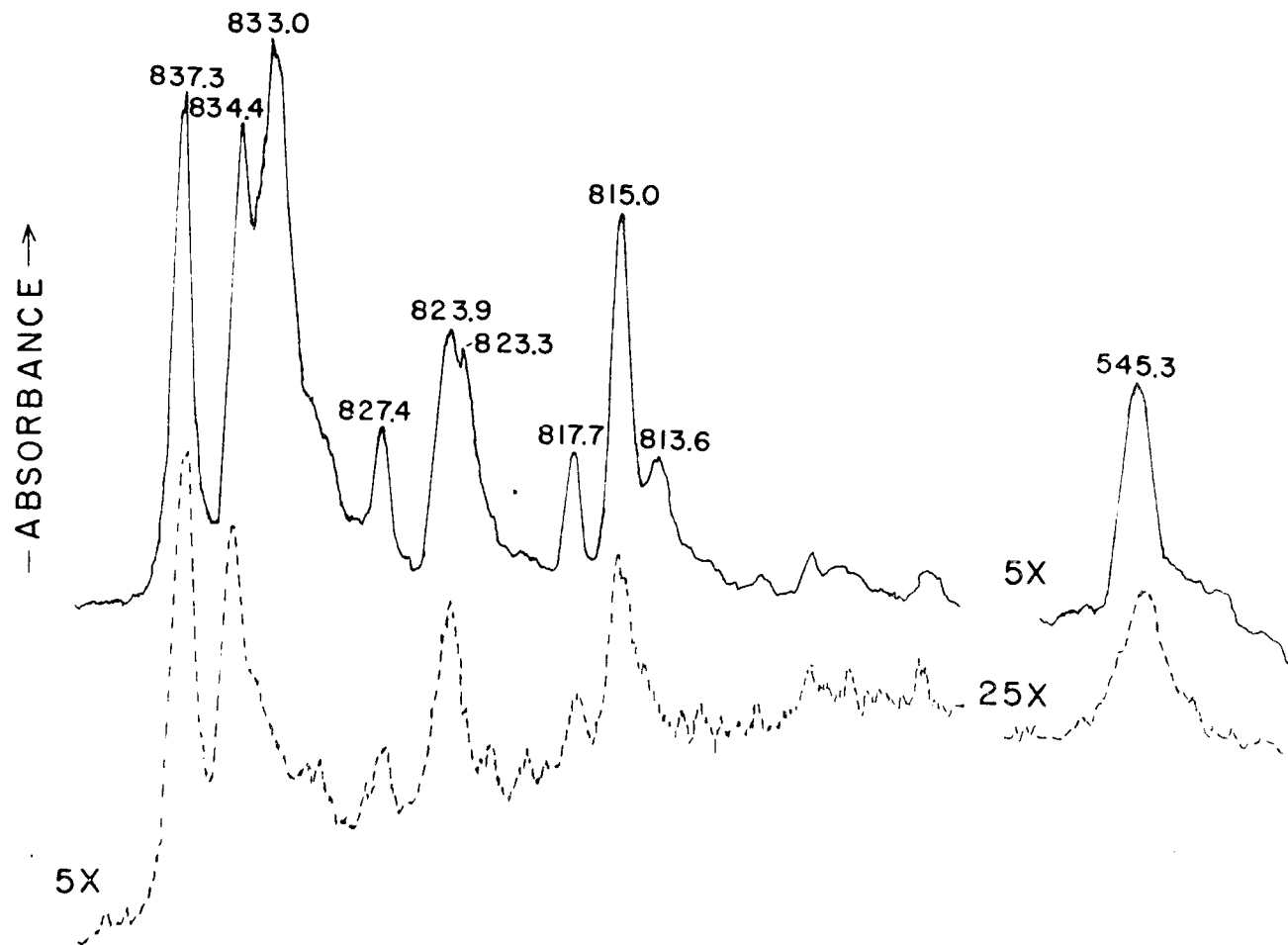


Fig. 12. Expanded scale of portions of the infrared trace of Fig. 11. — 14°K, --- after annealing to 35 - 40°K followed by recooling to 14°K. Scale amplification factors are indicated.

spectrum of matrices of pure krypton (MG Scientific, 99.95%) ] .

Small amounts of  $\text{H}_2\text{O}$  and sometimes  $\text{CO}$  and  $\text{CO}_2$  were detected in all experiments, and traces of  $\text{N}_2$  and  $\text{O}_2$  could conceivably be present although they were not observed in the Raman scans. Since the exact partner(s) involved in such complexes was not established in these studies, we shall refer to the complexes as  $\text{MgF}_2 \cdots \text{X}$ .

The infrared absorption at  $545.3 \text{ cm}^{-1}$  is of particular interest since it is nearly coincident with the  $\nu_1$  Raman band of  $\text{MgF}_2$ . However, diffusion results indicate that this band decreases at a faster rate than  $\nu_3$ , and other experiments at different effusion temperatures, etc., also suggest that this band is unrelated in intensity to either the monomer or dimer species. Possible explanations for these observations will be offered in the discussion section.

### $\text{MgF}_2$ in Argon

Fig. 13 shows the infrared and Raman spectra of  $\text{MgF}_2$  in argon matrices and the observed spectral features are given in Table 5. The infrared results were observed in experiments using a Ta Knudsen cell ( $T \simeq 1275^\circ\text{C}$ ) while the Raman spectrum was obtained using a graphite cell ( $T \simeq 1225^\circ\text{C}$ ) and higher dilution conditions in which the monomer was substantially favored. The upper trace is the infrared transmission spectrum; its features agree well with the results of HMK and the absorptions are analogous to those observed in krypton.

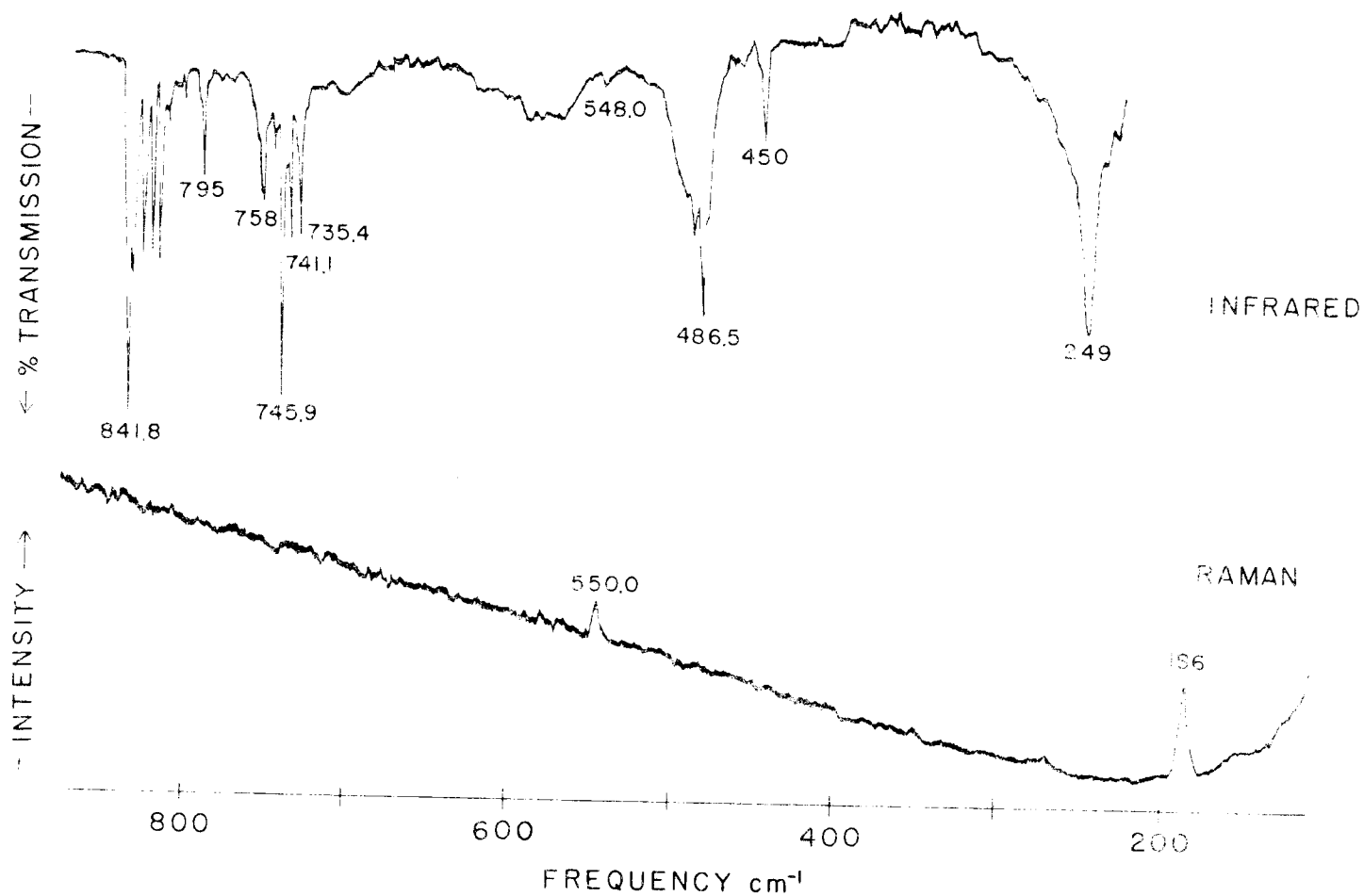


Fig. 13. Vibrational spectra of MgF<sub>2</sub> in an argon matrix. Infrared: 1.5 hr., T = 1275°C, SBW = 1 cm<sup>-1</sup>. Raman: 7.5 hr., T = 1225°C, 5145 Å, 1000 cps, SBW = 4 cm<sup>-1</sup>.

In the Raman spectrum, two significant features were detected (lower trace, Fig. 13), a band at  $550.0 \text{ cm}^{-1}$  which is assigned as  $\nu_1$  and a  $186 \text{ cm}^{-1}$  line of variable intensity (relative to  $\nu_1$ ) which is apparently the analog of the  $207 \text{ cm}^{-1}$  krypton matrix band. At the highest detection sensitivities two additional weak features were detected at  $584$  and  $354 \text{ cm}^{-1}$  and these could be due to dimers of  $\text{MgF}_2$ . No feature corresponding to  $\nu_3$  or  $\nu_2$  was observed in the Raman spectrum, but a weak counterpart of  $\nu_1$  was observed at  $548.0 \text{ cm}^{-1}$  in the infrared spectrum.

#### MgF<sub>2</sub> in Nitrogen

The infrared and Raman results for  $\text{MgF}_2$  in nitrogen are presented in Fig. 14 and Table 5. The infrared absorbance spectrum was recorded after a 2-hr deposit from a graphite cell at  $1225^\circ\text{C}$ . The spectrum is consistent with that reported by HMK above  $400 \text{ cm}^{-1}$  (their low frequency limit) except for a weak  $755.3 \text{ cm}^{-1}$  feature which they do not report. Concentration studies suggest that this band is not due to  $(\text{MgF}_2)_2$  but possibly to a complex,  $\text{MgF}_2 \cdots \text{X}$ . After an additional 2-hr deposit, the Raman spectrum was recorded in the same experiment (upper trace, Fig. 14). Though weak, a  $\nu_1$  candidate at  $514 \text{ cm}^{-1}$  is clearly discernible, along with a stronger feature at  $230 \text{ cm}^{-1}$  which is apparently the analog of the  $207 \text{ cm}^{-1}$  band in krypton.

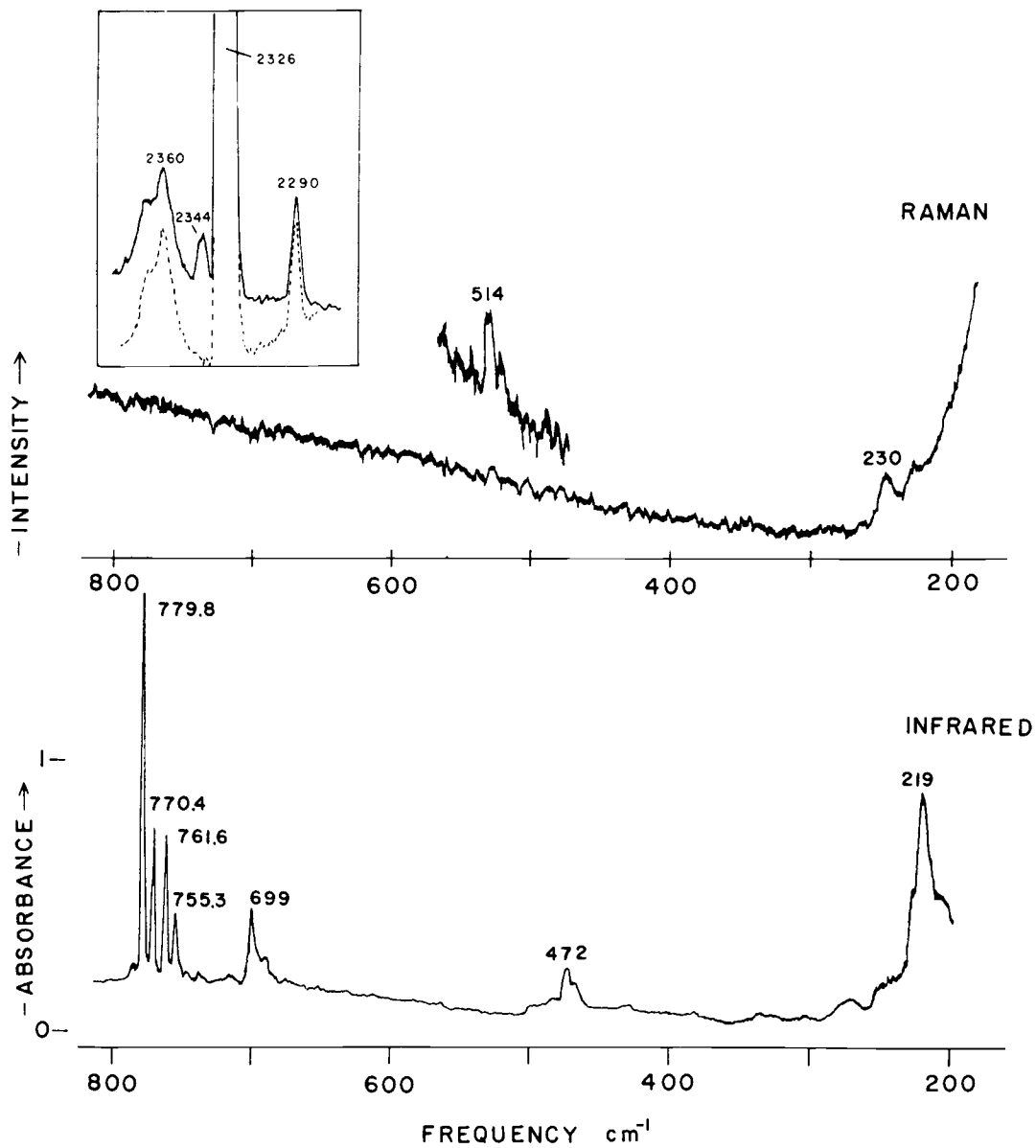


Fig. 14. Vibrational spectra of  $\text{MgF}_2$  in a  $\text{N}_2$  matrix. Raman: 4 hr.,  $T = 1225^\circ\text{C}$ ,  $5145 \text{ \AA}$ ,  $\text{SBW} = 5 \text{ cm}^{-1}$ , lower = 1000 cps, upper = 200 cps, inset = 2000 cps. Infrared: 2 hr.,  $T = 1225^\circ\text{C}$ ,  $\text{SBW} = 5 \text{ cm}^{-1}$ . Dashed trace = pure  $\text{N}_2$  at  $14^\circ\text{K}$ .

The frequency shifts in going from argon and krypton to nitrogen are unusually large and suggest that all the  $\text{MgF}_2$  is "complexed" in  $\text{N}_2$ . Support for this view comes from the Raman spectrum of the  $\text{N}_2$  stretching region (Fig. 14, inset) in which a weak  $\text{N}_2$  feature at  $2344 \text{ cm}^{-1}$  appears which is not present in the pure matrix (dashed trace). It may also be noted from this figure that the  $\text{MgF}_2$  concentration is quite low since the "complexed"  $\text{N}_2$  band at  $2344 \text{ cm}^{-1}$  is much weaker than the naturally occurring  $^{14}\text{N}^{15}\text{N}$  band (0.73%) at  $2290 \text{ cm}^{-1}$ . Since no trace of  $\nu_1$  was observed in the infrared spectrum, it also seems likely that more than one  $\text{N}_2$  is complexed to  $\text{MgF}_2$  in some manner such that the  $D_{\infty h}$  linear symmetry is not lowered.

#### $\text{MgCl}_2$ in Argon

The spectral results for  $\text{MgCl}_2$  in argon are displaced in Fig. 15 and Table 6. The Raman spectrum was recorded after a 2.5-hr deposit from a graphite cell at a temperature of  $775\text{-}800^\circ\text{C}$ . The strong band at  $326.5 \text{ cm}^{-1}$  can be assigned as  $\nu_1$  and the frequency shift for the 35-37 chlorine isotopic component ( $4.0 \text{ cm}^{-1}$ , Fig. 15, inset) of this band is in good agreement with that calculated ( $4.5 \text{ cm}^{-1}$ ) for a linear model. The corresponding 37-37 component was discernible but too weak to measure an accurate frequency shift. The broad feature at  $286 \text{ cm}^{-1}$  is attributed to dimeric  $\text{MgCl}_2$  and/or an impurity.

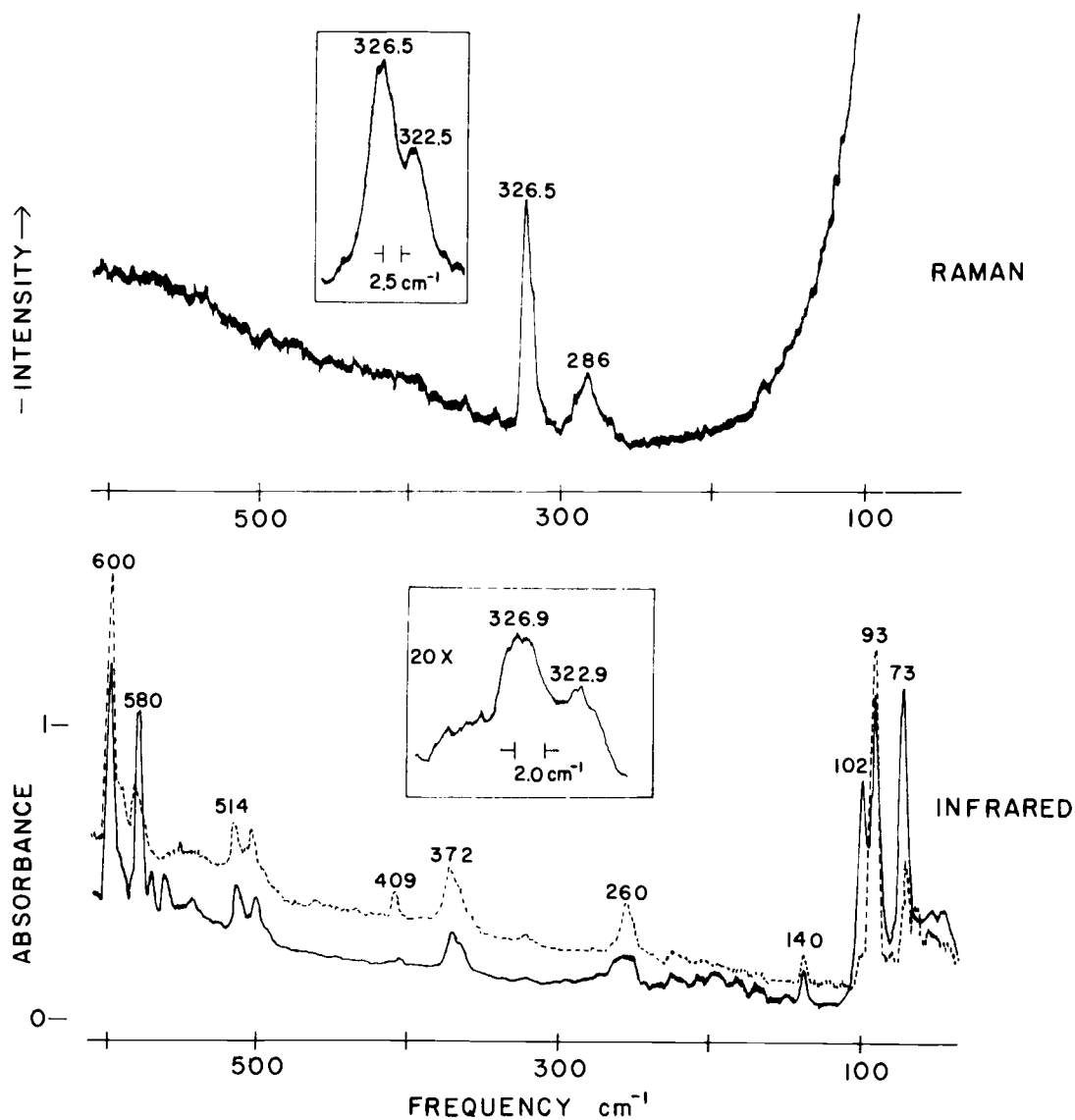


Fig. 15. Vibrational spectra of  $\text{MgCl}_2$  in an argon matrix. Raman: 2.5 hr,  $T = 800^\circ\text{C}$ ,  $5145 \text{ \AA}$ , 200 cps,  $\text{SBW} = 3 \text{ cm}^{-1}$ ; inset = 200 cps,  $\text{SBW} = 2.5 \text{ cm}^{-1}$ . Infrared: 1 hr.,  $T = 800^\circ\text{C}$ ,  $\text{SBW} = 1.5 \text{ cm}^{-1}$ , —  $14^\circ\text{K}$ , --- after annealing at  $35 - 40^\circ\text{K}$  followed by re-cooling to  $14^\circ\text{K}$ .

Table 6. Observed spectral features for  $\text{MgCl}_2$  isolated in Ar and  $\text{N}_2$  matrices.

	<u>Argon</u>	<u>Nitrogen</u>	<u>Assignment</u>
RAMAN: ( $\text{cm}^{-1}$ )		2360	$14,14\nu_{\text{N}_2} + \nu_{\text{N}_2}$ lattice
		2341	$\text{MgCl}_2 \cdots \text{N}_2$
		2326	$14,14\nu_{\text{N}_2}$
		2290	$14,15\nu_{\text{N}_2}$
		326.5	$\nu_1 \text{MgCl}_2$
		286	$(\text{MgCl}_2)_2$
INFRARED: ( $\text{cm}^{-1}$ )		2360	$14,14\nu_{\text{N}_2} + \nu_{\text{N}_2}$ lattice
		2340	$\text{MgCl}_2 \cdots \text{N}_2$
		2326	$14,14\nu_{\text{N}_2}$
	600-560	525-495	$\nu_3 \text{MgCl}_2$
		560	?
	514	473	$(\text{MgCl}_2)_2$
	409	447	$(\text{MgCl}_2)_2$ or ?
	372	347	$(\text{MgCl}_2)_2$
	260		$(\text{MgCl}_2)_2$
	190		?
	140		$(\text{MgCl}_2)_2$ or ?
	102-93		$\nu_2 \text{MgCl}_2$
73		induced lattice mode	

The infrared spectrum in Fig. 15 was recorded after a 1.0-hr deposit at effusion temperatures of 775-800°C. The solid trace was taken at 14°K while the dashed trace shows the changes in the spectrum after allowing diffusion to occur at 35-40°K and then recooling to 14°K. The high frequency multiplet near 600 cm<sup>-1</sup> can be assigned to  $\nu_3$  of MgCl<sub>2</sub>, in agreement with other workers (55, 56) and Fig. 16 shows this region at higher resolution. The complex multiplet structure is due to the isotopes of Mg and Cl in natural abundance and to the fact that the molecule appears to be isolated in three different sites (A, B, C). The calculated isotopic frequencies for a linear structure in each matrix site are compared with the observed values in Table 7, and the agreement is seen to be generally excellent. The  $\nu_2$  bending mode for MgCl<sub>2</sub> in two distinct sites was measured at 93 and 102 cm<sup>-1</sup> but no isotopic components were distinguishable at 1.0 cm<sup>-1</sup> resolution. [Calculations for  $\nu_2$  (Table 7) indicate that the isotopic splittings would probably not be separable at this resolution.] White et al. (56) report the bend at 87.7 cm<sup>-1</sup> in krypton. Our diffusion results indicate that sites B and C in argon are thermally unstable and largely site A is obtained on annealing.

The infrared bands at 514 (doublet), 409, 372 and 260 cm<sup>-1</sup> can be assigned to dimers of MgCl<sub>2</sub> on the basis of their intensity increase after diffusion and their increase in intensity relative to  $\nu_3$  in other experiments where the deposit rate was increased. The origin of the

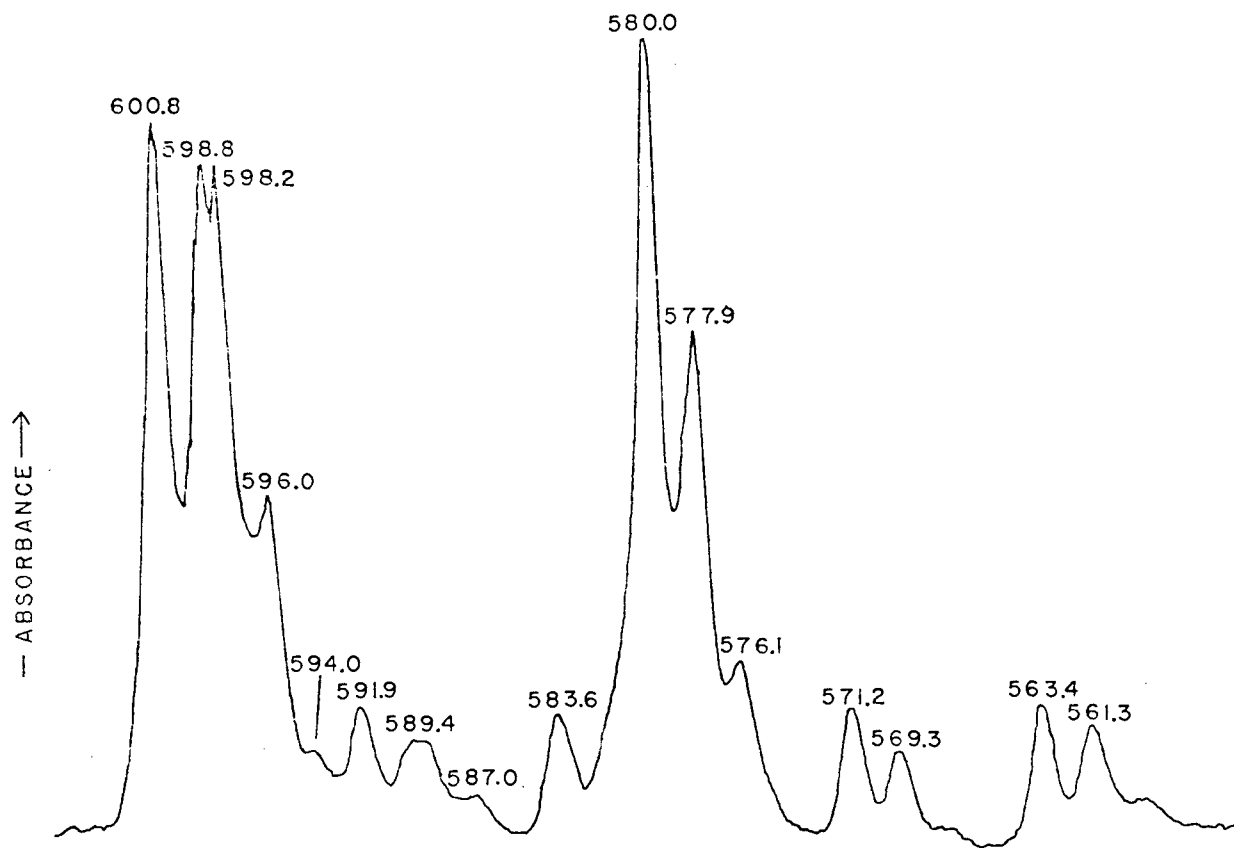


Fig. 16. Expanded scale of infrared (14°K) trace of MgCl<sub>2</sub>, ν<sub>3</sub> region, from Fig. 15, SBW = 0.6 cm<sup>-1</sup>.

Table 7. Observed and Calculated Fundamental Frequencies ( $\text{cm}^{-1}$ ) for  $\text{MgCl}_2$  in Argon.<sup>a</sup>

Species	Site A		Site B		Site C	
	Obs.	Calc.	Obs.	Calc.	Obs.	Calc.
$\nu_3$ : $^{24}\text{Mg}^{35,35}\text{Cl}_2$	600.8	(600.8)	598.2	(598.2)	580.0	(580.0)
$^{24}\text{Mg}^{35,37}\text{Cl}_2$	598.8	598.8	596.0	596.2	577.9	578.1
$^{24}\text{Mg}^{37,37}\text{Cl}_2$	--	596.6	594.0	594.1	576.1	576.0
$^{25}\text{Mg}^{35,35}\text{Cl}_2$	591.9	591.8	589.4	589.2	571.2	571.3
$^{25}\text{Mg}^{35,37}\text{Cl}_2$	589.4	589.7	587.0	587.2	569.3	569.3
$^{25}\text{Mg}^{37,37}\text{Cl}_2$	--	587.6	--	585.0	--	567.2
$^{26}\text{Mg}^{35,35}\text{Cl}_2$	583.6	583.4	--	580.8	563.4	563.2
$^{26}\text{Mg}^{35,37}\text{Cl}_2$	--	581.3	--	578.8	561.3	561.2
$^{26}\text{Mg}^{37,37}\text{Cl}_2$	--	579.1	--	576.6	--	559.0
$\nu_2$ : $^{24}\text{Mg}^{35,35}\text{Cl}_2$	93.0	(93.0) <sup>b</sup>			101.7	(101.7) <sup>b</sup>
$^{25}\text{Mg}^{35,37}\text{Cl}_2$	--	91.6			--	100.2
$^{26}\text{Mg}^{37,37}\text{Cl}_2$	--	90.3			--	98.7
$\nu_1$ : $\text{Mg}^{35,35}\text{Cl}_2$	326.5	(326.5)				
$\text{Mg}^{35,37}\text{Cl}_2$	322.5	322.0				
$\text{Mg}^{37,37}\text{Cl}_2$	--	317.6				

<sup>a</sup>All frequencies are believed to be accurate to  $\pm 0.5 \text{ cm}^{-1}$ .

<sup>b</sup>The calculated isotopic splittings of  $\nu_2$  for  $\text{Mg}^{35,37}\text{Cl}_2$  and  $\text{Mg}^{37,37}\text{Cl}_2$  were  $\sim .35 \text{ cm}^{-1}$  and not experimentally resolved.

band at  $140\text{ cm}^{-1}$  is not readily apparent and little can be said about this band except that its intensity decreases after diffusion. The band near  $70\text{ cm}^{-1}$  is apparently due to an induced phonon mode in the Ar lattice; it has been observed by others (29, 30).

It is interesting to examine the  $325\text{ cm}^{-1}$   $\nu_1$  region in the infrared more closely. On initial inspection (solid line, Fig. 16) there is little evidence of an absorption in this area. However, when an ordinate expansion of 20x is used, a doublet at  $326.9$  and  $322.9\text{ cm}^{-1}$  becomes apparent as shown in the inset. Although this is a very weak band, its intensity was observed to increase by one-third after allowing diffusion to occur. The possible implications of this observation will be discussed later.

### MgCl<sub>2</sub> in Nitrogen

As for MgF<sub>2</sub>, large vibrational frequency shifts were observed for MgCl<sub>2</sub> in a nitrogen matrix (Fig. 17 and Table 6). The infrared region to  $250\text{ cm}^{-1}$  is dominated by a strong  $\nu_3$  multiplet at  $523\text{ cm}^{-1}$  while the Raman spectrum shows only the  $\nu_1$  band at  $286\text{ cm}^{-1}$ . In addition, several weaker features at 473, 447, and  $347\text{ cm}^{-1}$  can be attributed to dimers, and the origin of the band at  $560\text{ cm}^{-1}$  is not readily apparent since the relative intensity of this absorption did not correlate with the relative intensities of either the monomer or the dimer bands. The large frequency shifts relative to argon ( $\Delta\nu_3 = -77$ ,

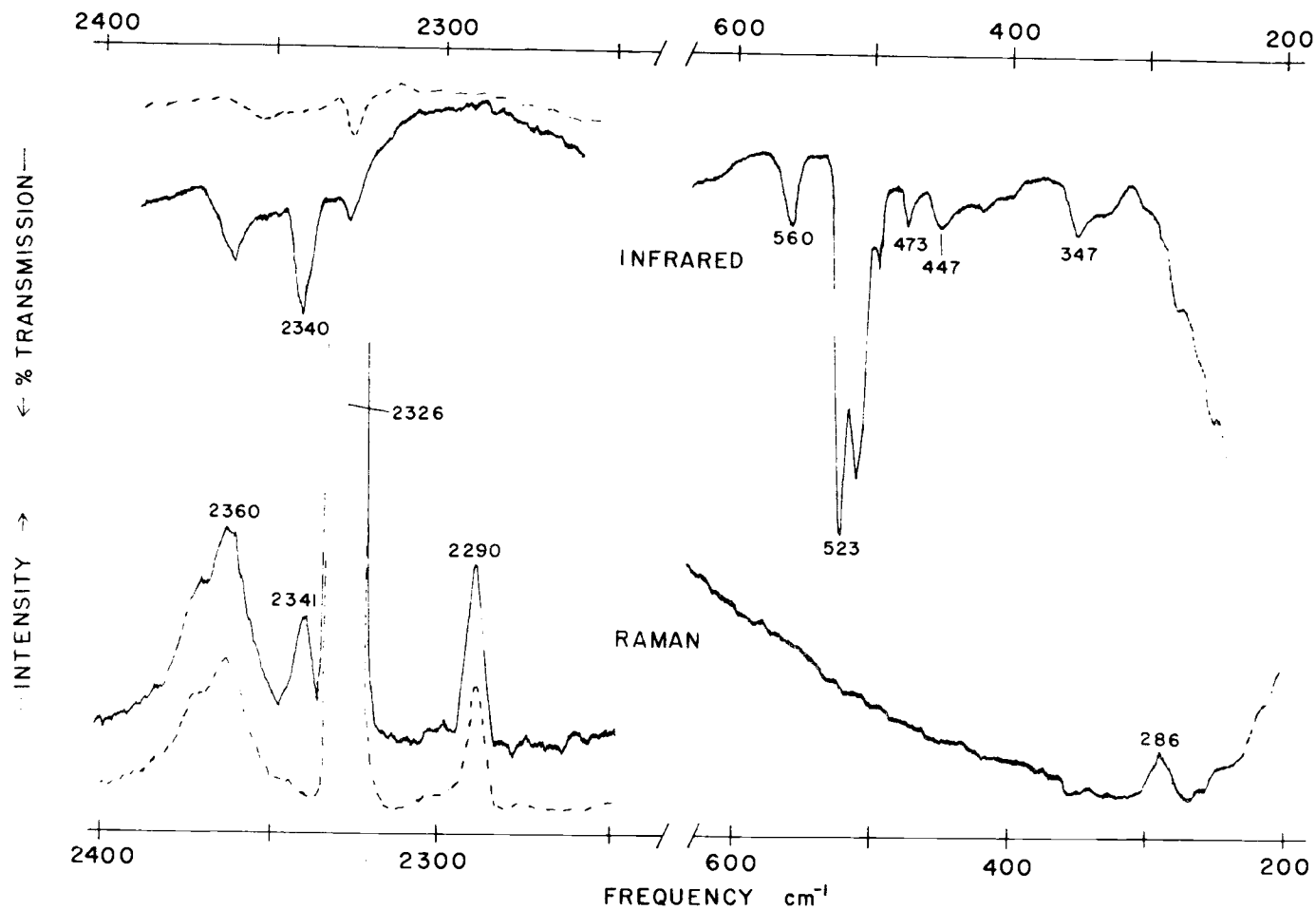


Fig 17. Vibrational spectra of MgCl<sub>2</sub> in a nitrogen matrix. Infrared: 2.5 hr., T = 800°C, SBW = 2.5 cm<sup>-1</sup>. Raman: 5 hr., T = 800°C, SBW = 4 cm<sup>-1</sup>, 600-200 cm<sup>-1</sup> = 500 cps, SBW = 5 cm<sup>-1</sup>; 2400-2250 cm<sup>-1</sup> = 5000 cps, SBW = 4 cm<sup>-1</sup>. Dashed trace = pure N<sub>2</sub>.

$\nu_1 = -40 \text{ cm}^{-1}$ ) are indicative of a strong interaction between  $\text{N}_2$  and  $\text{MgCl}_2$ . To investigate this effect further infrared and Raman spectra in the  $\text{N}_2$  stretching region were examined and the results are also shown in Fig. 17. The dashed trace in both spectra corresponds to pure  $\text{N}_2$  while the solid trace was recorded for the matrix isolated sample. After deposition, a new Raman feature appears at  $2341 \text{ cm}^{-1}$  very near but not identical with the  $2344 \text{ cm}^{-1}$  value observed for  $\text{MgF}_2$  in  $\text{N}_2$ . This feature also appears in the infrared at  $2340 \text{ cm}^{-1}$  along with a  $\text{N}_2$  + lattice combination band at  $2360 \text{ cm}^{-1}$ . Thus for both  $\text{MgCl}_2$  and  $\text{MgF}_2$ , a weak complex with  $\text{N}_2$  forms quite readily.

#### MgBr<sub>2</sub> in Argon

Argon matrix results for  $\text{MgBr}_2$  are presented in Fig. 18 and Table 8. The solid trace in the Raman spectrum was recorded after a 4.5-hr deposit from a graphite cell at an effusion temperature of  $\sim 750^\circ\text{C}$ . The dashed trace was obtained for the same sample after annealing to  $35^\circ\text{K}$  and then recooling to  $14^\circ\text{K}$ . A doublet at 207.2 and  $197.9 \text{ cm}^{-1}$  dominates the spectrum, and this feature can readily be assigned to  $\nu_1$  of  $\text{MgBr}_2$  isolated in two different matrix sites. Only one site ( $197.9 \text{ cm}^{-1}$ ) is favored as annealing occurs as indicated by the dashed trace. The inset of Fig. 18, recorded at a spectral band width (SBW) =  $0.8 \text{ cm}^{-1}$ , revealed no conclusive evidence of Mg or Br isotopic splittings, an observation in accord with calculated splittings

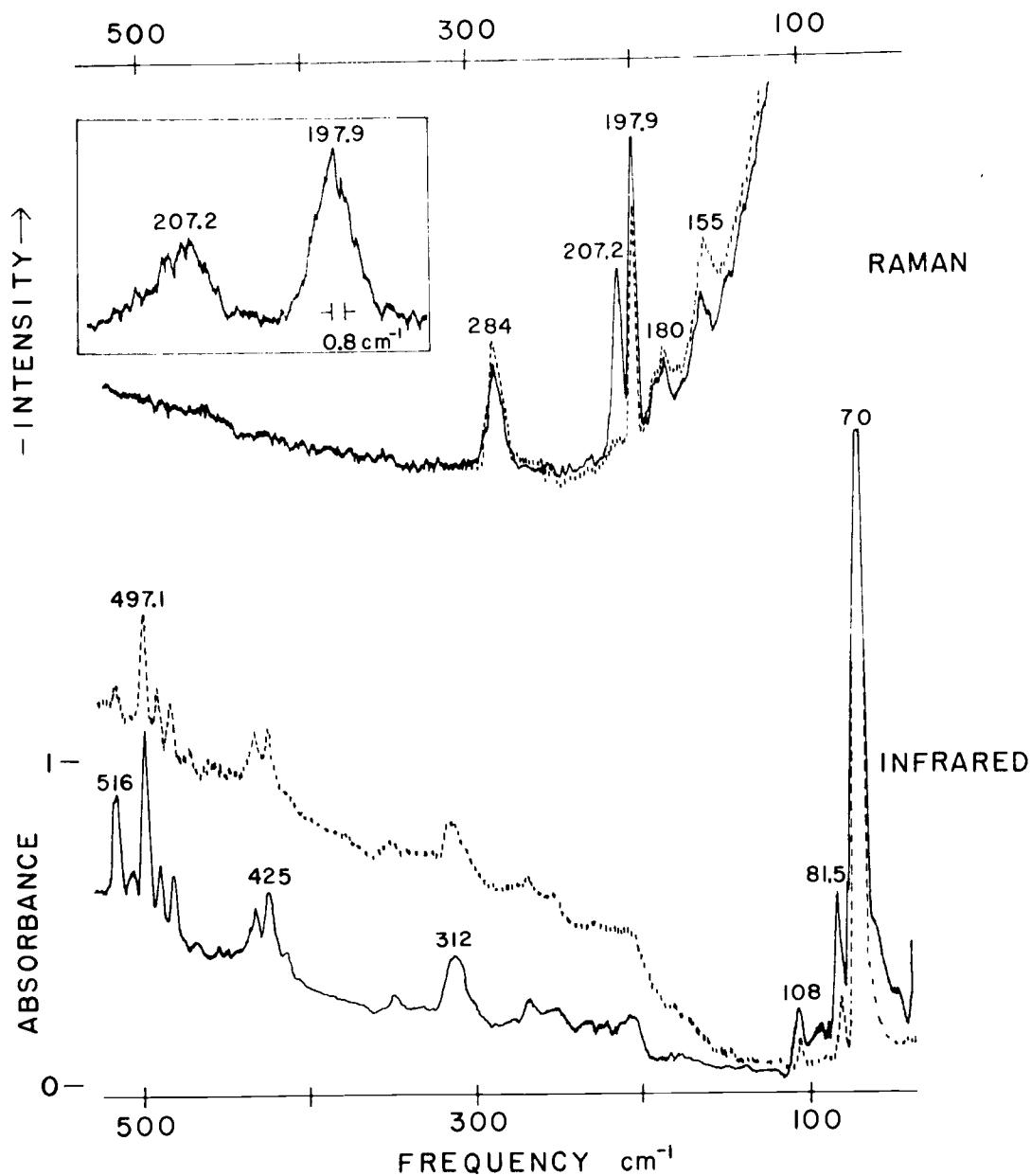


Fig. 18. Vibrational spectra of  $\text{MgBr}_2$  in an argon matrix. Raman: 4.5 hr,  $T = 750^\circ\text{C}$ ,  $5145 \text{ \AA}$ , 500 cps,  $\text{SBW} = 4 \text{ cm}^{-1}$ ; inset = 50 cps,  $\text{SBW} = 0.8 \text{ cm}^{-1}$ . Infrared: 1 hr.,  $T = 750^\circ\text{C}$ ,  $\text{SBW} = 2 \text{ cm}^{-1}$ .  
 —  $14^\circ\text{K}$ , --- after annealing at  $35-40^\circ\text{K}$  followed by re-cooling to  $14^\circ\text{K}$ .

Table 8. Observed and Calculated Fundamental Frequencies ( $\text{cm}^{-1}$ ) for  $\text{MgBr}_2$  and  $\text{MgI}_2$  in Argon.<sup>a</sup>

	Species	Obs.	Calc. <sup>b</sup>	Species	Obs.	Calc.
$\nu_3$ :	$^{24}\text{Mg}^{79,81}\text{Br}_2$	497.1	(497.1)	$^{24}\text{MgI}_2$	444.9	(444.9)
	$^{25}\text{Mg}^{79,81}\text{Br}_2$	488.4	488.4	$^{25}\text{MgI}_2$	437.0	436.7
	$^{26}\text{Mg}^{79,81}\text{Br}_2$	480.4	480.3	$^{26}\text{MgI}_2$	428.7	429.0
$\nu_2$ :	$^{24}\text{Mg}^{79,81}\text{Br}_2$	81.5	(81.5)	$^{24}\text{MgI}_2$	55.8	(55.8)
	$^{25}\text{Mg}^{79,81}\text{Br}_2$	--	80.1	$^{25}\text{MgI}_2$		54.8
	$^{26}\text{Mg}^{79,81}\text{Br}_2$	--	78.7	$^{26}\text{MgI}_2$		53.8
$\nu_1$ :	$\text{Mg}^{79,81}\text{Br}_2$	197.9	(197.9)	$\text{MgI}_2$	147.6	(147.6)

<sup>a</sup>All frequencies are believed to be accurate to  $\sim 0.5 \text{ cm}^{-1}$ .

<sup>b</sup>The calculated isotopic splittings for  $\text{Mg}^{79,79}\text{Br}_2$  and  $\text{Mg}^{81,81}\text{Br}_2$  were small ( $\sim 0.4 \text{ cm}^{-1}$  for  $\nu_3$ ,  $\sim 0.07 \text{ cm}^{-1}$  for  $\nu_2$ ,  $\sim 1.25$  for  $\nu_1$ ) and not experimentally resolved.

for a linear model (Table 9). The bands at 180 and 155  $\text{cm}^{-1}$  are attributable to dimers of  $\text{MgBr}_2$  on the basis of their intensity increase with respect to  $\nu_1$  during warmup experiments. The intensity of the 284  $\text{cm}^{-1}$  feature also increases relative to  $\nu_1$  as diffusion proceeds near 40°K, but it seems too high a frequency to be due to dimers or aggregates of  $\text{MgBr}_2$ . Since a feature near this frequency was also observed for  $\text{MgCl}_2$  in argon, it may arise from a volatile impurity common to both  $\text{MgCl}_2$  and  $\text{MgBr}_2$ . It should be noted that this frequency is uncomfortably close to the 286  $\text{cm}^{-1}$   $\text{MgCl}$  value in a  $\text{N}_2$  matrix. Despite this, we feel that the latter feature is indeed  $\nu_1$  since no other candidate for  $\nu_1$  was observed in nitrogen even though the 2341  $\text{cm}^{-1}$  band characteristic of  $\text{MgCl}_2 \cdots (\text{N}_2)_n$  was seen.

The infrared spectrum was obtained after a 2-hr deposit at an effusion temperature of 750°K; the solid trace was recorded at 14°K while the dashed trace shows the results of annealing to 35°K. The multiplet near 500  $\text{cm}^{-1}$  is readily assigned to  $\nu_3$  of the various magnesium isotopes in  $\text{MgBr}_2$  isolated in multiple matrix sites. After diffusion the site at 497.1  $\text{cm}^{-1}$  predominates and the observed splittings due to the Mg isotopes agree well with the calculated values given in Table 9. The calculations further suggest the multiplet structure due to the Br isotopes will not be experimentally resolvable. A number of other weaker absorptions in the spectrum, such as the features at 425, 312 and 108  $\text{cm}^{-1}$ , are attributable to aggregates of

Table 9. Observed spectral features for  $\text{MgBr}_2$  and  $\text{MgI}_2$  isolated in an argon matrix.

	<u>MgBr<sub>2</sub></u>	<u>MgI<sub>2</sub></u>	<u>Assignment</u>
RAMAN: (cm <sup>-1</sup> )	197.9	147.6	$\nu_1$ site A
	207.2		$\nu_1$ site B
	180	110	(MgX <sub>2</sub> ) <sub>2</sub>
	155		(MgX <sub>2</sub> ) <sub>2</sub>
	285		(MgX <sub>2</sub> ) <sub>x</sub>
		213.5 424.2 634.3	I <sub>2</sub> (Resonance Raman)
INFRARED: (cm <sup>-1</sup> )	497.1	444.9	$\nu_3$ site A
	516	450.5	$\nu_3$ site B
		410	?
	425	387	(MgX <sub>2</sub> ) <sub>2</sub>
	312	274	(MgX <sub>2</sub> ) <sub>2</sub> or (MgX <sub>2</sub> ) <sub>x</sub>
	210		(MgX <sub>2</sub> ) <sub>2</sub> or ?
	108	92	(MgX <sub>2</sub> ) <sub>2</sub>
	81.5	55.8	$\nu_2$
	72	72	induced lattice mode

MgBr<sub>2</sub> on the basis of their intensity changes after diffusion and their increase in intensity relative to  $\nu_3$  as the deposit rate was increased in other experiments. The intensity variations of the band at 81.5 cm<sup>-1</sup> parallel those of the  $\nu_3$  mode and this feature is assigned to  $\nu_2$  of MgBr<sub>2</sub>. No isotopic structure was experimentally observed for this band and again calculations (Table 9) indicate that this is reasonable. The strong absorption near 70 cm<sup>-1</sup> is similar to the induced lattice mode that was also observed in the MgCl<sub>2</sub> experiments. Careful examination of the 200 cm<sup>-1</sup> region in the infrared did not conclusively reveal the presence of any features that might be coincident with  $\nu_1$  (observed at 197.9 and 207.2 cm<sup>-1</sup> in the Raman). However, it must be pointed out that due to the noise and sloping background in this region, a very weak absorption could escape detection.

#### MgI<sub>2</sub> in Argon

The infrared and Raman spectra of MgI<sub>2</sub> generated in a graphite Knudsen cell at  $\sim 700^\circ\text{C}$  and isolated in an argon matrix are presented in Fig. 19 and a frequency summary is given in Table 8. For the Raman scans, the sample was deposited for three hours and the upper and lower traces were recorded with 4880 Å and 5145 Å excitation, respectively; all other instrument parameters were the same. The features at 213.5, 424.2 and 634.3 cm<sup>-1</sup> are similar to the Resonance Raman spectrum of argon matrix isolated I<sub>2</sub> reported

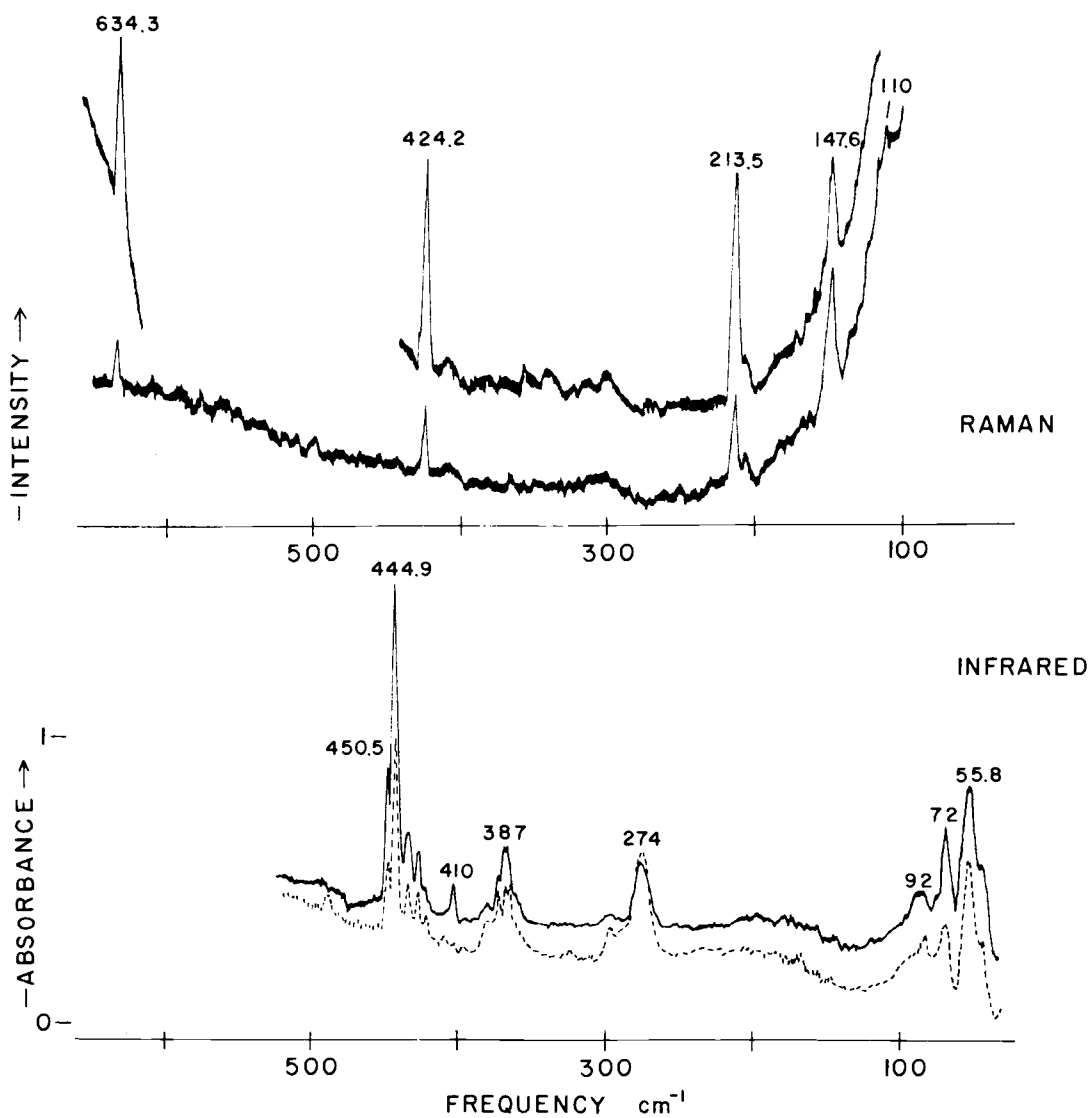


Fig. 19. Vibrational spectra of  $\text{MgI}_2$  in an argon matrix. Raman: 3 hr,  $T = 700^\circ\text{C}$ , 300cps, SBW =  $4 \text{ cm}^{-1}$ , upper -  $5145 \text{ \AA}$ , lower -  $4880 \text{ \AA}$ . Infrared: 1.5 hr.,  $T = 700^\circ\text{C}$ , SBW =  $2 \text{ cm}^{-1}$ , —  $14^\circ\text{K}$ , --- after annealing at  $35 - 40^\circ\text{K}$  followed by recooling to  $14^\circ\text{K}$ .

by Howard and Andrews (59). The  $I_2$  is apparently formed from decomposition of  $MgI_2$  but since the matrix was not colored the amount of  $I_2$  present must have been small. The band at  $147.6\text{ cm}^{-1}$  can be assigned to  $\nu_1$  of  $MgI_2$  and a weak feature near  $110\text{ cm}^{-1}$  can tentatively be assigned to  $MgI_2$  dimer.

The infrared spectrum was obtained after a 1.5-hr deposit under the same conditions as those for the Raman experiment; the solid trace was recorded at  $14^\circ\text{K}$  while the dashed trace shows the results after diffusion at  $35\text{-}40^\circ\text{K}$  followed by recooling to  $14^\circ\text{K}$ . The spectrum is similar to that of  $MgBr_2$  in that the multiplet structure for  $\nu_3$  is due to  $^{24,25,26}\text{MgI}_2$  isolated in two different sites. After annealing occurs at  $35\text{-}40^\circ\text{K}$ , the site at  $444.9\text{ cm}^{-1}$  is seen to be slightly favored, and after further diffusion occurs at  $40\text{-}45^\circ\text{K}$ , the  $450.5\text{ cm}^{-1}$  site almost completely disappears. The spectrum after this higher temperature annealing experiment is not shown since the quality of the overall trace was poor due to the increased scattering of the matrix. The absorptions at  $387$  and  $92\text{ cm}^{-1}$  increase relative to  $\nu_3$  after diffusion occurs and can readily be assigned to dimers. The band at  $274\text{ cm}^{-1}$  also gains intensity after diffusion and can be assigned either to dimer or aggregate species. The weak feature at  $410\text{ cm}^{-1}$  decreases significantly after warmup to  $35\text{-}40^\circ\text{K}$  and its origin is not apparent. In the low frequency region, the absorption near  $72\text{ cm}^{-1}$  is due to induced modes in the argon matrix as previously

noted for  $\text{MgCl}_2$  and  $\text{MgBr}_2$  matrices. The feature at  $55.8 \text{ m}^{-1}$  can be attributed to  $\nu_2$  of  $\text{MgI}_2$  and calculations (Table 9) indicate that the magnesium isotopic splittings will probably not be resolvable. The intensity of this  $\nu_2$  mode does not decrease as rapidly as  $\nu_3$  after diffusion; however, contribution to the  $\nu_2$  intensity from low frequency dimer modes could account for this anomalous result. Examinations of the  $\nu_1$  area in the infrared did not reveal any features; however, the relatively high noise level in this region ( $\approx 150 \text{ cm}^{-1}$ ) could preclude the observation of a very weak band. Table 9 summarizes the observed and calculated fundamental vibrations for  $\text{MgI}_2$ .

## Discussion

### Frequency Assignments and Structural Implications

A summary of the fundamental frequencies of vibration ( $\nu_1$ , symmetric stretch;  $\nu_2$ , bend;  $\nu_3$ , asymmetric stretch) for the magnesium dihalides isolated in argon matrices is given in Table 10. The assignment of these fundamental modes is straightforward since it is usually the case that, for a  $\text{MX}_2$  molecule in the infrared,  $\nu_3$  has the highest frequency and intensity, while  $\nu_2$  is most often observed at low frequencies. With these generalizations in mind we have assigned  $\nu_3$  and  $\nu_2$  as indicated in Table 10 and as previously

Table 10. Vibrational Frequencies and Force Constants for the Magnesium Dihalides in Argon.

Argon Matrix Frequencies ( $\text{cm}^{-1}$ )		$\nu_1$	$\nu_2$	$\nu_3$
MgF <sub>2</sub>		550.0	249.0	841.8
MgCl <sub>2</sub>		326.5	93.0	600.8
MgBr <sub>2</sub>		197.9	81.5	497.1
MgI <sub>2</sub>		147.6	55.8	444.9

Internal Force Constants ( $\text{mdyn}/\text{\AA}$ )		Ref.	$k_r$	$k_{rr}$	$ka/\text{\AA}^2$	
MgF <sub>2</sub>	Exp.		<u>3.228</u>	<u>0.158</u>	<u>0.1343</u>	
	Theoretical Results <sup>a</sup>					
	1) Ionic Models					
		polarizable ions model	62	---	---	0.108
		ion-ion interaction model <sup>b</sup>	53	4.34	0.099	0.060
	2) Semi-Empirical Models					
		CNDO/2 ( $\alpha = 140^\circ$ )	49	---	---	0.041
		INDO ( $\alpha = 130^\circ$ )	49	---	---	0.37
	3) SCF-MO A Priori Models					
		Slater basis (Mg; s,p)	49	---	---	(0.029) <sup>c</sup>
	Gaussian basis (Mg; s,p)	51	2.13	---	0.162	
	Gaussian basis (Mg; s,p,d)	51	2.30	---	0.186	
MgCl <sub>2</sub>	Exp.		<u>2.048</u>	<u>0.149</u>	<u>0.0228</u>	
		polarizable ions model	62	---	---	0.078
		ion-ion interaction model <sup>b</sup>	53	1.94	0.043	0.029
MgBr <sub>2</sub>	Exp.		<u>1.669</u>	<u>0.153</u>	<u>0.0204</u>	
		polarizable ions model	62	---	---	0.075
		ion-ion interaction model		---	---	0.023
MgI <sub>2</sub>	Exp.		<u>1.454</u>	<u>0.175</u>	<u>0.0100</u>	
		polarizable ions model	62	---	---	0.067
		ion-ion interaction model		---	---	0.018

a All calculations for all dihalides assumed or predicted linear configurations except for the semi-empirical results for MgF<sub>2</sub>. In these two cases, predicted bond angles ( $\alpha$ ) are shown.

b Values listed here were deduced from the frequencies calculated in reference 53 with the exception of  $ka/\text{\AA}^2$  which is smaller here by a factor of 4. This factor comes from a minor error in the calculation of  $ka$  in that work.

c A lower limit calculated by us from the variation of energy with angle reported in reference 49.

mentioned, our results for  $\nu_3$  and  $\nu_2$  of  $\text{MgF}_2$  and  $\text{MgCl}_2$  agree with the observations of other investigators (44, 46, 47, 55).

In the Raman spectrum  $\nu_1$  will have the highest intensity, moreover if the molecule is linear, only  $\nu_1$  will be Raman active. Since the composition of the vapor (58) of the magnesium dihalides is 99%  $\text{MX}_2$ , we would expect one strong band, characteristic of the  $\nu_1$  mode, if the molecule is linear. Indeed, this is what is observed for all the magnesium dihalides. The Raman spectrum, in some cases, was complicated by scattering from other species such as  $(\text{MX}_2)_2$  molecules. Effects such as fluorescence (see  $\text{MgF}_2$ ) or Resonance Raman (see  $\text{MgI}_2$ ) can also make the spectrum difficult to interpret. In addition, the intensity of the  $\nu_1$  mode, although strongest in the Raman, is inherently weak for such molecules as  $\text{MgF}_2$  due to the relatively small change in polarizability associated with the symmetric stretching of the F atoms. Nonetheless, we are confident in our assignments for  $\nu_1$  since most of the complicating features have all been identified by varying deposit conditions or by controlled diffusion experiments or by changing the frequency of the source radiation. One exception is the band at  $207 \text{ cm}^{-1}$  in krypton ( $186 \text{ cm}^{-1}$  in argon,  $230 \text{ cm}^{-1}$  in nitrogen) for which a number of possible origins were eliminated as previously discussed. Since this feature does not correlate with any other Raman bands the only remaining choice seems to be to classify it as a volatile impurity which was produced only in certain experiments.

Having assigned the fundamental vibrations we can deduce the symmetry of these molecules from selection rule considerations. In the Raman spectrum we observe only  $\nu_1$  and no indication of  $\nu_3$  or  $\nu_2$ ; this fact alone indicates that the molecules are linear. However, the observation of a weak feature in the infrared nearly coincident with the  $\nu_1$  Raman mode for  $\text{MgF}_2$  and  $\text{MgCl}_2$  is not strictly consistent with the selection rules for  $D_{\infty h}$  symmetry. The measured Raman frequencies are calibrated with respect to the frequency of the exciting radiation while the infrared bands are calibrated with respect to  $\text{CO}_2$  or  $\text{H}_2\text{O}$  absorptions. A conservative estimate of the experimental error in the measured frequencies is  $\pm 0.5 \text{ cm}^{-1}$ . For  $\text{MgF}_2$  in a krypton matrix  $\nu_1 = 544.5$  (Raman) and we observe a weak feature at  $545.3 \text{ cm}^{-1}$  (infrared). A similar comparison for the argon matrix results shows  $\nu_1 = 550.0$  (Raman) and a weak feature at  $548.0 \text{ cm}^{-1}$  (infrared). For  $\text{MgCl}_2$  in an argon matrix,  $\nu_1 = 326.5 \text{ cm}^{-1}$  (Raman) and an extremely weak feature was observed at  $326.9 \text{ cm}^{-1}$  (infrared). Especially compelling for  $\text{MgCl}_2$  is the observed  $4.0 \text{ cm}^{-1}$  splitting in both the Raman and infrared for  $\text{Mg}^{35, 37}\text{Cl}_2$ . The experimental evidence indicates that these weak features in the infrared can be assigned to the  $\nu_1$  mode. This implies  $C_{2v}$  symmetry, however we do not favor this conclusion for several reasons: 1) we have observed, as did (HMK), that, although these infrared bands are weak, their intensity behavior did not parallel that of the  $\nu_3$  mode, 2)  $\nu_3$  and  $\nu_2$  were not

observed in the Raman spectrum although the noise level could preclude the detection of weak features, 3) (HMK) has indicated that in unpublished studies, a band in the infrared spectrum of  $\text{MgF}_2$  in argon at  $552 \text{ cm}^{-1}$  can be attributed to infrared activity induced in  $\nu_1$  as a result of complexes of the type  $\text{MgF}_2 \cdots \text{X}_n$ . In view of these arguments we believe that these weak infrared absorptions are in fact due to the  $\nu_1$  vibration arising from the molecule perturbed by a matrix effect. The intensity of this band in the infrared did seem to correlate with bands attributed to complexes ( $823.9$  and  $815.0 \text{ cm}^{-1}$  in krypton for  $\text{MgF}_2$ ), although, since it was so weak quantitative measurements were not possible.

In summary, at the present time the experimental evidence indicates that all the magnesium dihalides are linear with some infrared activity induced in  $\nu_1$  as the result of a matrix effect. This effect is most likely due to complex formation and it appears that  $\text{MgF}_2$  is the most easily complexed species in the series since the intensity of the induced  $\nu_1$  mode in the infrared was highest for this molecule. Further work concerning the nature of these complexes is in progress by Hauge and coworkers (60).

### Force Constants and Bonding

The measurement of all three fundamental frequencies for the linear  $\text{MgX}_2$  compounds allows accurate potential constants to be

determined for the first time (Table 10). For  $\text{MgF}_2$ , the stretching force constant ( $k_r = 3.23 \text{ mdyn/\AA}$ ) is not significantly changed from that for diatomic  $\text{MgF}$  [ $3.14 \text{ mdyn/\AA}$  (61)], but for the other dihalides,  $k_r$  is 15-25% greater than for the diatomic molecule [ $k_r = 1.78, 1.49, 1.16 \text{ mdyn/\AA}$  for  $\text{MgCl}, \text{MgBr},$  and  $\text{MgI}$  respectively (61)]. For every halide, the value of  $k_r$  for  $\text{MgX}_2$  is almost twice that of the corresponding  $\text{NaX}$  molecule (61), a species in which the bonding is largely ionic (53). Presumably these larger values arise mostly from the double charge on the Mg cation but part of the increase may result from greater covalent contributions to the bonding.

The force constants serve as one of the few available tests of a number of theoretical models for the bonding in the alkaline earth dihalides and in  $\text{MgF}_2$  in particular. Since much of the effort in the latter case has been to explain the "non-linearity" of  $\text{MgF}_2$ , most of the calculations have examined the variation of energy with bond angle. Thus bending force constants are readily available even though the stretching constants were not always obtained. These theoretical values are compared with the experimental results in Table 10 and a number of observations can be made.

First, it may be noted that the semi-empirical models for  $\text{MgF}_2$  were the only ones to produce an energy minimum for the bent configuration, a structure known to be incorrect. These calculations also yield poor values for  $k_\alpha / l^2$ . Some of the extensive SCF-MO

calculations give better results for the bending force constants but the values of  $k_r$  are too low. This latter feature is apparently characteristic of Hartree-Fock calculations and is due to the failure of the Hartree-Fock wavefunction to lead to the proper dissociation into neutral atoms (51). It may be worth noting that inclusion of 3d orbitals for the Mg atom gives a slight improvement for  $k_r$  but a poorer (higher) value for  $k_\alpha / l^2$ . This is the opposite direction to the expected since d orbitals are thought to favor the bent configuration (48). However, at larger angles, a flatter potential curve does result for the s, p, d basis set and, moreover, similar calculations for  $\text{CaF}_2$  successfully predict the observed bent structure when d orbitals are included. Presumably, extensions of these calculations using larger basis sets and configuration interaction could provide closer agreement with experiment albeit at greater cost.

Force constants deduced for two ionic bonding descriptions are also presented. The polarizable ions model is based on the electrostatic energy obtained classically for three spherical conductors with radii corresponding to the polarizability volume. The resultant bending force constant is fairly close for  $\text{MgF}_2$  but is increasingly too high as one goes from Cl to Br to I. The second ionic model is based on the pairwise summation of ion-ion interaction potentials deduced by Kim and Gordon (53) from electron density functions for individual ions. In this model, the bending force constant was deduced solely from the

electrostatic repulsion of the  $F^-$  anions but it appears that an error of a factor of four was made in expanding the  $e^2/(R_1 + R_2)$  potential in terms of a bending coordinate  $\alpha$ . We obtain  $k_\alpha/\ell^2 = e^2/8\ell^3$  from this expansion (rather than  $e^2/2\ell^3$ ) and our tabulated values reflect this correction. The results are low by a factor of  $\simeq 2$  for  $MgF_2$  but are reasonably close for  $MgCl_2$ . Although Kim and Gordon (53) do not report potentials for  $MgBr_2$  and  $MgI_2$ ,  $k_\alpha/\ell^2$  values are listed in Table 10 which we have calculated from the experimental equilibrium bond distances and again the agreement is surprisingly good. Stretching force constants were also obtained from the ion-ion interaction model, and although the  $MgF_2$  value for  $k_r$  is high by  $\simeq 35\%$ , the value for  $MgCl_2$  is within 5% of the experimental result. Moreover, the correct sign for the interaction constant  $k_{rr}$  is obtained and the magnitude is reasonably close for both  $MgF_2$  and  $MgCl_2$ . It may be noted that the experimental value for  $k_{rr}$  is small for all the dihalides (0.15-0.18 mdyne/Å) but the ratio  $k_{rr}/k_r$  systematically increases as one goes from  $MgF_2$  to  $MgI_2$  ( $k_{rr}/k_r = 0.05, 0.07, 0.09, 0.12$  for F, Cl, Br, I respectively). This may be related to a larger contribution of covalent bonding in this same progression.

#### Absolute Entropy Calculations

The statistical absolute entropies of the magnesium dihalides have been calculated using expressions given by Herzberg (36), bond

lengths from reference (61) and the vibrational frequencies from Table 10; the results are listed in Table 11. The values for  $\text{MgF}_2$  and  $\text{MgCl}_2$  are compared with the thermodynamic entropies determined from the experimental entropy of sublimation (63, 64) and the well established entropy of the solid (65). Although the experimental entropy of sublimation has been reported for  $\text{MgBr}_2$  and  $\text{MgI}_2$  (63) the corresponding entropy of the solid is not well known. Our calculations indicate that the results of Berkowitz and Marquart (63) are too low while the entropies determined by Hildenbrand et al. (64) are too high but in general the agreement is satisfactory with both of the experimental results.

Table 11. Absolute Entropies (e. u.) for the Magnesium Dihalides.

Molecule	T°K	$S_{\text{trans+rot}}^0$	$S_{\text{vib}}^0$	$S_{\text{tot}}^0$	$S^0$ (exptl.) <sup>a</sup>	$S^0$ (exptl.) <sup>b</sup>
$\text{MgF}_2$	1450	64.36	15.17	79.53	77.2	88.3
$\text{MgCl}_2$	900	64.32	16.99	81.31	77.0	84.1
$\text{MgBr}_2$	900	68.18	18.84	87.02		
$\text{MgI}_2$	900	70.69	21.13	91.82		

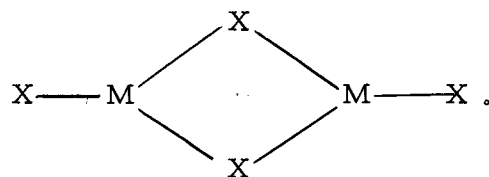
<sup>a</sup>Reference 63.

<sup>b</sup>Reference 64.

### Analysis of the Dimer Spectra

As previously discussed a number of observed features, particularly in the infrared, have been attributed to dimer or polymeric

species. It is interesting to consider the assignment of some of the more obvious dimer features although it must be noted that there is a particular lack of observed Raman frequencies since this study was mainly concerned with the monomer species. A number of workers have investigated  $M_2X_4$  systems, proposing a bridge bond structure of  $D_{2h}$  symmetry



For example, Thompson and Carlson (66) have assigned observed infrared frequencies for  $Fe_2Cl_4$ ,  $CO_2Cl_4$  and  $Ni_2Cl_4$  and have compared their observations with a simplified normal coordinate analysis patterned after that used by Buchler (67) and McNamee (68) in their study of the Zn-family dichlorides. Frey et al. (69) have extensively studied the Fe chlorides and have compared their observations for  $Fe_2Cl_4$  with a normal coordinate analysis (based in part on their studies of  $Fe_2Cl_6$ ).

For  $D_{2h}$  symmetry a  $M_2X_4$  molecule has six infrared ( $2B_{1u}$ ,  $2B_{2u}$ ,  $2B_{3u}$ ) and six Raman ( $3A_g$ ,  $2B_{1g}$ ,  $B_{2g}$ ) active fundamentals which can be described as indicated in Table 12. Intuitive arguments suggest that for the dimer the terminal bond stretch would be highest in frequency followed by the bridge-bond stretches. The terminal bond bending and ring puckering modes would lie at lower frequencies.

Table 12. Calculated<sup>a</sup> and Observed Frequencies for  $M_2X_4$  Species (Argon Matrix).

Assignment	Symmetry	this work				b	c	c	d
		$Mg_2F_4$	$Mg_2Cl_4$	$Mg_2Br_4$	$Mg_2I_4$	$Fe_2Cl_4$	$Fe_2Cl_4$	$Co_2Cl_4$	$Zn_2Cl_4$
<u>Infrared</u>	(normal mode)								
$\nu_7$ (ring pucker)	$B_{1u}$	240	140	108	92	(134)			
$\nu_8$ (ring pucker)	$B_{1u}$					(34)			
$\nu_9$ (ring str.)	$B_{2u}$	487 (498)	372 (337)	312 (266)	274 (165)	325 (325)	(298)	323 (298)	334 (310)
$\nu_{10}$ (ter. M-X bend)	$B_{2u}$	(146)	(42)	(18)	(---	(84)	110 (140)	(143)	(165)
$\nu_{11}$ (ter. M-X str.)	$B_{3u}$	747 (752)	514 (530)	425 (434)	387 (367)	438 (438)	436 (442)	433 (430)	435 (465)
$\nu_{12}$ (ring str.)	$B_{3u}$	450 (415)	260 (243)	210 (146)	(106)	249 (249)	(257)	289 (261)	297 (279)
$\nu_3$ (asym. str. monomer)	$\Sigma_u^+$	842	600	498	445	494	494	492	511
<u>Raman</u>									
$\nu_1$ (ter. M-X str.)	$A_g$	585	286	180	110	(429)			
$\nu_2$ (ring str.)	$A_g$					(250)			
$\nu_3$ (ring bend)	$A_g$					(103)			
$\nu_4$ (ring str.)	$B_{1g}$	353		155		(306)			
$\nu_5$ (ter. M-X bend)	$B_{1g}$					(130)			
$\nu_6$ (ter. M-X bend)	$B_{2g}$					(87)			

a Values in parentheses are calculated.

b reference 68.

c reference 65.

d reference 67.

To test these arguments we have calculated the  $B_{2u}$  and  $B_{3u}$  frequencies using expressions given by McNamee (68),

for  $B_{3u}$ :

$$\lambda^2 - (\mu_{Mg} + \mu_{Cl}) (F_d + F_r) \lambda + F_d \cdot F_r (\mu_{Cl} + 2\mu_{Mg}) \mu_{Cl} = 0$$

for  $B_{2u}$ :

$$\lambda^2 - \lambda \left[ F_d (\mu_{Mg} + \mu_{Cl}) + 2 \frac{F_\alpha}{\ell^2} \mu_{Cl} \right] + 2 \frac{F_\alpha}{\ell^2} \cdot F_d \left[ (\mu_{Mg} + \mu_{Cl}) \mu_{Cl} - \mu_{Mg}^2 / 4 \right] = 0$$

in which it is assumed that the bridge bonds form a square and that the potential energy can be represented by  $F_r$  for the terminal bonds,  $F_d$  for the bridge bonds and  $F_\alpha / \ell^2$  for the terminal bond bending. It is also assumed that  $F_2 = F_{33}$  (determined from the monomer) and that  $F_\alpha / \ell^2$  is the same for the monomer and the dimer. Furthermore, we assume  $F_d = F_2 / 2$  which is justified from studies on compounds such as  $B_2H_6$  (70) and  $Al_2Cl_6$  (71). The calculated frequencies are compared with the experimental values in Table 12 and the agreement is reasonable in view of the approximate nature of the calculations. Also offered for comparison: 1) Thompson and Carlson's (66) calculated and observed results for  $Fe_2Cl_4$ ,  $CO_2Cl_4$ , 2) McNamee's (68) calculated and observed results for  $Zn_2Cl_4$ , 3) Frey *et al.* (60) calculated and observed results for  $Fe_2Cl_4$  and 4)  $\nu_1$  (monomer). These calculations (69) suggest that the lowest frequency dimer mode that we assign ( $Mg_2F_4 = 240$ ,  $Mg_2Br_4 = 140$ ,  $Mg_2I_4 = 108$ ) is a ring

puckering mode rather than the terminal bond bending which lies below the monomer bending frequency. Failure to observe  $\nu_8$  and  $\nu_{10}$  is possibly due to overlap of the argon lattice modes and relatively low intensities that one might expect for these modes.

In the Raman spectrum one might expect the symmetric terminal bond stretching frequency to be near the  $\nu_1$  mode of the monomer. If this is the case we can assign this  $\nu_1$  mode of the dimer as follows:  $\text{Mg}_2\text{F}_4 = 585 \text{ cm}^{-1}$ ,  $\text{Mg}_2\text{Cl}_2 = 286 \text{ cm}^{-1}$ ,  $\text{Mg}_2\text{Br}_2 = 180 \text{ cm}^{-1}$ . The calculations of Frey et al. (69) indicate that the next highest mode would be the  $\nu_4$  ( $B_{1g}$ ) ring stretching mode which we can assign as follows:  $\text{Mg}_2\text{F}_4 = 353 \text{ cm}^{-1}$ ,  $\text{Mg}_2\text{Br}_4 = 155 \text{ cm}^{-1}$ . The lack of further vibrational data for the dimer does not allow further specific assignments for the remaining normal modes.

### Summary

The complete vibrational spectrum for all of the magnesium dihalides has been reported and observation of principally the position of  $\nu_1$  in the Raman and the corresponding region in the infrared has allowed us to conclude that all of the molecules in this series are linear (in agreement with the majority of the previous experimental and theoretical results and establishing that the assignment of a bent configuration for  $\text{MgF}_2$  on the basis of a previous infrared study was incorrect). A number of spectral complications were observed, most

interesting of these was a weak feature in the infrared (for  $\text{MgF}_2$  and  $\text{MgCl}_2$ ) that was apparently the analog of  $\nu_1$ . The infrared activity in this mode was discussed in terms of possible weak complex formation. Accurate potential constants have been determined and used as a basis for evaluating several theoretical models for the bonding in the alkali earth dihalides and in  $\text{MgF}_2$  in particular. Models based on ionic descriptions were the most successful in reproducing the observed bending force constants.

A calculation of the statistical absolute entropy was compared to the experimental values (for  $\text{MgF}_2$  and  $\text{MgCl}_2$ ) of two other investigations. The calculated values were found generally to be in good agreement with the experimental results although no clear preference for either set of data was established. Finally, an analysis of some of the observed dimer features gave reasonable agreement with calculations based on a number of simplifying assumptions.

IV. ABSORPTION SPECTRUM, LASER EXCITED FLUORESCENCE  
SPECTRUM AND PRELIMINARY LIFETIME MEASUREMENTS  
FOR MATRIX ISOLATED YF

Introduction

In Chapter I, in the Raman matrix isolation study of  $\text{PrF}_3$ , some of the experiments showed a strong fluorescence spectrum characteristic of a diatomic molecule. Although  $\text{PrF}$  would be a logical source for this spectrum, further matrix isolation studies with  $\text{LaF}_3$  gave identical results, leading us to suspect a reaction involving the tantalum Knudsen cell:  $\text{MF}_3 + \text{Ta} \longrightarrow \text{MF}_2 + \text{TaF}$  (where  $M = \text{Pr}$  or  $\text{La}$ ). Since  $\text{YF}_3$  should be easier to reduce than the  $\text{PrF}_3$  or  $\text{LaF}_3$  we next conducted a series of experiments with  $\text{YF}_3 + \text{Ta}$  and observed (in the infrared) principally  $\text{YF}_2$  and, on laser excitation, the same fluorescence spectrum but with a much greater intensity. To ease any doubt that the fluorescing species was thus  $\text{TaF}$ ,  $\text{YF}_3$  was heated in a graphite cell and, much to our surprise, the same spectrum was again obtained, though at lower intensity. Further experiments with  $\text{Y} + \text{YF}_3$  in graphite also gave the characteristic spectrum with much greater intensity. From this sequence of observations, we were finally led to conclude that the species responsible for the fluorescence spectrum is  $\text{YF}$ . This identification has been confirmed by producing  $\text{YF}$  (and the characteristic spectrum) from the reduction of  $\text{CaF}_2$  by pure yttrium metal at  $1200^\circ\text{C}$ .

The matrix spectrum of YF is interesting for a number of reasons. First, yttrium is a common impurity in most of the rare earth metals (spectrochemical analysis of our sample of  $\text{PrF}_3$  showed 0.035%  $\text{YF}_3$ ) and since YF is a very strong fluorescer, its spectrum may appear in other studies of the rare earth fluorides. Second, the gas phase spectrum of YF has recently been studied in great detail (72-74) and the molecular parameters ( $T_e$ ,  $\omega_e$ ,  $\omega_e x_e$ ,  $B_e$ ,  $r_e$ ) are known for several electronic states. Comparison of the gas and matrix values can give an indication of the effect of the matrix on the potential functions of these states. In addition, comparison of the observed relative intensities with those calculated from Franck-Condon factors provides a test of the  $r_e$  value deduced for the matrix. Furthermore, we observed that the spectrum is very sensitive to the matrix environment, as is the rate of vibrational relaxation in the upper electronic state. A simple model in terms of several different substitutional sites is offered which provides a very consistent explanation of all the observations. Finally, YF was thought to be an excellent candidate for vibrational lifetime measurements (in the ground state) using novel techniques developed by Dr. Louis J. Allamandola and Professor J. W. Nibler at this University (75). As discussed, below, several electronic states are capable of being excited by the argon ion laser and the Rhodamine 6G dye laser, making possible these types of lifetime studies. However, some complications,

thought at this time to involve intersystem crossing with a triplet electronic state, have hindered the preliminary vibrational lifetime measurements and raised interesting questions concerning the excited electronic states of this system.

### Experimental

The experimental apparatus used in this study has been described in Chapter I and conventional techniques for the matrix isolation of high temperature species have been used. Only the details particular to these experiments will be described here.

The matrix gas was typically deposited at rates of 2-3 cc/min and the sample was heated in graphite or Ta Knudsen cells. YF was generated in several ways: a) from a 0.035%  $\text{YF}_3$  impurity in  $\text{PrF}_3$  (99.9% Michigan Chemical Corp.) heated to 1300-1350°C for deposit times on the order of 3 hrs, b) from  $\text{YF}_3$  (99.9% Ventron Alfa Inorganic) heated to 1300-1350°C for 1 hr, c) from a mixture of  $\text{CaF}_2$  (Baker analyzed c. p. grade) and yttrium metal (99+% Atlantic Equipment Engineers, NJ) heated to 1100-1200°C for deposit times of about one-half hour, d) from  $\text{Y} + \text{YF}_3$  heated to 1100-1200°C for 15-30 min. In all cases the sample was outgassed for about 15 min at 25-50°C higher than the deposit temperature before the cold tip was cooled and the Knudsen cell temperature was measured by an optical pyrometer. For the UV-visible absorption experiments the sample

was deposited on a sapphire window cooled to 12-14<sup>o</sup>K and the spectra were recorded using a Cary 15 spectrophotometer (wavelength calibrated as indicated in Appendix II). The emission spectra were obtained using a Cary 82 spectrophotometer (corrected for relative instrument response as indicated in Appendix III). Relative intensity measurements were made using peak height and area and both types of measurements were comparable to within 10%. The relative intensities were corrected for instrument response and problems associated with background corrections, etc., limit the precision of the results to  $\pm 10\%$ .

## Results

### Absorption and Laser Excited Emission Spectra and Molecular Constants of YF

Typical absorption spectra for YF isolated in an argon matrix are shown in Fig. 20 and the values of  $T_{oo}$  and  $G_{1/2}$  are compared with the gas absorptions (72) at 2000<sup>o</sup>C in Table 13. The labeling of the states follows the conventions introduced in the gas phase work and of particular interest (due to their proximity to the laser frequencies) are the  $B^1\Pi$  and  $C^1\Sigma^+$  states labeled in Fig. 20. There appears to be two distinct matrix sites for the molecule; site A, represented by trace A, is obtained almost exclusively by deposition

Figure 20. Absorption spectra for YF generated from  $Y + YF_3$  (Ta Knudsen cell), Absorbance setting = 1.0 full scale.

A: 0.5 hr,  $T = 1200^\circ C$ .

B: 1.0 hr,  $T = 1300^\circ C$ .

C: Same as B after annealing at  $35-40^\circ K$  followed by recooling to  $14^\circ K$ .

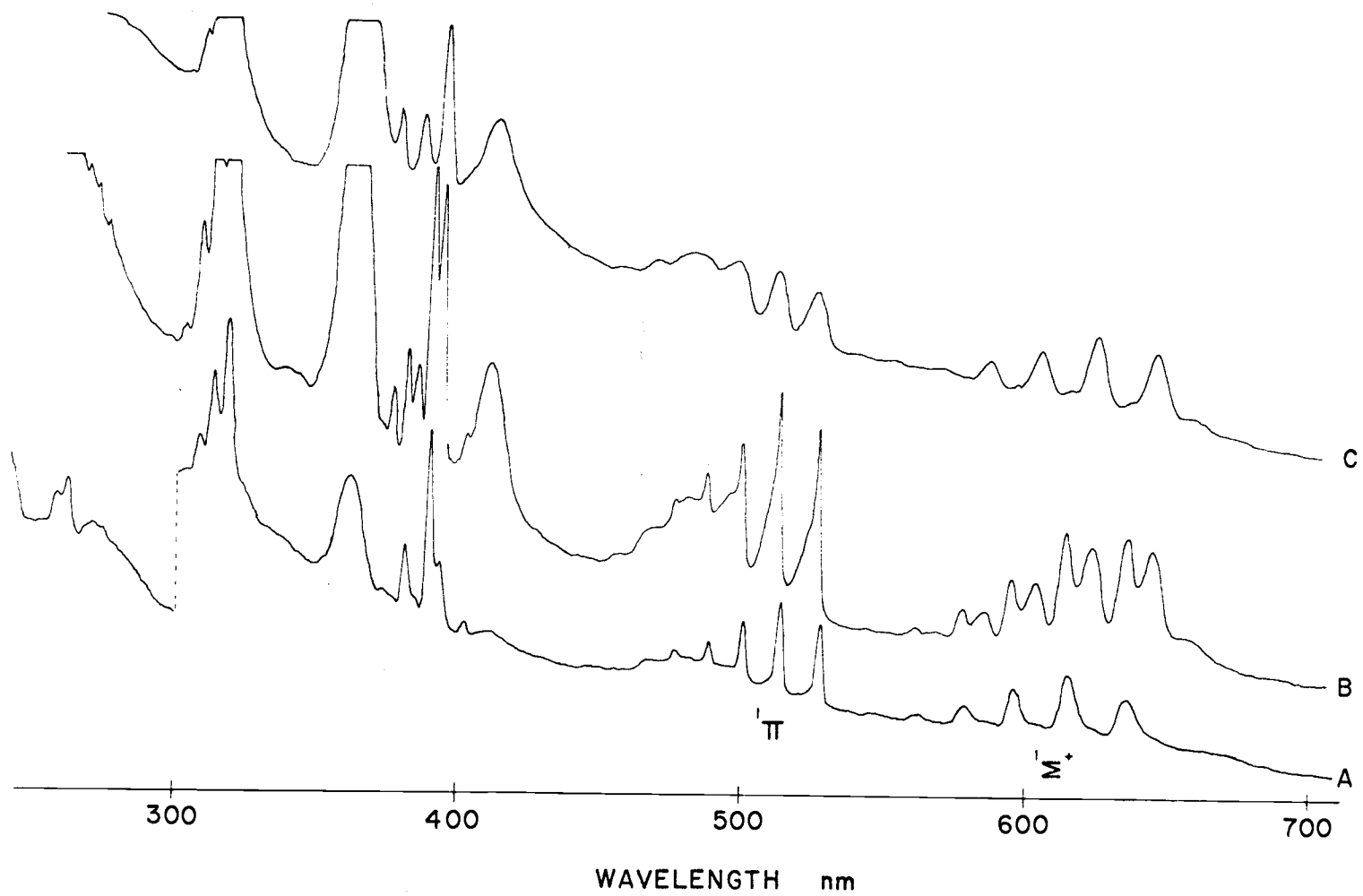


Table 13. Comparison of YF Absorptions in an Argon Matrix at 14°K with Gas Absorptions at 2000°C.<sup>a</sup>

State	Gas			Matrix - Site A			Matrix - Site B		
	T <sub>00</sub>	$\Delta G_{1/2}$	v'	$\lambda$ (nm)	$\nu$ (cm <sup>-1</sup> -vac.)	$\Delta\nu$ (cm <sup>-1</sup> )	$\lambda$ (nm)	$\nu$ (cm <sup>-1</sup> -vac.)	$\Delta\nu$ (cm <sup>-1</sup> )
X <sup>1</sup> E*	0	631.3	---	---	---	---	---	---	---
B <sup>1</sup> $\Pi$	15885.8	534.7	0?	636.7 <sup>b</sup>	15701		644.1	15521	
			1?	615.6	16239	538	623.0	16046	525
			2?	596.6	16757	518	603.9	16554	508
			3?	579.2	17260	503	585.8	17066	512
			4?	562	17739	(529) <sup>c</sup>	570	17539	(473)
C <sup>1</sup> E*	19190.3	527.2	0	528.4	18919		525.0	19042	
			1	514.3	19438	519	511.2	19556	514
			2	501.4	19958	500	498	20074	(518)
			3	489.2	20456	498	482	20741	(667)?
			4	477.8	20923	487	468	21348	(607)?
I <sub>1</sub>	25324.9	---	---	390.1	25627		385.4	25940	
I <sub>2</sub>	25464.5	---	---	381.8	26185		376.9	26525	
I <sub>3</sub>	26046.4	---	---	372.8	26795				
I <sub>4</sub> *	27987	547.5	---	366	27315		362	27617	
I <sub>5</sub>	31205	536.3		317.2	31516				
				312.0	32042	526			
				307.5	32511	469			
				302.5	33049	538			
?				278.3	35921				
				274.8	36379	458			
				271.0	36889	510			
				267.5	37372	483			
				264.3	37825	435			

a reference 71.

b All frequencies recorded in absorption are believed to be accurate to  $\pm 10$  cm<sup>-1</sup>.

c Values in parentheses are uncertain.

temperatures near  $1200^{\circ}\text{C}$  while trace B shows that a second series "grows in" as the deposition temperature is raised to  $1300^{\circ}\text{C}$ . A reasonable interpretation, in terms of localized heating of the matrix produced by this higher temperature, appears to be that this annealing favors a second site (B). Support for this is shown in trace C which is the same as trace B except that the matrix has been annealed to  $35-40^{\circ}\text{K}$  and then recooled to  $14^{\circ}\text{K}$ . This process is seen to favor the site B bands and implications of these two sites in terms of a simple model will be discussed below. Also observed in the short wavelength region of these spectra, are a number of broad featureless absorptions which can be tentatively attributed to  $\text{YF}_2$ .

The argon ion laser excited emission spectra of YF using four different excitation frequencies are shown in Fig. 21 and Table 14 gives the observed transitions in the form of a Deslandres table. The excitation is to the  $\text{C}^1\Sigma^+$  state and these emission spectra correspond to absorption spectra of type A bands exclusively. Although the absorptions are relatively narrow, the match between exciting frequency and absorption frequency apparently does not have to be exact (note that the  $4765 \text{ \AA}$  exciting line is  $70 \text{ cm}^{-1}$  higher than the  $0''$ ,  $4'$  transition).

Since the emission lines for this state were very sharp ( $1/2$  width  $\approx 20 \text{ cm}^{-1}$ ) the measured frequencies are believed to be accurate to  $\pm 1 \text{ cm}^{-1}$ . Table 15 lists some of the observed and

Figure 21. Emission spectra ( $C^1\Sigma^+ - X^1\Sigma^+$ ) of YF in argon at  $14^\circ\text{K}$  generated from  $Y + YF_3$  (graphite Knudsen cell) for a 20 min deposit at  $T = 1100^\circ\text{C}$ .

A: 5145 Å (1w),  $1.5 \times 10^5$  cps,  $\text{SBW} = 2 \text{ cm}^{-1}$ .

B: 5017 Å (.3w),  $1.0 \times 10^5$  cps,  $\text{SBW} = 3 \text{ cm}^{-1}$ .

C: 4880 Å (1w),  $1.0 \times 10^5$  cps,  $\text{SBW} = 4 \text{ cm}^{-1}$ .

D: 4765 Å (.6w),  $5.0 \times 10^4$  cps,  $\text{SBW} = 4 \text{ cm}^{-1}$ .

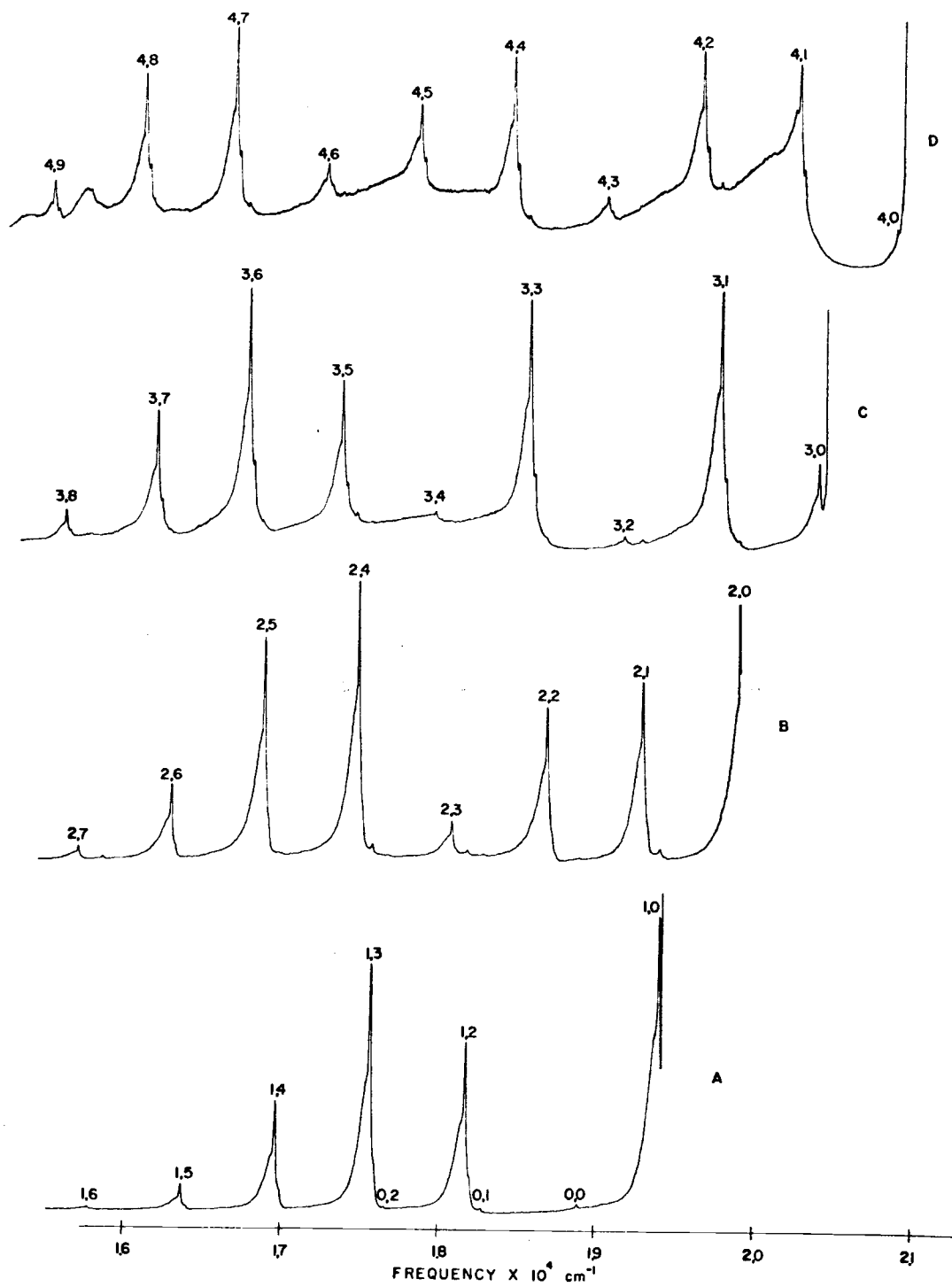


Table 14. Deslandres table for YF in argon ( $C^1\Sigma^+ \rightarrow X^1\Sigma^+$  system)

$v''$	0	1	2	3	4	5	6	7	8	9									
0	18884 516	619	18265	616	17649 514	610	17039 514	---	---	---									
1	19400 509	---	---	18165 509	610	17555 507	607	16946 511	599	16347 510	590	15757 505	---	---	---				
2	19909 502	622	19287 505	615	18672 505	612	18060 506	603	17457 504	600	16857 503	595	16262 504	592	15670 506	---	---		
3	20411 500	619	19792 498	615	19177 497	611	18566 498	605	17961 496	601	17360 498	594	16766 497	590	16176 497	587	15589 499	---	
4	20911	621	20290	616	19674	610	19064	607	18457	599	17858	595	17265	590	16673	585	16088	579	15509

Table 15. Molecular Parameters for Gaseous<sup>a</sup> and matrix isolated YF.

State	$T_e$ cm <sup>-1</sup>	$\omega_e$ cm <sup>-1</sup>	$\omega_e^x$ cm <sup>-1</sup>	$r_e$ Å	$B_e$ cm <sup>-1</sup>	$\alpha_e \times 10^{-3}$	$k_2 \times 10^5$ dynes/cm	$k_3 \times 10^{13}$ dynes/cm <sup>2</sup>	$k_4 \times 10^{21}$ dynes/cm <sup>3</sup>
<u>C<sup>1</sup>Σ<sup>+</sup></u>									
Ar matrix	18937	520	2.76	2.022	.26343	(1.74)	2.483	-3.88	3.89
Gas	19242.4	532.1	2.50	2.010	.26657	1.74	2.610	-4.12	4.16
<u>B<sup>1</sup>Π</u>									
Ar matrix									
Site A	15737	554 ± 3	9 ± 1						
Site B	15570	528 ± 13	4 ± 3						
Gas	15934.3	539.4	2.35						
<u>X<sup>1</sup>Σ<sup>+</sup></u>									
(gr. state)									
Ar matrix	0	626	2.54	1.934	.28792	(1.63)	3.601	-5.67	5.60
Gas	0	636.3	2.50	1.926	.29042	1.63	3.732	-5.91	5.92

<sup>a</sup>Ref. 71

<sup>b</sup>The values for  $\omega_e$  in the matrix were obtained by a Birge-Spooner plot and the errors (not indicated if <1cm<sup>-1</sup>) were obtained from a least squares analysis of these plots.

calculated molecular parameters for the matrix and compares them with the gas phase results. The  $0''$ ,  $0'$  frequency derived from the absorption and emission spectra is not identical, a discrepancy which we believe is introduced by the breadth of the absorption bands. This implies that for the  $C^1\Sigma^+$  state the molecular constants are more accurately determined from the emission data. The  $T_e$  value is shifted about  $300\text{ cm}^{-1}$  to the red in going to the matrix, a shift comparable to those observed for other diatomic molecules (76). The decrease in the values of  $\omega_e'$  and  $\omega_e''$  ( $11, 13\text{ cm}^{-1}$ ) is also typical and indicates that the quadratic potential terms are smaller in the matrix. An estimate of  $r_e'$  and  $r_e''$  in the matrix was obtained from the relation  $\omega_e r_e^n = C$ , where the constants  $n = 4.17$  and  $C = 9784$  were deduced from the known gas phase values for the two electronic states of interest. These values of  $r_e$  yield the  $B_e$  values listed in Table 15.

The anharmonic vibrational potential function for YF is written as  $2V = k_2x^2 + k_3x^3 + k_4x^4$  and the constants can be obtained from  $\omega_e$ ,  $\omega_e x_e$  and from  $\alpha_e$  (the correction term for the variation of  $B_e$  with vibrational state). For a Morse potential curve (77),

$$\alpha_e = [6 (\omega_e x_e B_e^3)^{1/2} - 6 B_e^2] / \omega_e$$

and substitution of values of  $\omega_e x_e$ ,  $\omega_e$ , and  $B_e$  gives essentially identical results for the gas and matrix. For this reason, we have

used the experimental gas phase values of  $\alpha_e$  for both the gas and the matrix in deducing the force constants in the usual manner (77, 78). From these constants it is clear that the potential curve does not rise as rapidly in the matrix for either electronic state. Thus, at least up to about the seventh vibrational level or so, the dominant interaction of YF with the matrix must be attractive in nature. That this is true at the bottom of the well is of course indicated by the  $\omega_e$  and  $r_e$  values in the matrix.

Preliminary emission spectra from the  $B^1\Pi$  state (excited by the tunable dye laser with frequencies available from 15950-17550  $\text{cm}^{-1}$ ) are shown together with a tentative energy level diagram in Fig. 22. The progressions are neither sharp nor simple as was the case with the  $C^1\Sigma^+$  state and additional complications occur since in these spectra the molecules were isolated in a mixture of type A and B sites. The labeling of the bands as indicated requires that the  $0''-0'$  absorption lie one vibrational spacing to the red of the value listed in Table 13. Therefore the assignments of the absorption and emission frequencies for this  $B^1\Pi$  state are not to be considered definite and further experiments, preferably ones in which only type A or B sites were present, are needed to confirm these preliminary results. One other complication that will be discussed below is the possibility of triplet-triplet emission which might be observed in this region if the molecule is excited by appropriate dye laser frequencies.

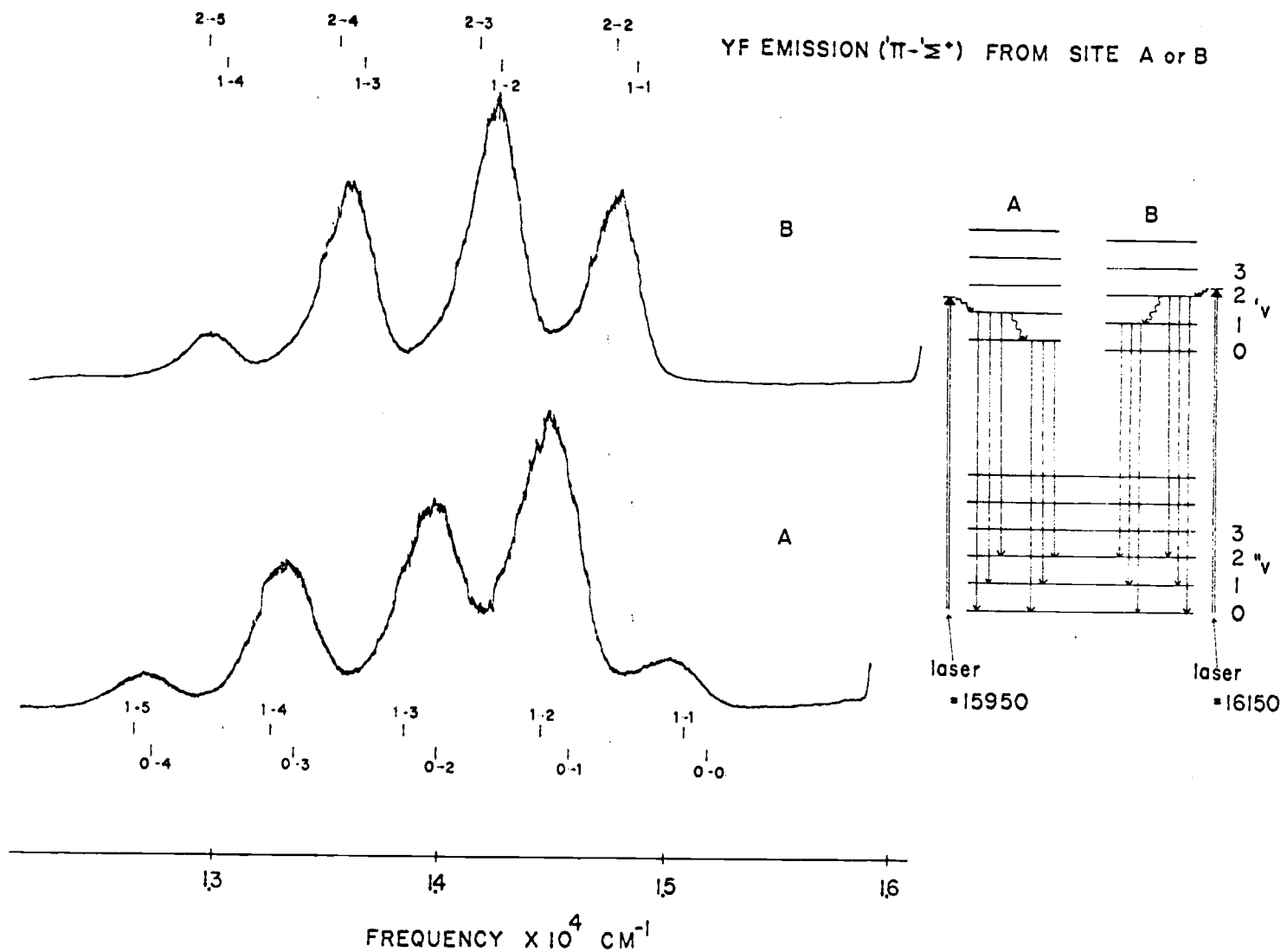


Fig. 22. Preliminary emission results for YF in argon ( $B^1\Pi \rightarrow X^1\Sigma^+$ ) with tentative energy level diagram.

Since the emission spectra of the  $B^1\Pi$  state are not well characterized, the values of  $\omega_e$  and  $\omega_e x_e$  for sites A and B were obtained from the absorption data. A comparison between these values (with their rather large error limits due to uncertainties in the band center) and the gas phase results is offered in Table 15.

Several experiments were conducted to observe the vibrational frequency of YF in the ground state directly by infrared absorption. However, the concentration of YF must have been very small since, although a large amount of  $YF_2$  was observed (by monitoring its  $\nu_3$  mode near  $550\text{ cm}^{-1}$  (79) ), no trace of an absorption attributable to YF was found.

### Franck-Condon Factors

Examination of Figure 21 shows marked intensity alternations within the several vibrational progressions and it is interesting to compare these relative intensities with those calculated using both the gas and the matrix molecular parameters. These theoretical intensities are proportional to  $\nu^4$  times the appropriate Franck-Condon factors. Table 16 offers this contrast, where the Franck-Condon factors were calculated using a modified version (80) of a program written by Zare (81). The calculated intensity trends fit the observations very satisfactorily, e.g., the "missing" (1, 1) transition has a very small calculated intensity. Comparison of the theoretical

Table 16. Comparison of Observed and Calculated Relative Emission Intensities for YF ( $C^1\Sigma^+ \rightarrow X^1\Sigma^+$ ).

Transition	Obs. Pk. Ht.	Calc. <sup>a</sup> Matrix	Calc. <sup>a</sup> Gas
0,0	10.0 <sup>b</sup>	10.0	10.0
1	8.4	9.6	9.1
2	3.5	4.3	3.8
3	0.5	1.2	1.0
4	0.0	0.2	0.2
5	0.0	0.0	0.0
6	0.0	0.0	0.0
7	0.0	0.0	0.0
8	0.0	0.0	0.0
9	0.0	0.0	0.0
1,0	10.0	10.0	10.0
1	0.0	0.0	0.0
2	3.8	4.4	5.1
3	4.5	5.6	5.6
4	2.0	2.7	2.4
5	0.4	0.7	0.6
6	0.0	0.1	0.1
7	0.0	0.0	0.0
8	0.0	0.0	0.0
9	0.0	0.0	0.0
2,0	10.0	10.0	10.0
1	6.8	7.1	8.4
2	4.3	4.5	4.0
3	0.9	1.1	1.9
4	6.2	7.7	8.8
5	5.1	6.5	6.6
6	1.5	1.7	2.5
7	0.5	0.6	0.5
8	0.0	0.1	0.1
9	0.0	0.0	0.0
3,0	4.0	3.6	3.3
1	10.0	10.0	10.0
2	0.2	0.5	0.8
3	5.1	6.1	6.0
4	0.1	0.1	0.0
5	2.0	3.5	4.4
6	3.6	5.9	6.0
7	1.9	3.3	3.0
8	0.5	1.0	0.8
9	0.0	0.2	0.1
4,0	1.8	1.7	1.6
1	10.0	10.0	10.0
2	6.2	8.5	9.8
3	0.7	0.8	0.4
4	4.5	6.3	7.5
5	1.9	2.6	1.9
6	0.8	1.4	2.4
7	5.0	7.0	8.1
8	3.2	5.8	5.8
9	1.2	2.3	2.0

a Calculated using matrix and gas phase parameters listed in Table 16.

b Observed intensities were corrected for instrument response and normalized relative to the strongest transition.

values shows that the fit is better for the matrix molecular parameters than for the gas values but the large uncertainties in both the calculated and experimental intensities make it doubtful that further inferences are warranted.

## Discussion

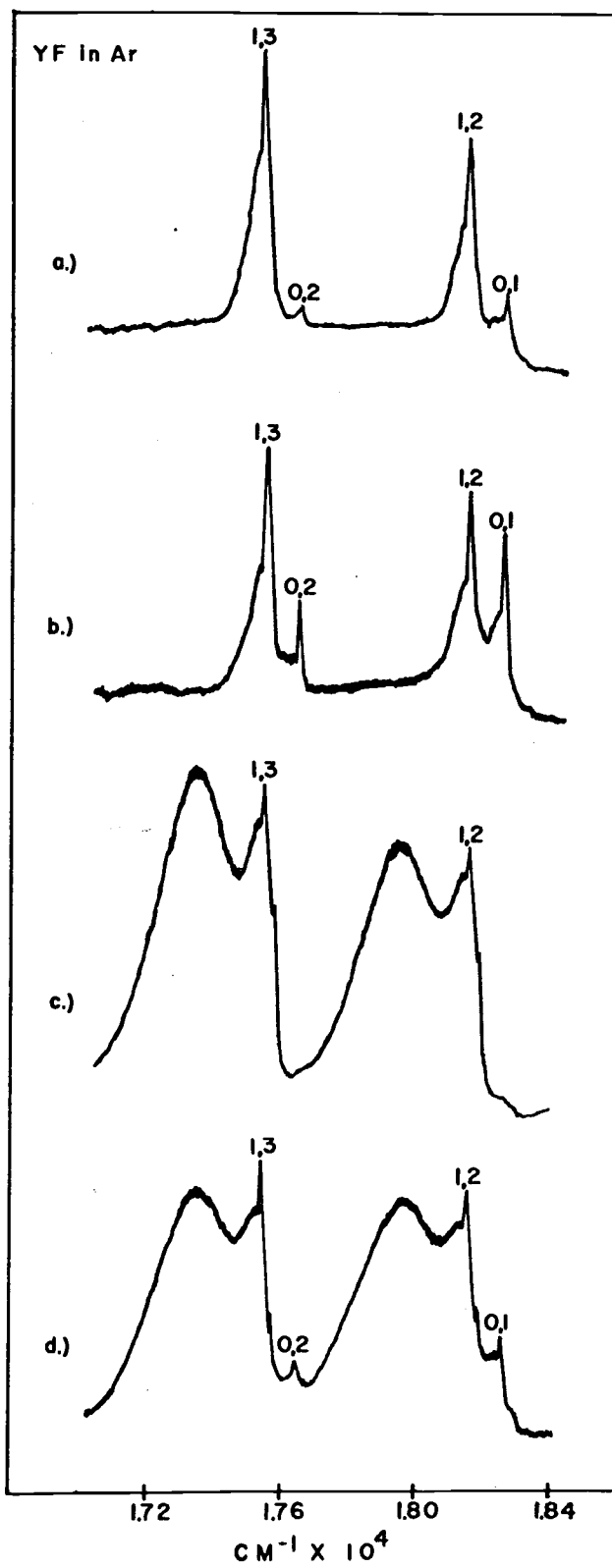
### Matrix Effects

Phonon Interactions. It is significant that while the sharp fluorescence bands for the  $C^1\Sigma^+$  state (shown in Fig. 21) have a definite shoulder to the red, the absorption spectra (Fig. 20B) show similar shoulders shifted to the blue. A similar shading has been noted (82) for  $C_2^-$  in emission and absorption, and a number of comparable examples exist (76). It is clear from these observations that this structure is due to a phonon sideband resulting from interaction between the guest molecule and the host lattice modes. That this structure occurs on only one side of the transition is reasonable since the phonon relaxation time will be comparable to the period of the lattice vibrational frequency,  $\approx 10^{-12}$  sec. Thus for the emission process, thermal depopulation of the excited lattice vibrational levels occurs long before fluorescence ( $\approx 10^{-8}$  sec). The blue phonon sideband in absorption is actually rather fortunate since it markedly increases the probability of absorption of the narrow laser line and

this suggests that such studies may be practical for a large number of colored systems. For YF, the  $19926 \text{ cm}^{-1}$  ( $5017 \text{ \AA}$ ) laser line was most nearly resonant with the (2, 0) electronic transition ( $E = +17 \text{ cm}^{-1}$ ) and hence very good spectra were obtained (Fig. 21B) despite the relatively low power of this line. Such near resonance is probably not essential for strong absorbers or cases where the coupling with the lattice modes is particularly strong. (E.g., for  $\text{C}_2^-$  in Xe, emission is seen even though  $\Delta E = +456 \text{ cm}^{-1}$ , a result believed to be due to a strong coupling interaction because of the charge.)

Site Effects. In a number of experiments, a system of broad bands were observed to the red of the sharp lines (Fig. 23C, D). The frequencies of the broad bands did not depend noticeably on the mode of preparation and their relative intensities correlate well with the pattern observed for the sharp features. Thus it seems likely that the broad bands correspond to YF isolated in a different site (type B), a site which we believe by the following reasoning to correspond to a direct substitution for a single argon atom. The force constant calculations indicate an attractive interaction between Ar and YF and thus, for a given cavity radius, the greater the YF bondlength the more the potential energy is lowered. This implies a larger decrease for the upper electronic state ( $r'_e = 2.010 \text{ \AA}$ )--and a red shift in the transition as observed (Fig. 24). Until the repulsive interactions become significant, one would expect a continuous shift to the red as

- Figure 23. Fluorescence spectra of YF in Ar at 14°K.  
19430 cm<sup>-1</sup> (5145 Å) excitation, SBW = 3 cm<sup>-1</sup>.
- A: From YF<sub>3</sub> in Ta at 1350°C, Ar flow = 2 cc/min,  
10<sup>4</sup> counts/sec, 3 hours deposit.
- B: From PrF<sub>3</sub> in Ta at 1325°C, Ar flow = 2 cc/min,  
2 x 10<sup>3</sup> counts/sec, 3.5 hour deposit.
- C: From CaF<sub>2</sub> + Y in graphite at 1100°C, Ar flow =  
12 cc/min, 2 x 10<sup>5</sup> counts/sec, 0.5 hour deposit.
- D: From PrF<sub>3</sub> in Ta at 1320°C, Ar flow = 2 cc/min,  
2.5 x 10<sup>4</sup> counts/sec, 1.5 hour deposit.





the cavity radius is shrunk from the "largest site" (gas) to a medium site (A--sharp bands) to the smallest possible site (B--broad bands). Consideration of the covalent radii of Y and F shows that YF can fit (rather snugly) into a single Ar substitutional hole but not into an interstitial site. The breadth of the site B bands can be understood in terms of a significant modulation of the electronic levels as the cavity radius is changed during the lattice vibration. For site A, this modulation is less important because of the larger cavity and thus the bands are sharper. It should be noticed that there is an indication of yet a third site since a sharp shoulder appears slightly to the blue of the type A bands; this would presumably correspond to a larger site in which three Ar atoms are removed.

Several other observations support this simple picture. First we have noted a definite variation in the relative intensities of the type A and B bands as one samples different regions on the cold tip, the type B bands being favored in the thicker center of the deposit. Since most of the room temperature Ar initially impinges here, it is likely that there is local annealing which produces the energetically favored site B. On the fringes of the tip, the matrix gas has already lost much of its kinetic energy due to deflecting collisions and hence the formation of the less stable sites is more likely. We do not believe that the broad features are due to YF aggregates since the amount of YF is very small in all cases, as evidenced by the fact that

it was not detected at all in infrared experiments even though extremely intense absorptions of  $\text{PrF}_3$  or  $\text{YF}_2$  were observed. Several dilution and warmup experiments were done and, although the observations are not clearcut because of spectral variations across the sample, the results do suggest that the broad bands are favored by conditions leading to local annealing (e.g., high deposition rates or temperatures). Also, as previously mentioned in the absorption experiments, the type B bands were favored by controlled annealing. Finally, experiments were also run in krypton and nitrogen. In krypton, no sharp features were observed, only broad bands which were slightly closer to the gas phase transitions than were the type B bands in argon. These results suggest that in Kr type A sites do not form because YF fits easily into a single substitutional site. In nitrogen, no spectrum was observed at all, a result which suggests that YF may form a molecular complex with  $\text{N}_2$  in a manner similar to that previously observed for  $\text{NiF}_2$  in  $\text{N}_2$  (82).

Vibrational Relaxation. In a previous study of  $\text{C}_2^-$ , it was concluded that the rate of vibrational relaxation was exceedingly slow in Ar ( $\approx 1 \text{ msec}^{-1}$ ). Thus it is particularly interesting that emission is observed from two or three vibrational levels of the upper electronic state of YF since this suggests that the vibrational relaxation and the fluorescence lifetimes are comparable for YF. This could be due to vibrational relaxation by emission of an infrared photon (forbidden for

$C_2^-$ ) but the following argues against this. Figures 23A, B, and C indicate that the extent of the vibrational relaxation is noticeably dependent on the mode of preparation. In particular, the loss of the  $514\text{ cm}^{-1}$  of vibrational energy was much easier in matrices containing  $\text{PrF}_3$  (Fig. 23B) than in those containing  $\text{YF}_2$  (Fig. 23A) or  $\text{CaF}$  and  $\text{Ca}$  (Fig. 23C). We believe that this indicates a more efficient resonant exchange of energy for  $\text{YF}$  with  $\text{PrF}_3$  ( $\nu_1 = 526\text{ cm}^{-1}$ ) than with  $\text{YF}_2$  ( $\nu_1 = 542\text{ cm}^{-1}$ ) (79) or  $\text{CaF}$  ( $582\text{ cm}^{-1}$ ) (77). Certainly, all of these species are present in excess and some undoubtedly lie near  $\text{YF}$  in the matrix. The molecules need not necessarily occupy a site adjacent to  $\text{YF}$  since the frequency of, for example, the (1,2) transition does not differ noticeably in Fig. 23B and C and thus the perturbation is not large. Moreover, infrared scans show no evidence of dimers of  $\text{PrF}_3$  or  $\text{YF}_2$ . Finally, however, an indication that the relaxation process may be concentration dependent is provided by the variations observed in the two  $\text{PrF}_3$  experiments shown in Fig. 23B and D. Since the scan of Fig. 23D was taken at the deposit fringes, it is presumably more dilute and hence less relaxation is observed, a result confirmed by other dilution experiments on  $\text{YF}_3 + \text{Ta}$ . However a more quantitative elucidation of the effect of distance on the vibrational relaxation process would require a more controllable test system of two nearly resonant partners whose concentrations are each independently variable. An effort to study such a system is underway.

Preliminary Vibrational Lifetime Studies

As noted, the vibrational lifetimes for YF are slower than the fluorescence lifetimes, a fact which is supported by Fig. 25. The weaker band to the blue of the  $19430 \text{ cm}^{-1}$  exciting line is due to emission from a molecule which is excited from a higher vibrational level in the ground state (as indicated in the Figure). We had proposed to measure the vibrational lifetimes using techniques previously described (75) and outlined in the energy level diagram of Fig. 26. The method involves populating the ground state vibrational levels by emission from the excited  $C^1\Sigma^+$  state pumped by the argon ion laser ( $\nu_p$ ). Once a vibrational level has been populated (the  $2''$  for example) its decay can be monitored by excitation by a frequency ( $\nu_{pr}$ ) that will cause emission ( $1' \rightarrow 0''$  for example). The intensity of this emission can be measured as a function of the time delay between the  $\nu_p$  and  $\nu_{pr}$  radiation and suitably analyzed (as was the case with  $C_2^-$  (75) ) to yield the vibrational lifetime of a particular vibrational level.

The results of the experiment to measure the lifetime of the  $2''$  level of YF using this technique are also shown in Fig. 26. Trace a was obtained with  $\nu_p = 19926 \text{ cm}^{-1}$  and it shows that the  $2''$ ,  $1''$  and  $0''$  levels are populated via this emission process. There is also a hint of  $1' \rightarrow 0''$  emission caused by a small amount of relaxation in the upper state followed by emission. When  $\nu_{pr}$  was focused to the

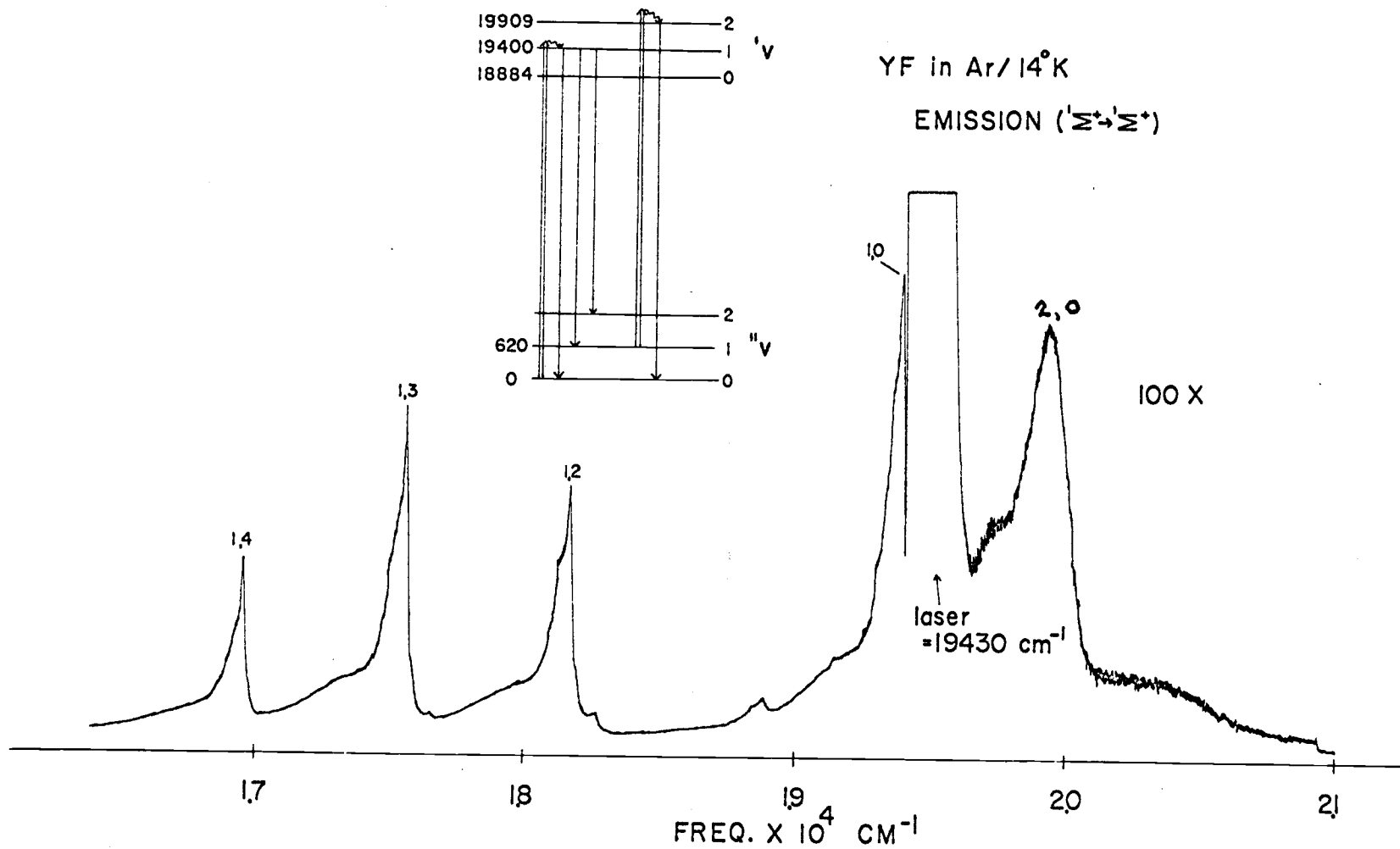


Fig. 25. YF emission ( $C^1\Sigma^+ \rightarrow X^1\Sigma^+$ ) showing excitation of a higher vibrational level. Anti-stokes side of the laser line recorded at 100X.

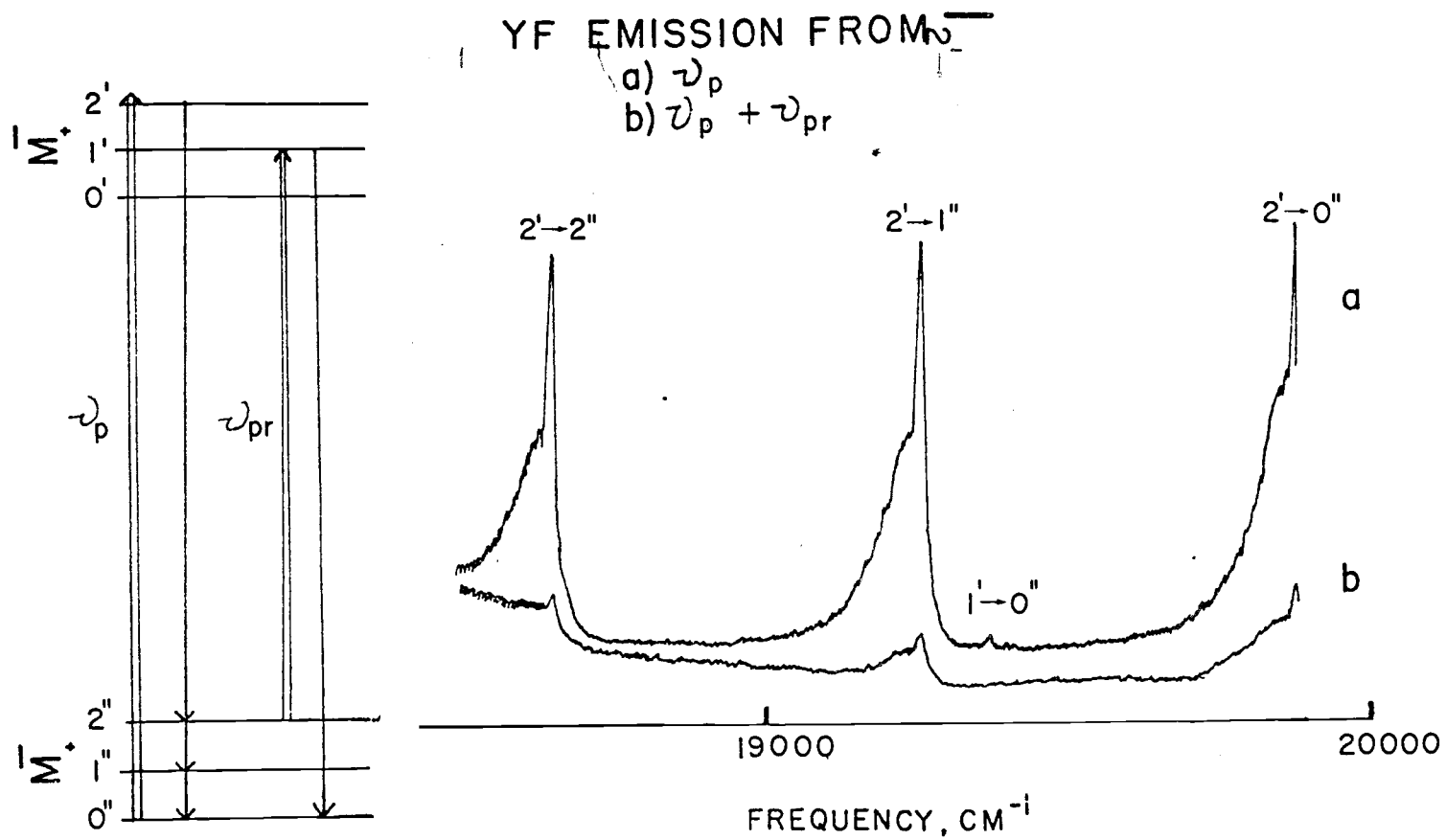


Fig. 26 Observed change in the YF ( $\text{C}^1\Sigma^+ \rightarrow \text{X}^1\Sigma^+$ ) emission during vibrational lifetime experiments; a:  $\nu_p$ , b:  $\nu_p + \nu_{pr}$ .

same spot in the matrix so that both frequencies were inducing excitation (trace b) the  $1' \rightarrow 0''$  transition should have been enhanced.

Instead the spectrum as a whole experienced a dramatic decrease in intensity; a quite surprising result which suggested that the  $\nu_{pr}$  was essentially removing molecules from the ground state. When the decrease in intensity of the  $2' \rightarrow 1''$  was monitored as a function of the  $\nu_{pr}$  frequency, the dotted trace was obtained in Fig. 27. For comparison the absorption spectrum of the  $B^1\Pi$  state is reproduced on the same scale (solid line) where it is shown that a minimum in the  $2' \rightarrow 1''$  intensity corresponds to a maximum in the absorption spectrum. This indicated that the molecules were being excited to the  $B^1\Pi$  state by  $\nu_{pr}$  and most effectively when  $\nu_{pr}$  corresponded to a maximum in the absorption of the  $B^1\Pi$  state.

More surprisingly it was found that when  $\nu_{pr}$  was turned off ( $\nu_p$  still on) the molecules did not immediately return to the ground state as would be expected by simple emission from the  $B^1\Pi$ . This is shown in Fig. 28 where the intensity of the  $2' \rightarrow 1''$  is plotted versus time. At time = 0, when  $\nu_{pr}$  (probe) is off, the  $\nu_p$  pumped  $2' \rightarrow 1''$  emission proceeds as before. When the probe is on the intensity drops as molecules are removed from the ground state to the  $B^1\Pi$  state. When the probe is turned off (time  $\simeq 10$  min) it is seen that the  $2' \rightarrow 1''$  signal returns very slowly. This suggests a mechanism which might involve intersystem crossing into a triplet state(s) which

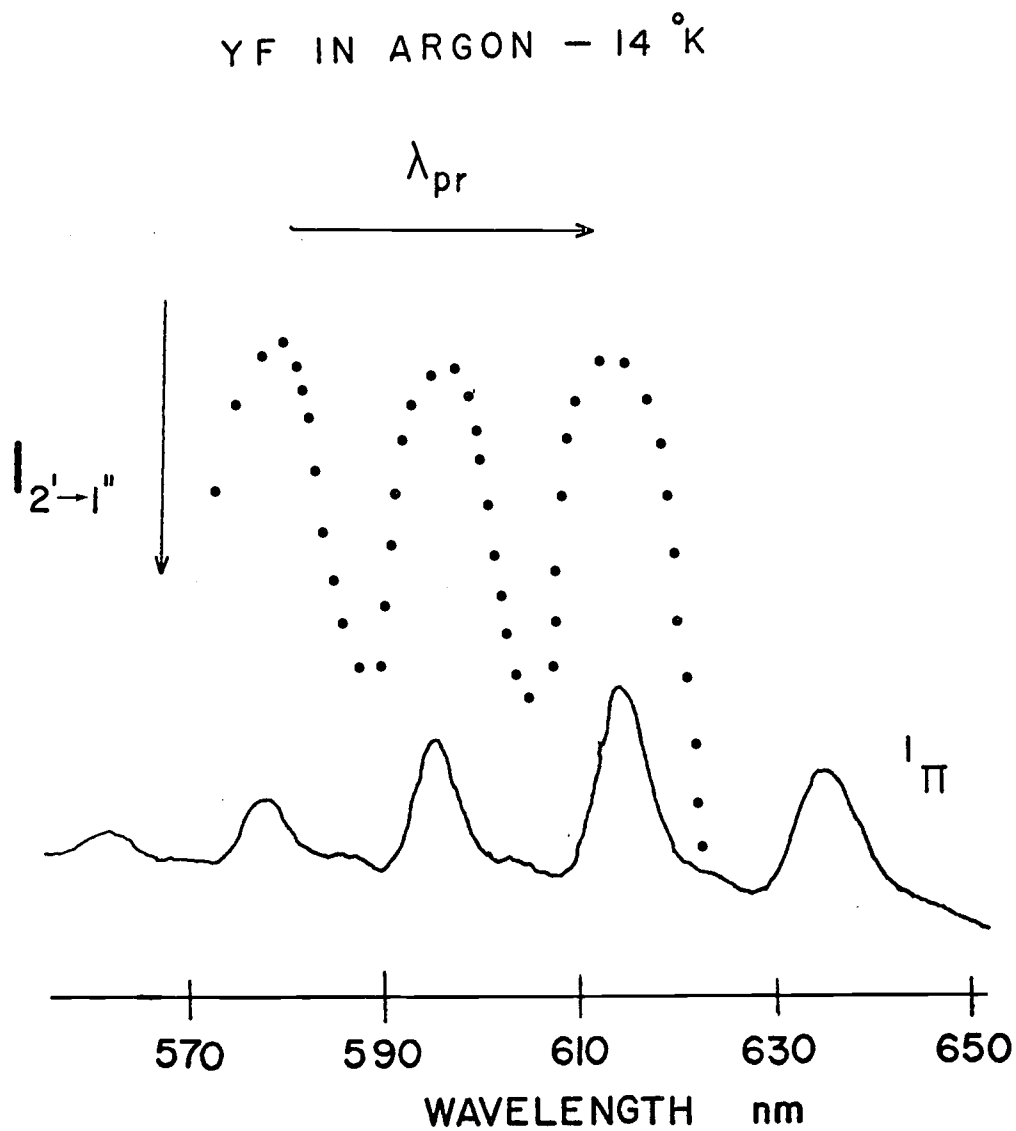


Fig. 27 ..... Variation of the intensity(I) of the  $2' \rightarrow 1''$  emission vs. wavelength. —  $B^1\Pi$  absorption spectrum.

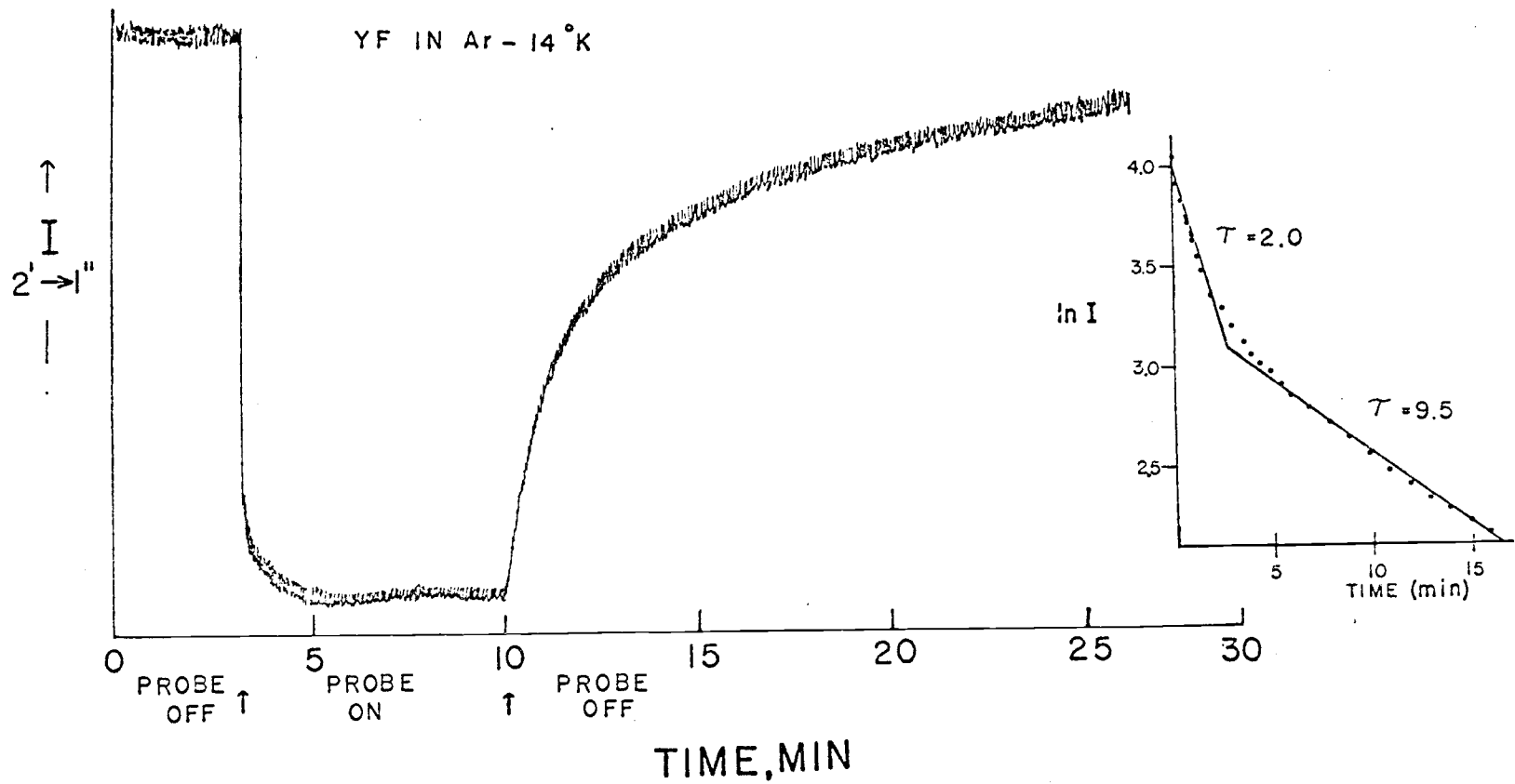


Fig.28 Observed change in intensity ( $I$ ) of the  $2' \rightarrow 1''$  emission with time as  $\nu_{pr}$  (probe) is turned on and off.

is shown schematically in Fig. 29. The gas phase values for the triplet states are shown below (taken from reference (72) ):

State	$T_{00}$	$\Delta G_{1/2}$
${}^3\phi_4$	$15,028.0 + x_3$	
${}^3\phi_3$	$14,842.8 + x_2$	531.3
${}^3\phi_2$	$14,635.5 + x_1$	
${}^3\Delta_3$	$x_3$	578.5
${}^3\Delta_2$	$x_2$	577.5
${}^3\Delta_1$	$x_1$	576.4

The exact singlet ground state-triplet ground state splitting is not known; however, it may be argued that it is relatively small as was observed in a matrix study (84) of the isoelectronic molecule ZrO.

A possible mechanism (Fig. 29) might be that  $\nu_{pr}$  excites molecules to the  $B^1\Pi$  state, which then intersystem cross to a  ${}^3\phi$  state, followed by emission to the low lying  ${}^3\Delta$  state. The molecules return to the ground singlet state via intersystem crossing, a process which we believe at this time to be responsible for the long delay in the return of the  $2' \rightarrow 1''$  signal after the probe is turned off (at time  $\simeq 10$  min.). A graphical analysis of this decay is also shown in Fig. 28 where a plot of  $\ln$  of the  $2' \rightarrow 1''$  intensity (arbitrary units) is presented. If the curve is approximated by two straight lines as shown,

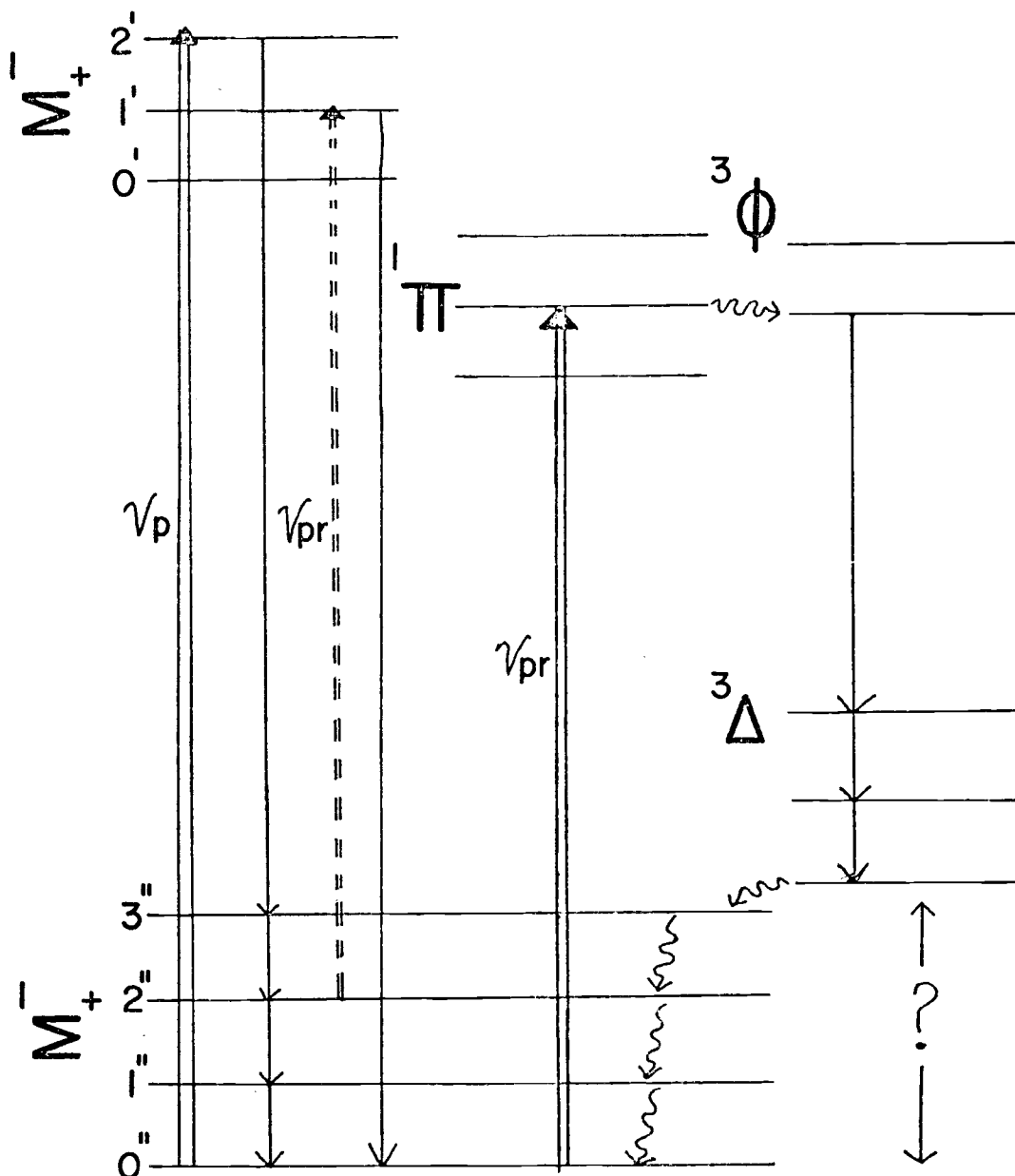


Fig.29 Possible mechanism for the results observed during the vibrational lifetime measurements for YF in argon.

a first order analysis gives lifetimes ( $\tau$ ) of 2.0 and 9.5 min respectively. The interpretation of these two separate lifetimes, which can tentatively be considered as some measure of some singlet-triplet intersystem crossing lifetimes, is not readily apparent and experiments are underway to elucidate the mechanism by which these long lifetimes are produced. Further experiments will be conducted to assure that these effects are not due merely to heating of the matrix by  $\nu_{pr}$  and to hopefully limit the magnitude of the singlet-triplet ground state splitting.

### Summary

YF has been identified as a decomposition product of  $YF_3$  and has been produced in a number of novel ways. Its absorption spectrum has been obtained and a number of singlet states have been observed and compared with known gas phase data. The absorption spectrum also indicates that there are two distinct sites in the argon matrix and a simple model (in terms of the size of the vacancy in the matrix) has been proposed to account for some of the spectral features due to these site effects. Emission (induced by an argon ion laser) from the  $C^1\Sigma^+$  state has been well characterized and extensively analyzed to yield molecular constants which indicate a net attraction between the argon matrix and the YF molecule. Some preliminary emission results (induced by a dye laser) from the  $B^1\Pi$  were reported but were

not extensive and could not give an indication of the molecular constants for this state.

From the accurately known molecular parameters in the gas and the matrix, Franck-Condon factors were obtained and were used to calculate intensities for the purpose of comparison with the observed values. The fit of the observed intensities to those calculated from gas and matrix parameters was good, however, unfortunately the comparison of the observed and calculated values did not serve as a useful test of the  $r_e$  value deduced for the matrix.

A number of interesting matrix effects were noted: the shading of the absorption and emission bands was attributed to phonon sidebands and the varying degree of vibrational relaxation observed in the emission spectra was related to the ability of YF to exchange vibrational energy with other guests in the matrix.

Finally, several preliminary lifetime experiments were described and the results indicated that the molecules appeared to be undergoing singlet-triplet excited state inter-system crossing and a possible mechanism was proposed which indicated that the lifetime associated with the molecules returning from the triplet state to the singlet ground state was on the order of minutes. Further experimental work to confirm these results and to elucidate the mechanism that produces these long lifetimes is in progress.

## BIBLIOGRAPHY

1. J.S. Shirk and H.H. Claassen, *J. Chem. Phys.*, 54, 3237 (1971).
2. D. Boal, G. Briggs, H. Huber, G.A. Ozin, E.A. Robinson and A. Van der Voet, *Nature Phys. Sci.*, 231, 174 (1971).
3. L. Andrews, to appear in "Vibrational Spectra and Structure," vol. III, ed. J.R. Durig, Marcel Dekker Inc., New York, 1974.
4. V.E. Bondybey and J.W. Nibler, *J. Chem. Phys.*, 58, 2125 (1973).
5. L.Y. Nelson and G.C. Pimentel, *Inorg. Chem.*, 6, 1758 (1967).
6. R.D. Wesley and C.W. DeKock, *J. Chem. Phys.*, 55, 3866 (1971).
7. R.H. Hauge, J.W. Hastie and J.L. Margrave, *J. Less-Common Metals*, 23, 359 (1971).
8. J.W. Hastie, R.H. Hauge and J.L. Margrave, *J. Less-Common Metals*, 39, 309 (1975).
9. L.V. Vilkov, N.G. Rambidi and V.P. Spiridonov, *Zh. Strukt. Khim.*, 8, 786 (1967).
10. E.W. Kaiser, W.E. Falconer and W. Klemperer, *J. Chem. Phys.*, 56, 5392 (1972).
11. We would like to acknowledge Dr. H. Claassen as originally indicating the advantages of this type of reflection arrangement.
12. a) J.W. Nibler and D. Coe, "Raman Matrix Isolation Spectroscopy," presented at the 26th Symposium on Molecular Structure and Spectroscopy, June 1971.  
b) J.W. Nibler and D. Coe, *J. Chem. Phys.* 55, 5134 (1971).
13. J.R. Clifton, D.M. Gruen and A. Ron, *J. Mol. Spec.*, 39, 202 (1971).
14. J.H. Van Vleck, *J. Chem. Phys.*, 7, 61 (1939).

15. A. Hadni, G. Morlot and P. Strimer, *IEEE J. Quant. Elec.*, QE3, 111 (1967).
16. F.J. Keneshea and D. Cubicciotti, *J. Phys. Chem.*, 69, 3910 (1965).
17. F.J. Keneshea and D. Cubicciotti, *J. Phys. Chem.*, 71, 1958 (1967).
18. J.M. Brom, Jr. and H.F. Franzen, *J. Chem. Phys.*, 54, 2874 (1971).
19. J.L. Dehmer, J. Berkowitz and L.C. Cusachs, *J. Chem. Phys.*, 58, 5681 (1973).
20. M.G. Fickes, R.C. Slater, W.G. Becker and R.C. Stern, *Chem. Phys. Lett.*, 24, 105 (1974).
21. J.S. Muentner, *Chem. Phys. Lett.*, 26, 97 (1974).
22. Private communication by Prof. Victor Spiridonov of Moscow State University, U.S.S.R.
23. J.W. Nibler, "Advances in Raman Spectroscopy," vol. 1, chap. 8, 1972, ed. J.P. Mathieu, Hayden & Son Ltd. (1973).
24. V.G. Solomonik, E.Z. Zasorin, G.V. Giricev and K.S. Krasnov, *Izv. Vyssh. Uchebn. Zaved., Khim. Khim. Tekhnol.*, 17, 136 (1974).
25. A.R. Miller, *J. Chem. Phys.* 42, 3734 (1965).
26. M. Moskovits and G.A. Ozin, *Applied Spectroscopy* 26, 481 (1972).
27. Type EX crystal--available from 3 to 60 MHz from International Crystal Mfg. Co., 10 North Lee, Oklahoma City, OK 73102 (\$3.95). A suitable oscillator circuit and power supply with case is available from the same manufacturer for \$20.50 (case FOT-10 with oscillator OT-3).
28. A.W. Warner, "Ultra Micro Weight Determinations," Chap. 7, ed. S.P. Wolsky and E.J. Zdanuk, John Wiley and Son (1969).
29. G.O. Jones and J.M. Woodfine, *Proc. Phys. Soc.*, 86, 101 (1965).

30. A. J. Barnes, J. B. Davies, H. E. Hallam and G. F. Schrimshaw, G. C. Hayward and R. C. Milward, Chem. Comm., 1089 (1969).
31. H. M. Gager, J. Lewis and M. J. Ware, Chem. Comm., 616 (1966).
32. J. R. Durig, K. K. Lau, G. Nagara, M. Walker and J. Bragin, J. Chem. Phys., 50, 2130 (1969).
33. J. Berkowitz, J. Chem. Phys., 29, 1386 (1958); 32, 1519 (1960).
34. A. H. Barrett and M. Mandel, Phys. Rev., 109, 1572 (1958).
35. D. White, K. S. Seshadri, D. F. Dever, D. E. Mann and M. J. Linevsky, J. Chem. Phys., 39, 2463 (1963).
36. G. Herzberg, "Molecular Spectra and Molecular Structure. II. Infrared and Raman Spectra," Van Nostrand, New York (1954).
37. D. Cubicciotti, J. Phys. Chem., 68, 1528 (1964).
38. O. N. Komshilova and O. G. Polyachenok, Zh. Fiz. Khim., 43, 2676 (1969).
39. S. J. Cyvin, J. Brunvoll, B. N. Cyvin, I. Elvebredd and G. Hagen, Mol. Phys. 14, 43 (1968).
40. D. S. Ginter, M. L. Ginter and K. K. Innes, J. Phys. Chem., 69, 2480 (1965).
41. P. A. Akishin and V. P. Spiridorov, Krystallografiya, 2, 475 (1957).
42. A. Buchler, J. L. Stauffer and W. Klemperer, J. Amer. Chem. Soc., 86, 4544 (1964).
43. L. Wharton, R. A. Berg and W. Klemperer, J. Chem. Phys., 39, 2023 (1963).
44. D. E. Mann, G. V. Calder, K. S. Seshadri, D. White and M. J. Linevsky, J. Chem. Phys., 46, 1138 (1967).
45. V. Calder, D. E. Mann, K. S. Seshadri, M. Allavena and D. White, J. Chem. Phys., 51, 2093 (1969).

46. A. Snelson, *J. Phys. Chem.*, 70, 3208 (1966).
47. R.H. Hauge, J.L. Margrave and A.S. Kana'an, *J. Chem. Soc., Faraday Transactions II*, 71, 1082 (1975).
48. E.F. Hayes, *J. Phys. Chem.*, 70, 3740 (1966).
49. A. Allavena and S. Besnainou, *J. Mol. Struct.*, 11, 439 (1972).
50. M. Astier, G. Berthier and P. Millie, *J. Chem. Phys.*, 57, 5008 (1972).
51. J. L. Gole, A.K.Q. Siu and E.F. Hayes, *J. Chem. Phys.*, 58, 857 (1973).
52. E.F. Hayes, A.K.Q. Siu and D.W. Kisker, *J. Chem. Phys.*, 59, 4587 (1973).
53. Y.S. Kim and R.G. Gordon, *J. Chem. Phys.*, 60, 4332 (1974).
54. A. Buchler and W. Klemperer, *J. Chem. Phys.*, 29, 121 (1958).
55. D.L. Cocke, C.A. Chang and K.A. Gingerich, *Appl. Spect.*, 27, 260 (1973).
56. D. White, G.V. Calder, S. Hemple and D.E. Mann, *J. Chem. Phys.*, 59, 6645 (1973).
57. S.P. Randall, F.T. Greene and J.L. Margrave, *J. Phys. Chem.*, 63, 758 (1959).
58. J. Berkowitz and J.R. Marquart, *J. Chem. Phys.*, 37, 1853 (1962).
59. W.F. Howard, Jr. and L. Andrews, *J. Raman Spec.*, 2, 447 (1974).
60. I am grateful to Professor Hauge of Rice University for private communication of preliminary results.
61. K.S. Krasnov, V.S. Timoshinin, T.G. Danilova and S.V. Khandozhko, "Handbook of Molecular Constants of Inorganic Compounds," Keter Press, Jerusalem (1970).

62. A. Buchler, W. Klemperer and A.G. Emslie, *J. Chem. Phys.*, 36, 2499 (1962).
63. J. Berkowitz and J.R. Marquart, *J. Chem. Phys.*, 37, 1853 (1962).
64. D.L. Hildenbrand, W.F. Hall, F. Ju and N.D. Potter. *J. Chem. Phys.*, 40, 2882 (1964).
65. Natl. Bur. Std. Report No. 6928 (July 1960).
66. K.R. Thompson and K.D. Carlson, *J. Chem. Phys.*, 49, 4379 (1968).
67. A. Buchler, Ph.D. dissertation, Harvard University, 1960.
68. R.W. McNamee Jr., Ph.D. dissertation, University of California at Berkeley, 1962; also issued as Univ. Calif. Rad. Lab. Report UCRL-10451.
69. R.A. Frey, R.D. Werder and Hs. H. Gunthard, *J. Mol. Spec.*, 35, 260 (1970).
70. R.B. Bell and H.C. Longuet-Higgins, *Proc. Roy. Soc., Ser. A*, 183, 357 (1955).
71. T. Onishi and T. Shimanoudri, *Spectrochim. Acta*, 20, 325 (1964).
72. R.F. Barrow, M.W. Bastin, D.L.G. Moore and C.J. Prott, *Nature*, 215, 1072 (1967).
73. E.A. Shenyavskaya, A.A. Mal'tsev and L.V. Gurvich, *Opt. Spektr.*, 21, 680 (1966).
74. D.E. Mann, N. Aquista and M.J. Linevsky, *A.E.C. Nuclear Science Abstracts*, 18, 26163 (1964).
75. L.J. Allamandola and J.W. Nibler, *Chem. Phys. Lett.*, 28, 335 (1974).
76. B. Meyer, "Low Temperature Spectroscopy," Elsevier, 1971.
77. G. Herzberg, "Spectra of Diatomic Molecules," D. Van Nostrand, 1950.

78. D.R. Herschbach and V.W. Laurie, UCRL Publication 9694, 1961.
79. R.D. Wesley and C.W. DeKock, J. Phys. Chem., 77, 466 (1973).
80. H.S. Liszt and Wm. H. Smith, JQSRT., 11, 1043 (1971).
81. R.N. Zare, UCRL Publication 10925, 1963.
82. V.E. Bondybey and J.W. Nibler, J. Chem. Phys., 56, 4719 (1972).
83. C.W. DeKock and D.A. Van Leirsburg, J. Amer. Chem. Soc., 94, 3235 (1972).
84. W. Weltner Jr. and D. McLeod Jr., J. Phys. Chem., 69, 3488 (1965).
85. G. Strey, Spectromchim. Acta, 25A, 163 (1969).

## APPENDICES

## I. Calibration and Use of the Crystal Oscillator

Three crystals were calibrated and they can be identified by the diameter of the electrodes (see Table I.1). The calibration curves shown in Fig. I.1 were obtained by depositing salt on the entire crystal, measuring the frequency change and washing off the salt followed by dilution for atomic absorption analysis. The slopes of these experimental curves must be corrected by several factors (see Table I.1): 1) by multiplying by the ratio of Na/NaCl (since the AA analysis is only for Na), 2) by multiplying by the ratio of the area of the electrode ( $n'$ ) to the area of the entire crystal ( $n$ ) since only the electrode area itself is sensitive to mass changes (comparable results were obtained with a mask so that only the electrode itself is deposited on), 3) dividing by the area of the electrode.

In practice it is best to use a mask with a known aperture (slightly smaller than the area of the electrode); the experimental rate (MHz/time) is then multiplied by the corrected crystal constant ( $\text{mg/MHz cm}^2$ ) and the effective electrode area ( $\text{cm}^2$ ) as determined by the size of the mask. The resulting rate has the units mg/time. Note: subsequent experiments indicated that one of the electrodes should not be grounded to the brass tube; a double feed-through on the brass tube is required.

Table I.1 Experimental and Corrected Crystal Constants (K)

<u>Crystal</u>	Electrode Diameter	Electrode Area	n'/n	Experimental Crystal K	-Corrected Crystal K
#1 5MHz	7.0 mm	.385 cm <sup>2</sup>	.291	41.5 ±1.5 μg/KHz	12.3 mg/MHz cm <sup>2</sup>
#2 5MHz	5.9 (oblong)	.273	.210	47.5 ±1.7	14.4
#3 9MHz	5.2	.212	.186	13.6 ±0.3	4.7

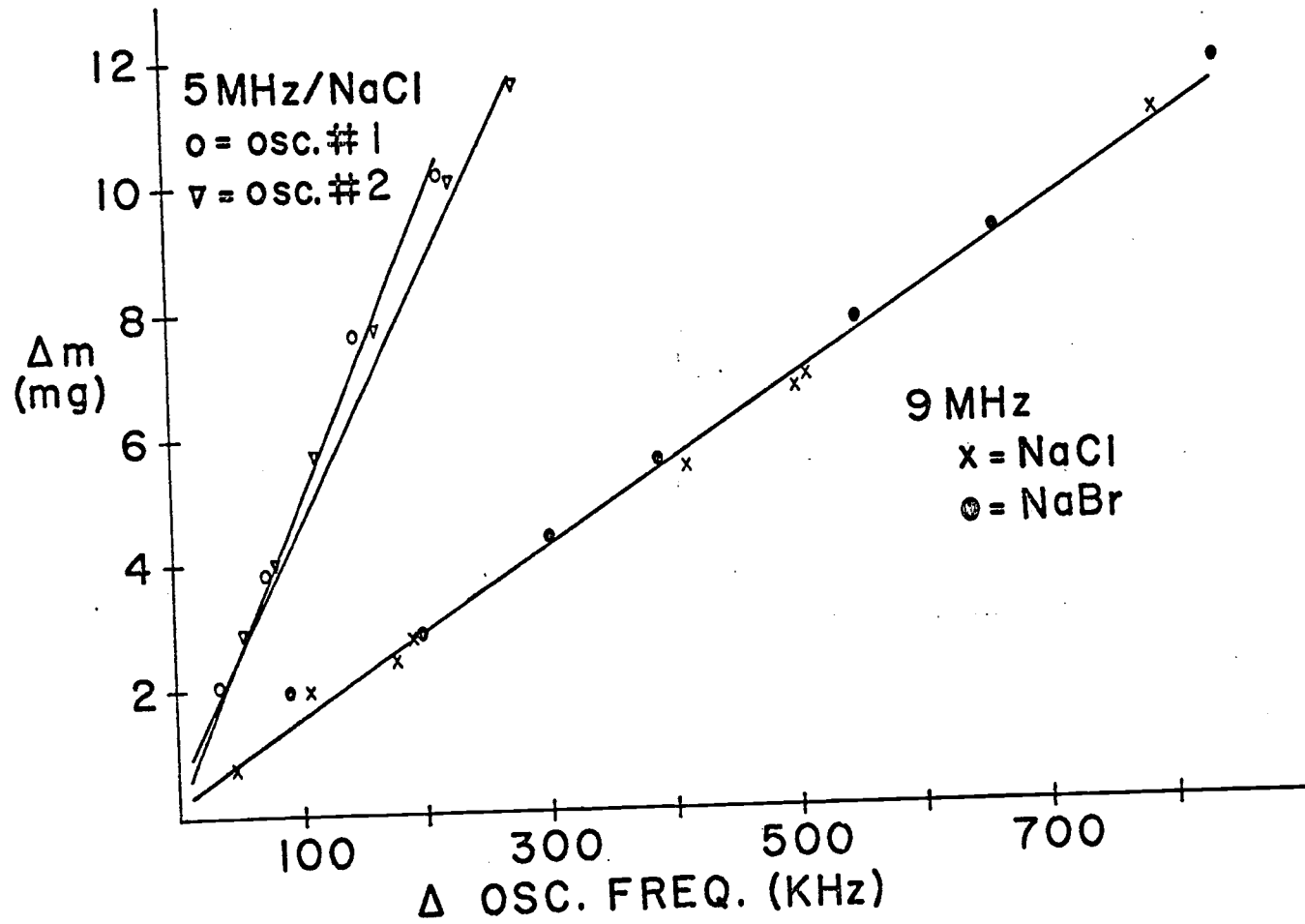


Fig. I.1 Calibration Curves for Three Crystals

## II. Cary 15 Wavelength Calibration

The Cary 15 was calibrated on 5/20/74 using a mercury lamp and a He-Ne laser (632.8 nm) as sources. The results are shown in Table II.1 with the correction factor ( $\Delta$ ) that must be added to the observed wavelength ( $\lambda_{\text{obs}}$ ) so that it is equal to the true wavelength ( $\lambda_{\text{true}}$ ).

The  $\lambda_{\text{true}}(\text{air})$  can be conveniently converted to  $\lambda_{\text{true}}(\text{vac})$  by the tables of Strey (85). Note: the magnitude of this correction is 0.4-0.6 nm in the 700-500 nm region.

Table II.1 Cary 15 Wavelength (nm) Calibration

---

---

$\lambda_{\text{true}}$	$\lambda_{\text{obs}}$	$\Delta$
253.48	253.5	0
289.36	289.2	.2
296.73	296.7	0
312.56	312.4	.2
313.16	313.1	.1
334.15	334.0	.15
365.01	364.7	.3
365.48	365.2	.3
366.31	366.1	.2
390.64	390.3	.3
404.66	404.4	.3
407.78	407.7	.1
435.83	435.5	.3
491.60	490.7	.9
546.07	545.2	.9
576.96	576.2	.8
579.07	578.4	.7
632.8	632.1	.7

---

---

### III. Determination of the Relative Response ( $\beta$ ) of the Cary 82

It is necessary to evaluate  $\beta$  since the transmission characteristics of the spectrophotometer and the efficiency of the phototube vary with the frequency and polarization of the light. This correction is essential when comparing observed relative intensities in Raman or fluorescence spectra. To measure  $\beta$  a standard tungsten lamp (Gamma Scientific, model 220-1A, ser.no. 1031) was placed in the sample area (positioned to give approx.  $10^5$  cps full scale at  $15000 \text{ cm}^{-1}$ ) and the spectrum was recorded for a given spectral bandwidth (SBW) and polarization over the frequency range of interest. This spectrum gives directly the spectrophotometer output  $N_c$  in cps. A calibration curve supplied with the lamp gives the known output in microwatts per  $\text{cm}^2$  per nm per SR from 400-725 nm. Since the Cary 82 actually measures photons per sec it is necessary to convert the output of the lamp to units of photons per sec per  $\text{cm}^2$  per  $\text{cm}^{-1}$  per SR. This is accomplished by multiplying the known output at a certain wavelength  $\lambda$  (in cm) by a factor of  $10^8 \lambda^3 / hc$ . The lamp output in these units is given in Table III.1.

To obtain  $\beta$ , the output of the standard lamp is divided by the output of the spectrophotometer  $N_c$  (Table III.2). Table III.3 gives  $\beta$  values for various SBW's and polarizations. These  $\beta$ 's can be normalized as is convenient and values normalized to  $19000 \text{ cm}^{-1}$  are given in Table III.4. In practice the intensity of each band is multiplied by the  $\beta$  value corresponding to the frequency of the band.

Table III.1 Standard Lamp Output Conversion

$\lambda$ nm	$\frac{\mu\text{w}}{\text{cm}^2 \text{ nm SR}}$	$\nu$ $\text{cm}^{-1}$	$\frac{\text{photons}}{\text{sec cm}^2 \text{ cm}^{-1} \text{ SR}}$
400	.015	25000	$.482 \times 10^9$
425	.085	23529	3.27
450	.155	22222	7.10
475	.235	21052	12.6
500	.31	20000	19.4
525	.39	19047	28.2
550	.465	18181	38.8
575	.545	17391	52.0
600	.625	16666	67.9
625	.68	16000	83.4
650	.73	15384	100.6
675	.815	14814	125.
700	.91	14285	157.
725	1.05	13793	201.

Table III.2 Experimental Values for  $N_c^i$  ( $i = \text{SBW}$ ) with  
Model #220 Standard Lamp (5/30/74).

$\nu_{\text{cm}^{-1}}$	$N_c^{2\text{cm}^{-1}}$	$N_c^{3\text{cm}^{-1}}$	$N_c^{3\text{cm}^{-1}\alpha}$	$N_c^{4\text{cm}^{-1}}$	$N_c^{5\text{cm}^{-1}}$
12000	$1.0 \times 10^4$	$1.8 \times 10^4$	$1.8 \times 10^4$	$1.9 \times 10^4$	$2.1 \times 10^4$
12500	3.3	4.5	4.1	4.4	4.5
13000	5.8	6.7	5.6	6.5	7.0
13500	8.3	8.4	6.5	8.0	8.5
14000	9.1	8.6	6.2	8.2	8.6
14500	9.4	8.3	5.5	7.6	8.0
15000	9.6	7.7	4.9	7.1	7.6
15500	9.5	6.9	4.4	6.4	6.9
16000	8.8	6.2	4.2	5.8	6.2
16500	8.2	5.5	3.4	5.1	5.6
17000	6.9	4.6	2.9	4.3	4.6
17500	5.6	3.6	2.3	3.3	3.9
18000	4.4	2.7	1.7	2.5	2.8
18500	3.3	2.1	1.2	2.0	2.2
19000	2.3	1.3	.86	1.3	1.4
19500	1.5	.84	.55	.87	.91
20000	.94	.52	.31	.53	.57
20500	.56	.34	.16	.33	.33
21000	.31	.18	.08	.18	.20
21500	.17	.093	.03	.10	.11
22000	.10	.054	.01	.06	.06

$\alpha$   $N_c^{3\text{cm}^{-1}}$  implies that the polaroid was placed between the sample and collection lens in the parallel configuration. The other runs were made without the polaroid.

Table III.3 Values of  $\beta_i^j$  ( $i = \text{SBW}$ ,  $j = \text{polarization}$ ).

$\nu_{\text{cm}^{-1}}$	$\beta_2 \text{ cm}^{-1}$	$\beta_3 \text{ cm}^{-1}$	$\beta_3^{\prime\prime} \text{ cm}^{-1}$	$\beta_{4\text{cm}^{-1}}$	$\beta_{5\text{cm}^{-1}}$
13500	$28 \times 10^5$	$27 \times 10^5$	$35 \times 10^5$	$29 \times 10^5$	$27 \times 10^5$
14000	20	22	30	23	22
14500	16	18	27	19	18
15000	12	15	24	17	16
15500	10	14	22	15	14
16000	10	13	20	14	13
16500	8.5	13	21	14	12.5
17000	8.6	13	20	14	13
17500	8.9	14	22	15	13
18000	9.5	16	25	17	15
18500	11	17	29	17.5	16
19000	12	22	33	22	20
19500	16	29	44	28	26
20000	20	37	61	36	33
20500	29	47	100	48	48
21000	42	72	162	72	65
21500	59	107	333	100	91
22000	80	148	800	133	133

Table III.4  $\beta$  Values Normalized to 19000  $\text{cm}^{-1}$ .

$\nu$	$\beta_{2\text{cm}^{-1}}$	$\beta_{3\text{cm}^{-1}}$	$\beta_{3\text{cm}^{-1}}^{\parallel}$	$\beta_{4\text{cm}^{-1}}$	$\beta_{5\text{cm}^{-1}}$
13500	2.3	1.2	1.1	1.3	1.35
14000	1.7	1.0	.91	1.0	1.0
14500	1.3	.82	.82	.86	.90
15000	1.0	.68	.73	.77	.73
15500	.83	.64	.67	.68	.70
16000	.83	.59	.61	.64	.65
16500	.71	.59	.64	.64	.63
17000	.72	.59	.61	.64	.65
17500	.74	.64	.67	.68	.65
18000	.79	.73	.76	.77	.75
18500	.92	.77	.88	.80	.80
19000	1.0	1.0	1.0	1.0	1.0
19500	1.3	1.3	1.3	1.3	1.3
20000	1.7	1.7	1.8	1.6	1.65
20500	2.4	2.1	3.0	2.2	2.4
21000	3.5	3.3	4.9	3.3	3.25
21500	4.9	4.9	10	4.5	4.55
22000	6.7	6.7	24.2	6.0	6.65